Conceptual Design Report

for a multi-turn Energy Recovery Linac-based Synchrotron Light Facility (Femto-Science Factory)

T. Atkinson, A. Bondarenko, A. Matveenko, Y. Petenev

Helmholtz-Zentrum Berlin
für Materialien und Energie
Hahn-Meitner Platz 1
D-14109 Berlin
Germany

Berlin
July, 2015

Disclaimer:

Written for an evolving project, this report naturally reflects a momentary status of the work, here of July, 2015. Additional chapters, improved solutions, new conditions and technical limitations are continuously being incorporated in the design.

Publisher

Helmholtz-Zentrum Berlin für Materialien und Energie GmbH
Hahn-Meitner Platz 1
D-14109 Berlin
Germany

E-mail: info@helmholtz-berlin.de
Homepage: www.helmholtz-berlin.de

DOI doi:10.5442/R0002
http://dx.doi.org/10.5442/R0002

1 Contents

2 Executive summary

The next generation of particle accelerators needs to meet the high demands and ever changing fields of science. With almost a century of history, and a wealth of applications ranging from high energy particle physics to medical, the accelerators have continually improved.

The production of X-ray radiation using synchrotron light sources is presently described as in its 3rd generation. The first and second define the conversion from accelerators used for particle collisions to dedicated machines for the sole purpose of producing synchrotron radiation. The 3rd generation, of which dozens of storage ring machines exist around the world from Brazil to Japan, circulate high average current electron bunches to yield hard X-rays to often more than 50 user work stations at any one time.

The next generation promises to relieve the physical restraints of the present machines, predominately, equilibrium states associated with multi-pass storage rings. A valid candidate of which is the Free Electron Laser, in which high peak brightness is reached using a single pass through a linac section before amplified photon emission is achieved in the magnetic undulator section. Since the accelerated beam is simply “wasted” at full energy once the light is produced, the present setup of such a machine is restricted to a low duty cycle.

Designs based on the recuperation of beam energy using recirculating magnetic optic and the same linac for acceleration and deceleration could encompass both high duty and the advantages of a single pass. These Energy Recovery Linac (ERL) based facilities are presently in a prototype phase, whereby a compact machine is used to rigorously test technical limitations at low beam energy. Although the technology is not particularly new the demands on the accelerator and the optic require novel developments to meet future user demands.

The trend is towards the acceleration of continuous wave (cw) high average current, short pulse electron bunches of high brilliance and low energy spread. The three dimensional emittance defining the beam quality is created at the source. Not only the choice of source but whole low energy section of the facility needs to be investigated through dedicated simulations of collective effects to optimize the technical limitations.

The electron beam properties of linear accelerators are primarily determined by the electron source and can be conserved (adiabatically damped) during the acceleration process and the choice of magnetic optic. The ERL process is to recirculate the accelerated beam into the same linac once again for deceleration. By doing so the energy of the decelerated beam is recuperated back into the linac cavities where it can be reused to accelerate the next fresh beam. The beam is not stored, as in 3rd generation machines, there is only one complete single pass per bunch. Since the energy is recovered, high current and high efficiency common to storage rings is also made possible but with the additional flexibility that a linac offers.

The ERL process suits the advantages of using Superconducting RF (SRF) technology for the linac. The power benefits at low Kelvin operation would allow high accelerating gradients in cw mode. The beam is

accelerated to a final energy, used to create photon radiation, then decelerated and safely dumped at a low energy. This means that GW electron beams can be produced and maintained at power consumptions of MWs, allowing energy efficient operation.

The technological challenges for low energy compact ERLs around the world are focused on reliable and stable operation of SRF based linacs. These test stands are continually improving all aspects of cw mode operation.

The challenges for the large scale multi-turn, multi-user facilities are coupled to the process of these low energy machines. Collective effects common to high charge, ultra-short bunches mean the 6 dimensional phase space defining the beam requires dedicated tracking simulations. Theoretical investigations that will give insight into the new thresholds underlining the key parameters which could drive the community to build such a facility include:

- Preservation of the low emittance throughout the ERL. Both transverse and longitudinal planes need to be conserved. Emittance compensation schemes are required in the space charge dominated low energy stages.
- Single particle analytical investigations underlying the fundamental limitations due to circulating electrons need to be estimated and suitable optic chosen to minimize them.
- Optic is required to suppress the collective radiation effects that determine the nonlinear notion of the phase space evolution required to produce short bunches.
- Common to all recirculation operation, studies to estimate the current thresholds due to Beam Break Up are required using up-to-date cavity measurements. Dedicated analytical programs can be used to optimize the linear optic and suppress the process.
- Numerical studies of many cavity cryomodules are necessary to approximate the extent of frequency bandwidth overlapping between modes. Random distributions can be used to improve the assembling of the long cryomodule.

Current report addressed the above mentioned and other theoretical issues. The CDR reports on the present status of the concept and design of such a multi-turn machine under the working name Femto-Science-Factory (FSF).

The underlying layout and scheme for acceleration and beam recovery of the FSF is well established with numerous public presentations held and publications released. The schematic of the facility is illustrated in Figure 1 and the theoretically achievable beam parameters are summarized in the Table 1.

A fresh beam is produced in the two stage low energy injector and accelerated (shown with green lines) through a structure of split linacs to a final beam energy of 6 GeV. On the way the beam traverses numerous independent orbit arcs with insertion devices (undulators), where magnetic optic is designed to perverse the high beam quality from the injector. At the maximum energy the beam is transferred to a final path by way of the spreaders before entering the long undulator section. The insertion devices create a high brilliance photon light for the multiple user stations. The beam is them symmetrically sent back (shown with red lines) through the arcs and decelerated with a phase shift of 180° back to the injection energy and sent to beam dump. Two independently adjustable modes presently are under

consideration. The high brilliance mode operates on-crest and conserves all planes of motion throughout the machine to preserve the low emittance. On the contrary, the second mode looks to create an ultra-short pulse at the expense of the transverse properties.

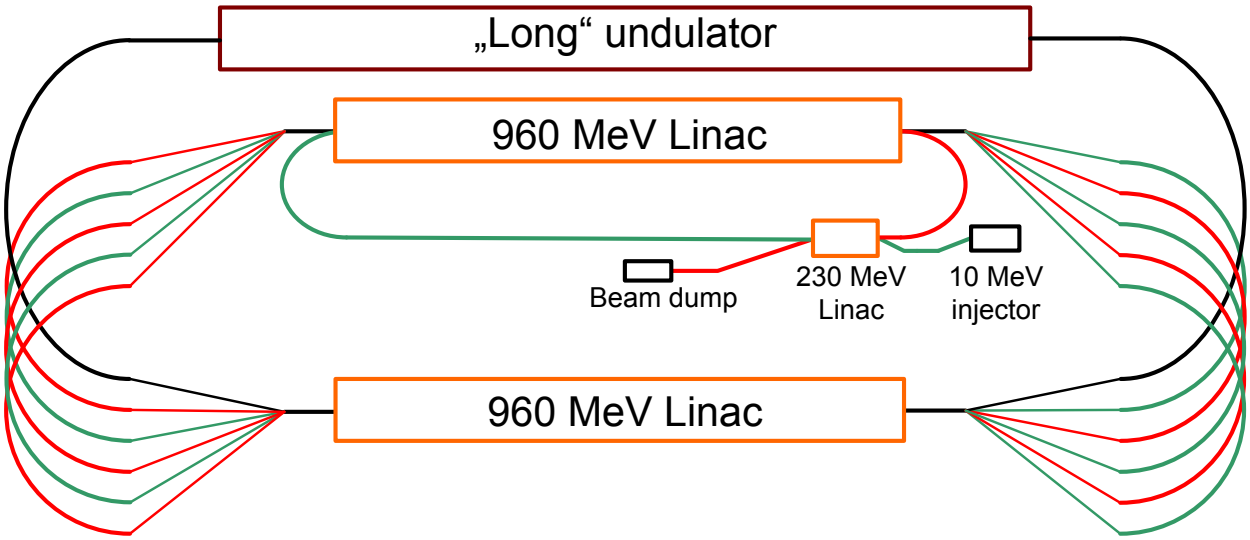

Figure 1. Layout of the multi-turn ERL based synchrotron radiation source FSF. The beam acceleration path is shown in green, deceleration path – in red.

Table 1. Theoretically achievable beam parameters of the FSF

Parameter	High Brilliance mode	Short Pulse mode
Energy, GeV	6	6
Beam Current, mA	20	5
Charge, pC	15	4
Emittance , μm	0.1	0.5
Pulse length, fs	200-2000	10
Av. Brilliance, ph/s/mm^2/mrad^2/0.1%	$7 \cdot 10^{22}$	$4 \cdot 10^{21}$
Peak Brilliance, ph/s/mm^2/mrad^2/0.1%	$8 \cdot 10^{24}$	$5 \cdot 10^{25}$

The goal of the current report is to develop the awareness of the theoretical limitations common to large scale ERL based light sources through dedicated studies. The CDR reports on these findings, how optimization processes were undertaken and presents the acievable parameters. These beam properties are all a magnitude superior than existing 3rd generation light sources and validates ERL based facilities as the next generation.

3 Motivation for the electron and optical beam parameters

The fast and very successful development of the synchrotron radiation sources in terms of achieved scientific impact in the last four decades was due to the significant improvement of the light beam flux and brilliance in the wavelength region, which was practically out of reach for other kinds of light sources. The way from so called 1st generation synchrotron light sources (parasitic use of the radiation from accelerators built for other "science", basically, particle physics) to the 3rd generation dedicated storage ring based facilities with tens of simultaneously available beamlines demonstrates great interest of the scientific community in the new research tool. Recent great achievements (operation of the DESY FLASH facility and recently LCLS) show the potential of further development in the field and map the road to the 4th generation sources.

The vast range of applications requires certain flexibility of the source itself or construction of the light sources dedicated to specific experiments (or groups of experiments).

Our approach is rather to propose an energy recovery linac (ERL-) based installation with a reasonable set of beam parameters emphasizing the important properties given by the nature of ERLs.

Unique features of the multi-turn ERL-based light source include:

- **High peak brilliance of the beam.** This feature is the result of the low emittance of the electron beam (conserved and adiabatically damped during acceleration). Both, transversal and longitudinal emittances, achieved from bright electron beam injectors can be an order of magnitude better than equilibrium emittances of 3rd generation storage rings-based light sources.
- **High temporal resolution.** Low longitudinal emittance allows short radiation pulses down to tens of ps. This gives great advantage in the peak brilliance, as well as for the time-resolved experiments
- **Full transversal coherence.** If the transversal emittance of the electron beam is lower, than $\lambda/4\pi$, the radiation can be transversally coherent. Such low emittances in storage rings are unattainable.
- **Multiple beam energies at the same time in the same installation.** Improves the flexibility and broadens the spectrum of user applications.

Similar to the storage ring-based sources, the energy of the electron beam is limited by radiation effects in the arcs. However, the beam in an ERL does not reach the equilibrium state during short time of several recirculations.

The energy defines the maximum in radiation spectrum in bending magnets and undulators. Undulators are the main sources of the synchrotron radiation in the 3rd generation synchrotron light sources due to their high brilliance. The wave length of the undulator is given by

$$\lambda = \frac{d}{2\gamma^2 k}\left(1+\frac{K^2}{2}\right), \quad (1)$$

where d is the undulator period, γ is the relativistic factor, k is the harmonic number (k=1 for the main harmonic), and K is the undulator parameter given by $K = 0.934 B_0[T] d[cm]$ in practical units.

We propose an ERL-based X-ray light source at wavelengths of 1 Å (ε_γ≈12.4 keV). This typically requires undulators with a period of d=2 cm and K=0.8 at 6 GeV.

$$\lambda = \frac{d}{2\gamma^2}(1+\frac{K^2}{2}) \approx \frac{0.02m}{2\cdot 11742^2}(1+\frac{0.8^2}{2}) \approx 1\,\text{Å}$$

These parameters are chosen as a starting point for this report.

However, the design of a user station is intrinsically connected with the source (undulator) parameters. We consider different type of undulators to find their use in the FSF and discuss their characteristics in more detail in the corresponding section.

The radiation of the bending magnets has a wide spectrum with a critical wave length (which divides the radiation power in two equal parts) given by

$$\lambda_c = \frac{4\pi}{3}\frac{\rho}{\gamma^3}, \quad (2)$$

where γ is the relativistic factor, ρ is the bending radius of the magnet. Although, bending magnets provide orders of magnitude lower brilliance than undulators, their radiation at FSF can be used for some experiments “for free”, like it is in use at many 3rd generation synchrotron light sources.

An ERL-based light source can exceed the 3rd generation sources in the following parameters:

1. Maximal average brilliance in diffraction limited regime (low emittance)
2. Maximal peak brilliance (low emittance and short bunch)
3. Minimal bunch length (short bunch)
4. High bunch degradation (e.g. ERL with FEL. This feature is of paramount importance for other ERLs applications, e.g. as electron beam source in e-p collider, internal target experiments, etc.) (large acceptance)

The first point seems to be the most prominent feature of an ERL-based light source; therefore, optimisation of the average brilliance and diffraction limited regime will be our main focus in this report.

4 FSF design principles

4.1 Accelerator layout

We consider multi-turn ERL linac with a cascade injection as a driver for the FSF. The accelerator consists of (see Figure 2) a bright electron beam injector with the beam energy of 10 MeV; 230 MeV pre-accelerator linac, which is used as a first cascade in the acceleration; two 960 MeV linacs with 3 recirculations of the beam, so that the final beam energy is about 6 GeV; achromatic arcs between the linacs and the beam dump.

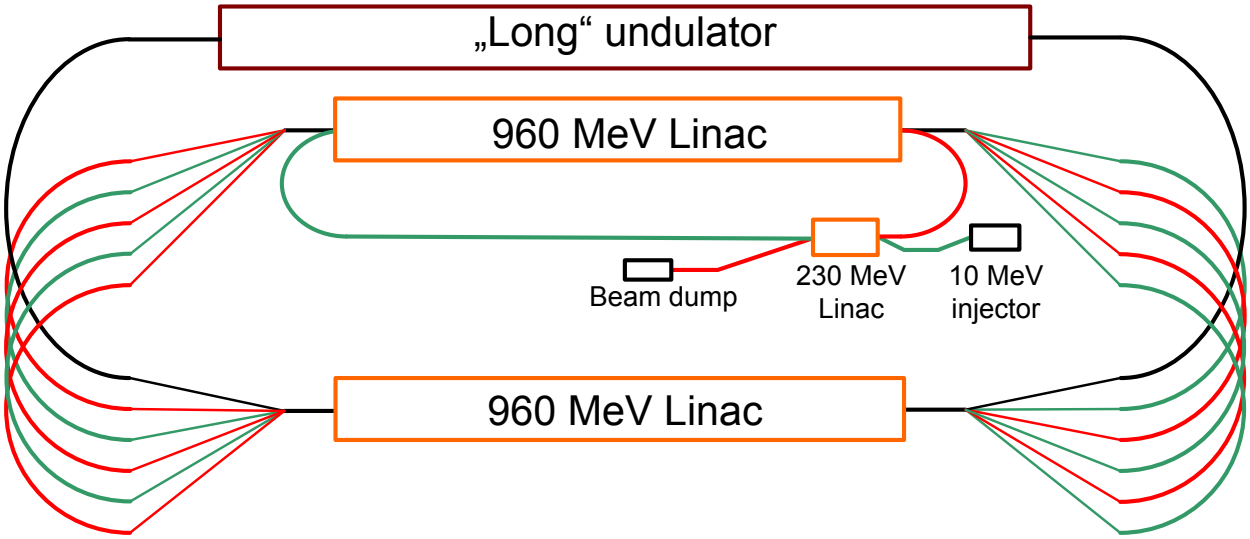

Figure 2. Principal layout of the multi-turn ERL with a cascade injection. The beam acceleration path is shown in green, deceleration path – in red.

The advantage of the cascade injection and the split main linac geometry as well as the choice of the necessary energy gain at every stage of the acceleration will be discussed in details in corresponding sections. Here we just note, that the cascade injection drastically improves the low to high energy ratio in the first 960 MeV linac, which allows a reasonable focusing along the linac for all energies and improves BBU stability of the installation. Split linac geometry allows to separate beams in the arcs, (i.e. the beam on accelerating path have different energy compared to the beam on the decelerating path) so that they are transported in separate vacuum chambers. This way all the beams can be steered separately, and users see only one beam in each undulator (installed in arcs with 5, 4, 3, etc. GeV energy).

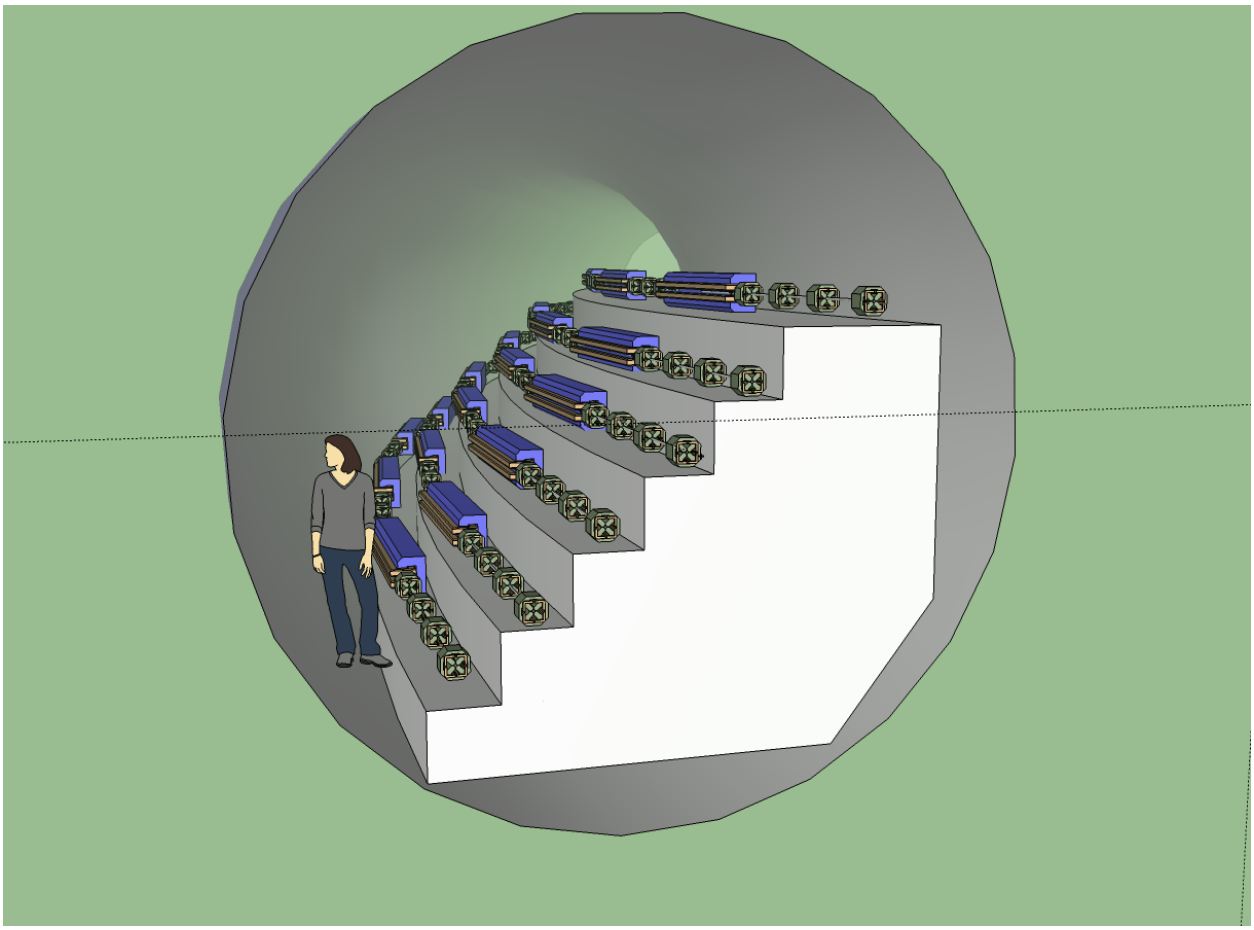

Figure 3. FSF arcs in a tunnel.

The initial assumptions

- Beam energy 6 GeV
- rms normalized emittance ≥ 0.1 mm·mrad
- Average current ≈ 5 – 20 mA (60 mA is the present world record for average current from photocathode guns in cw mode)
- rms bunch length 1 ps – 10 fs.

4.2 Beam parameters

Main parameters of the electron and photon beams in the FSF are listed in the following Table 2. The most important parameters of the FSF facility are the peak and average brilliance of the photon beam. The critical electron beam parameters are transverse emittance, pulse length and energy spread in undulators. Next subsections overview the limiting factors, defining these parameters.

Table 2. Main parameters of the electron and photon beams

Accelerator/beam parameters	High brilliance mode	Short pulse mode
E, GeV	6	6
<*I*>, mA	20	5
Q, pC	15	4
$\varepsilon_{\perp n}$, μm	0.1	0.5
$\varepsilon_{/\!/}$, keV·mm	3	3
τ, fs	200-2000	10
<*B*>, ph/s/mm^2/mrad^2/0.1%	$7 \cdot 10^{22}$	$4 \cdot 10^{21}$
B_{peak}, ph/s/mm^2/mrad^2/0.1%	$8 \cdot 10^{24}$	$5 \cdot 10^{25}$
I stage injector (no recovery)		
E, MeV	10	10
τ, fs	2000	2000
II stage injector (BERLinPro)		
E, GeV	0.1	0.1
τ, fs	200-2000	200
Undulators	5 /arc x 6 energies x 2 arcs+1	
d, cm	4 (2)	
Number of periods	1000 („long“ undulator with 3000)	
Linacs	2 linacs x 9 cryomodules x 8 cavities x 7cell (bERLinPro type) +2 cryomodules (Injector)	
Accelerating gradient, MV/m	17	
Energy gain per linac, GeV	1	
f, GHz	1,3	

4.2.1 Transverse emittance

The main advantage of the linac-based light sources over storage rings is the possibility to preserve the initial transverse electron beam emittance $\varepsilon_\perp$ from the injector. The emittance is additionally adiabatically damped during acceleration, giving a possibility to achieve sub-Å values if the final beam energy is high enough. The figure of merit of the electron beam injectors is a normalized emittance $\varepsilon_{n\perp} = \varepsilon_\perp \cdot \beta\gamma$, which can be conserved during acceleration. Feasibility of low emittance beams is successfully demonstrated in linac based X-ray FEL sources (Flash, LCLS).

The limit on the transverse emittance of the electron beam is set mainly by the space charge forces acting on the bunch at a low energy (near the cathode). Therefore, as fast as possible acceleration on the one hand and a low bunch charge on the other are desirable.

The highest accelerating fields are achievable in radiofrequency (RF) electron guns. For the 4th generation light sources continuous operation (cw mode) is desirable (if not a must), therefore development of the superconducting RF guns (SRF guns) is necessary. This type of electron guns promises to reach the best transverse emittance in the perspective.

Another important issue is the emittance conservation during beam transport and acceleration. To deal with it we treat an emittance compensation technique, effects of quantum fluctuations of synchrotron radiation, coherent synchrotron radiation, etc. in separate chapters.

4.2.1.1 Transverse beam emittance in storage rings

In a storage ring transverse beam emittance is a compromise between two processes:

- damping of the transverse (betatron) oscillations by synchrotron radiation
  and
- excitation of the transverse oscillations due to quantum nature of the synchrotron radiation

At equilibrium the emittance of a stored beam is given by [1]

$$\varepsilon_x = \frac{55}{32\sqrt{3}} \frac{r_e}{\alpha} \frac{\gamma^2}{1-D} \frac{\left\langle \frac{H(s)}{R^3} \right\rangle}{\left\langle \frac{1}{R^2} \right\rangle}, \quad (3)$$

where r_e and α are the classical electron radius and fine structure constant, γ is the relativistic factor, R is the bending radius in magnets, <…> means average over one turn, D and $\mathrm{H}(s)$ are the accelerator lattice parameters given by

$$\mathrm{H}(s) = \gamma\eta^2 + 2\alpha\eta\eta' + \beta\eta'^2, \quad (4)$$

$$D = \frac{\frac{1}{T}\oint P_0 \eta(\frac{1}{R} + 2\frac{B'}{B})dt_0}{\langle P \rangle}, \quad (5)$$

Here α, β, and γ are the Twiss parameters, η is the dispersion function of the lattice, ' means derivative with respect to s (along the accelerator), P is the radiation power, B and B' are the magnetic field and its gradient in the bending magnets, T is the circulation time in the ring.

Significant effort was invested in the design of low emittance lattices for the storage ring-based synchrotron light sources. 2nd and 3rd generation sources are emittance optimized. The limits of the circular machines in this respect are well understood.

4.2.1.2 Transverse beam emittance in storage rings vs. linacs

In short, the advantage of the linac-based light sources over ring-based ones follows from the comparison of transversal emittances:

$$\varepsilon_x = \frac{\varepsilon_0}{\gamma} \text{ vs. } \varepsilon_x \sim \frac{\gamma^2}{N^3}, \quad (6)$$

where ε_0 is the initial emittance in the linac at injection, N is the number of bending magnets in the ring, γ is the relativistic factor.

The comparison (6) shows that with the growing energy in a linac emittance gets lower. On the contrary, the storage ring (radiation induced) emittance is growing quadratic with the energy.

The usual way to counteract the emittance growth in a storage ring based synchrotron light source is to split the bending arc into many achromatic sections with short bending magnets (increase N in). This possibility is exploited in the so called "Ultimate Storage Ring" approach, which is another possibility for further improvement of the synchrotron light sources [see e.g. [4]].

It should be noted that the vertical emittance in a storage ring can be significantly below the value given by (3) since there is ideally no vertical dispersion in the ring. Operating installations usually demonstrate a small coupling between horizontal and vertical emittances which defines the vertical emittance (of the order of 1% of the horizontal one). Linac-based sources on the other hand provide nearly equal emittances in both transversal planes ("round" beams).

4.2.2 Longitudinal emittance

Due to the adiabatic dumping similar to the damping of the transverse emittance, low longitudinal emittance from the injector is important for the linac-based future light sources. The processes leading to the growth of longitudinal emittance in a linac is usually the nonlinearity of the accelerating field (RF curvature). Short bunches from the cathode are, therefore, necessary to minimize this growth. This

drives the choice of the photocathode guns as an electron source for an ERL. Second order dispersive terms in arcs can be another important source of the longitudinal emittance growth in an ERL.

We address the issues of bunch compression, reduction of correlated energy spread and second order non-linearity in the corresponding chapters.

The longitudinal bunch parameters in a storage ring are given here for comparison [in [1], 10.25].

Equilibrium energy spread in a storage ring:

$$\left(\frac{\sigma_E}{E}\right)^2 = \frac{55}{32\sqrt{3}}\frac{r_e}{\alpha}\frac{\gamma^2}{2+D}\frac{\left\langle\frac{1}{R^3}\right\rangle}{\left\langle\frac{1}{R^2}\right\rangle}, \tag{7}$$

Equilibrium bunch length [in [1], 10.27]:

$$\sigma_{c\Delta t}^2 = \left(\frac{c\alpha_p}{\omega_s E}\sigma_E\right)^2 = \frac{55\pi}{16\sqrt{3}\alpha}\frac{\gamma^3}{2+D}\frac{e\alpha_p}{hV_0\cos\psi_s}\frac{\langle R\rangle^2\left\langle\frac{1}{R^3}\right\rangle}{\left\langle\frac{1}{R^2}\right\rangle}, \tag{8}$$

Here again r_e and α are the classical electron radius and fine structure constant, γ is the relativistic factor, R is the bending radius in magnets, <…> means average over one turn, D is the accelerator lattice parameter given by (5), E is the beam energy, α_p is the momentum compaction factor, V_0 and ψ_s is the amplitude and phase of the accelerating voltage, h is the harmonic number of the RF, ω_s is the RF frequency.

A quick analysis of (7) shows the linear dependence of the equilibrium energy spread on the beam energy in a storage ring. This is to compare with inverse dependence in a linac (e.g. if no correlated energy spread is created for the bunch compression). Linacs have again the advantage in this respect at high energies.

As follows from (8), the parameters for optimisation of a short bunch mode in a ring are momentum compaction factor α_p (“isochronous ring”), RF amplitude V_0, and harmonic number h.

An important experiment to achieve short bunch lengths in a ring-based light source is an ongoing effort at BESSY called BESSY^{VSR}(see e.g. [2,3]).

4.2.3 Average brilliance

We define brilliance (other commonly used name is spectral brightness) as a number of photons per unit surface of the source per solid angle per second in a definite spectral interval.

$$[B] = \frac{\text{Number of photons}}{\text{mm}^2 \cdot \text{mrad}^2 \cdot \text{sec} \cdot 0.1\%\text{bandw.}}, \tag{9}$$

In other words, brilliance is the photon density in the 6-dimensional phase space.

Undulators, radiation sources with high brilliance, are used in the 3rd generation light sources as generators. They provide high power nearly monochromatic radiation with a bandwidth

$$\frac{\Delta\lambda}{\lambda} \sim \frac{1}{kN}, \tag{10}$$

where N is the number of undulator periods, k is the harmonic number of the undulator radiation.

In order to achieve high brilliance a small source size with a low photon beam divergence is necessary. The radiation divergence angle for a single electron in an undulator [1] is ψ.

$$\psi \sim \frac{1}{\gamma}\sqrt{\frac{1+0.5K^2}{2N}}, \tag{11}$$

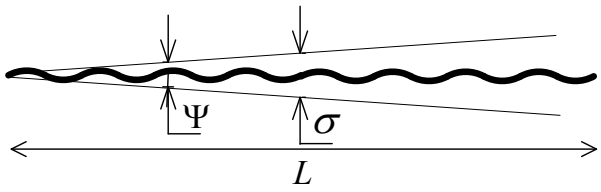

Figure 4. Source size of the undulator radiation.

Transverse "electron size" (size of an electron from the point of view of an observer of its light) in an undulator of length $L=Nd$ is σ (see Figure 4).

$$\sigma \approx \frac{L\psi}{2} \sim \frac{L}{2\gamma}\sqrt{\frac{1+0.5K^2}{2N}}, \tag{12}$$

The source divergence (11) and size (12) are given for the case of radiation from a single electron and are the same for the case electron beam size and divergence are lower, that those of the radiation. Therefore, for a low electron beam emittance

$$\varepsilon << \frac{\sigma}{2}\cdot\frac{\psi}{2} \sim \frac{d}{16\gamma^2}\left(1+0.5K^2\right) = \frac{\lambda}{8}, \tag{13}$$

or more exactly

$$\varepsilon \le \frac{\lambda}{4\pi}, \tag{14}$$

low energy spread of the beam

$$\frac{\Delta E}{E} << \frac{1}{2}\frac{\Delta\lambda}{\lambda} = \frac{1}{2kN}, \tag{15}$$

and ideal undulator alignment the brilliance reaches its theoretical maximum.

$$B_{av,\max} = \dot{N}_{ph}\frac{4/\lambda^2}{d\omega/\omega},, \tag{16}$$

In case (14) is fulfilled the light source is called “diffraction limited” and has full (high) transversal coherence (large fraction of photons is coherent).

Normalized transversal emittance of 0.1 mm·mrad is necessary for the source to be diffraction limited at the wavelength of 1 Å and electron beam energy 6 GeV.

$$\varepsilon_n \approx \gamma\frac{\lambda}{4\pi} \approx 12000\frac{1\,\mathring{\mathrm{A}}}{4\pi} \approx 0.1\mathrm{mm}\cdot\mathrm{mrad}, \tag{17}$$

We take this value as the goal for our design.

The theoretical maximum for the average brilliance $B_{av,\max}$ of an undulator in the diffraction limited regime is

$$B_{av} \approx 5\cdot 10^{23}\frac{ph}{s\cdot 0.1\%\cdot mm^2\cdot mrad^2}, \tag{18}$$

where the numerical value is given for K=0.8, I_{av}=20 mA, N=1000 and

$$\dot{N}_{ph} = \pi\alpha N\frac{d\omega}{\omega}\frac{I_{av}}{e}g(K)$$
$$g(K) = \frac{K^2[JJ]}{1+0.5K^2} \tag{19}$$

is taken for the average photon flux [1].

4.2.3.1 Higher harmonics

A separate note about brilliance of the higher harmonics of undulator radiation should be made at this point. The condition for the beam emittance, given by (14), is true for a k-th harmonic as well as for the main wavelength. However, the condition (15) for the energy spread in the beam depends on the harmonic number k. Therefore, at a given energy spread in the beam the brilliance of the source will be reduced for high harmonics

$$k > \frac{1}{2N\dfrac{\Delta E}{E}}, \tag{20}$$

For such harmonics the calculation of the actual spectrum of radiation is necessary.

4.2.3.2 Proposed undulators for the FSF

Parameters of possible FSF undulators are summarized in the following Table 3.

Table 3. Main parameters of the FSF undulators.

Undulator parameters	Type 1	Type 2
N (number of periods)	3000	1000
d (period), cm	2	4
N_{sec} (number of sections)	15	10
K	0 - 1.0	0 - 2.5
B_{max}, T	0.5	0.67
Max. brilliance $B_{av,\,max}$, $\frac{ph}{s\cdot 0.1\%\cdot mm^2\cdot mrad^2}$	$7\cdot10^{22}$	$3.1\cdot10^{22}$ (at 6 GeV)
Max. peak brilliance $B_{peak,\,max}$, $\frac{ph}{s\cdot 0.1\%\cdot mm^2\cdot mrad^2}$	$5\cdot10^{25}$	$3\cdot10^{25}$ (at 6 GeV)

The brilliance for the undulators is calculated according to

$$B_{av,\max} = \frac{\dot{N}_{ph}}{4\pi^2\,\sigma_x\sigma_{x'}\sigma_y\sigma_{y'}(d\omega/\omega)}\frac{1}{\sqrt{1+8\pi(Nk\delta)^2}}, \tag{21}$$

The brilliance is reduced from the diffraction limit (16) due to betatron motion, apparent source size, increased spectral width of the radiation due to energy spread in the beam, sectioned undulator, etc.

For the beam sizes σ_x, σ_y and divergences $\sigma_{x'}, \sigma_{y'}$ we use [1, p.852]

$$\sigma_x^2 = \frac{\lambda L}{8\pi^2} + \varepsilon\beta_{\min} + \frac{\varepsilon L_{\sec}^2}{12\beta_{\min}} + \left(\frac{dK}{2\pi\gamma}\right)^2, \tag{22}$$

$$\sigma_y^2 = \frac{\lambda L}{8\pi^2} + \varepsilon\beta_{\min} + \frac{\varepsilon L_{\sec}^2}{12\beta_{\min}}, \quad (23)$$

and

$$\sigma_{x',y'}^2 = \frac{\lambda}{2L} + \frac{\varepsilon}{\beta_{\min}}, \quad (24)$$

where $L \sim Nd$ is the full length of the undulator (including the length between the sections), L_{sec} is the length of a section, K is the undulator parameter.

By an undulator section we mean a part of the undulator corresponding to one period of the beta-function. The section can consist of a number of physical undulators.

The same beta-function in each section with $\beta_{\min}$ in the middle of the section and a round beam with $\beta_x = \beta_y$ are assumed.

We take into account the widening of the radiation spectrum due to the energy spread in the electron beam taking a factor (for comments on the coefficient used here see Appendix A: Brilliance of the undulator radiation in the case of an electron beam with an energy spread)

$$\frac{1}{\sqrt{1 + 8\pi(Nk\delta)^2}}, \quad (25)$$

in the brilliance. As estimation for the energy spread we take first the spread due to incoherent synchrotron radiation $\delta \sim 10^{-4}$. This unavoidable contribution seems to be the main source of the energy spread for the long bunch case in FSF (high brilliance mode).

The expression (21) gives good approximation and was benchmarked to “brill“ script in PAW, based on [6], as well as to WAVE code [5].

Figure 5 compares the brilliance curves of the FSF Type1 and Type2 undulators installed in all arcs (electron beam energies 1 - 6 GeV) with 3rd generation light sources.

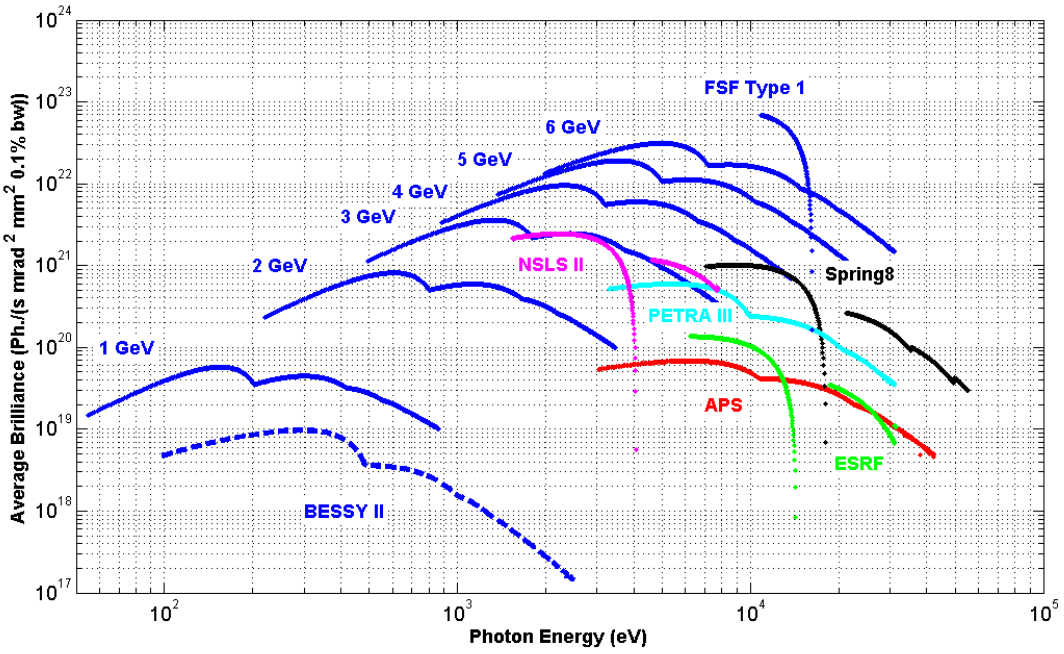

Figure 5. Average brilliance of synchrotron light sources. 1-6 GeV are the Type 2 FSF undulators.

That portion of the flux that is transversely coherent is given by [6]

$$\breve{S}_c = B_n\left(\frac{\lambda}{2}\right)^2 = \frac{\breve{S}_n\lambda^2}{(4\pi)\sigma_{Tx}\sigma_{Ty}\sigma_{Tx'}\sigma_{Ty'}}, \tag{26}$$

The plots of the coherent fraction of undulator radiation at different electron beam energies in FSF are shown in Figure 6. For a more rigorous discussion on the accurate brilliance and coherent fraction definitions see [37].

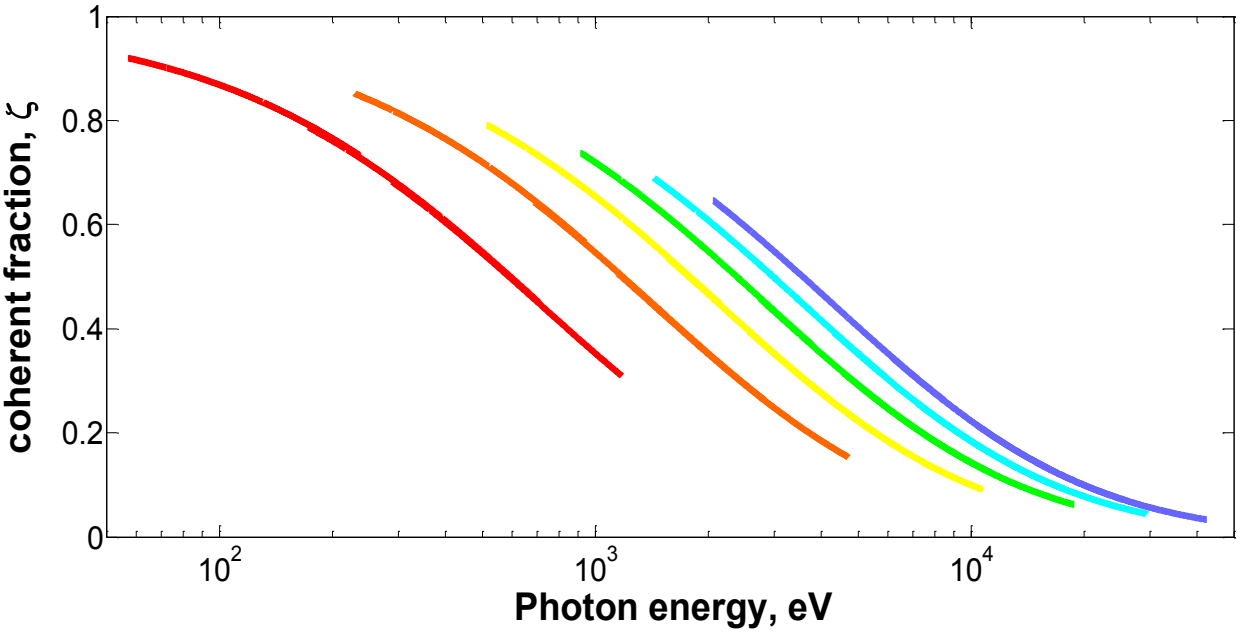

Figure 6. Coherent fraction of FSF Type2 undulators installed in 6 arcs at the beam energies 1 (red) – 6 (blue) GeV. 1st through 5th harmonics are taken into account for each beam energy.

4.2.4 Peak brilliance & short pulse

Bunch compression is required to achieve high peak brilliance. The compression limited by the incoherent and coherent synchrotron radiation effects. Too strong compression leads to an increased transverse emittance. Now consider a case with rms length of 10 fs and average current 5 mA constituting a peak current of 150 A. The horizontal emittance will as a result grow about an order of magnitude hence the horizontal bunch size will increase by a factor of three.

$$\frac{d\dot{N}}{d\Omega} = 1.7466 \cdot 10^{23} \cdot (6GeV)^2 \cdot 150A \cdot 1000^2 \cdot 0.322 \cdot 10^{-3} \approx 3 \cdot 10^{29} \frac{ph}{s \cdot rad^2 \cdot 0.1\%} \approx 3 \cdot 10^{23} \frac{ph}{s \cdot mrad^2 \cdot 0.1\%},$$
$$B_p = \frac{d\dot{N}}{d\Omega} \frac{1}{\sigma_x \sigma_y} \approx \frac{3 \cdot 10^{23}}{22\mu m \cdot 70\mu m} \frac{ph}{s \cdot 0.1\% \cdot mm^2 \cdot mrad^2} \approx 2 \cdot 10^{26} \frac{ph}{s \cdot mrad^2 \cdot 0.1\%}. \quad (27)$$

This increase in beam size will cancel out any proposed gain in current and the peak brilliance remains as before. Radiation production however is not the main reasoning behind the scientific requirement of short pulses. The bunch length acts as a degree of accuracy in many experiments (the principle of X-ray absorption spectroscopy (XAS) for example).

Figure 7 shows the peak brilliance curves of the FSF undulators in comparison with other operating 3rd generation synchrotrton light sources. Apparently lower peak brilliance in 1 GeV FSF arc is due to relatively long electron bunch here (compression is finished in 2 GeV arc). The curves are given for the last undulator in each arc at acceleration. Maximal peak brilliance depends on the bunch charge. The curves shown in the picture correspond to an optimum charge :1pC (6, 5, 4 GeV) 3 pC (3 GeV), and 5 pC (2 and 1 GeV).

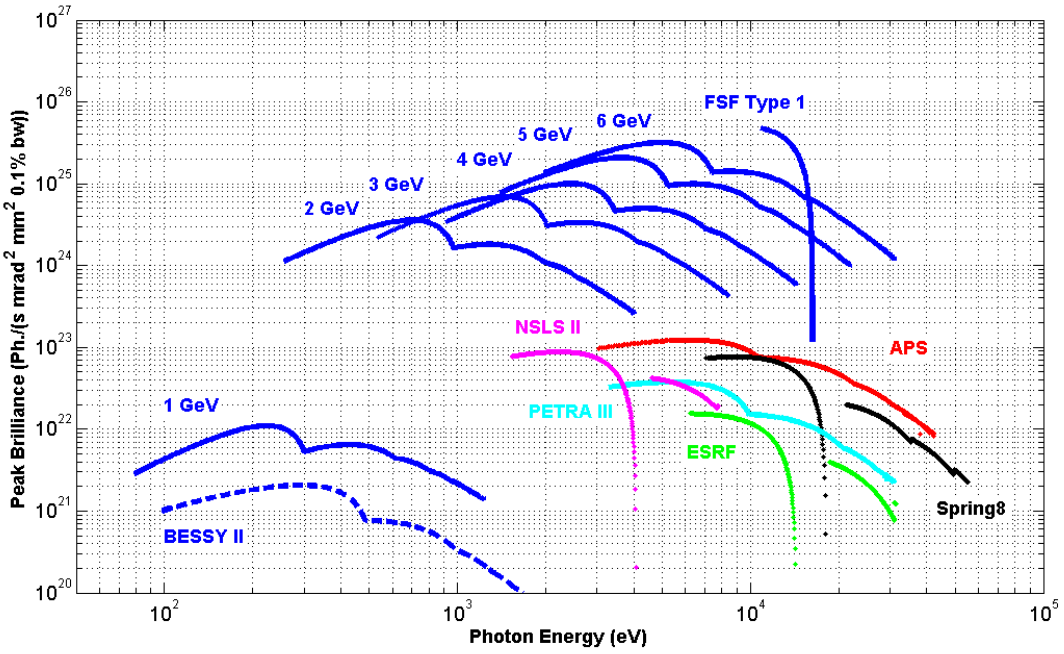

Figure 7. Peak brilliance of synchrotron light sources. 1-6 GeV are the Type 2 FSF undulators.

5 Beam dynamics issues

5.1 FSF injector

Beam parameters (transverse and longitudinal emittance) achieved in the injector is the key to the maximal brilliance of the FSF. They also define the efforts one should take for the design of the rest of the accelerator, since preserving the emittances for a low emittance machine is not trivial. The goal for the value of the transverse emittance set in Ch.4 (0.1 mm·mrad normalized) is challenging but within the reach of the modern guns. Emittance compensation technique must be used to preserve the emittances in the low energy part of the accelerator.

High brightness electron sources generating short pulses are based on the photocathode guns. There are a number of operating photocathode sources in DC guns, normal conducting radiofrequency (RF) guns, and superconducting RF (SRF) guns. The latter have the highest potential for the future high brightness sources since they combine the advantages of cw operation, high peak field on the cathode, and excellent vacuum conditions (of advantage for the life time of high QE semiconducting photocathodes). Due to this reason an SRF gun is considered as a base line design for the FSF. However, the excellent results of the Cornell ERL Injector group show that even a much more technologically mature solution with a DC photocathode gun could be sufficient for our needs.

Space charge effects in the injector are strong. If we set some goal emittance value, they limit the bunch charge. Modeling of the beam dynamics must be done with an appropriate space charge modeling program. We use ASTRA code (version 3) by K.Flöttmann [8].

The layout of the injector is shown in Figure 8. From the beam dynamics point of view it consists of a superconducting RF photo gun and booster in a single cryomodule, merger section and two matching sections of 4 quadrupoles each.

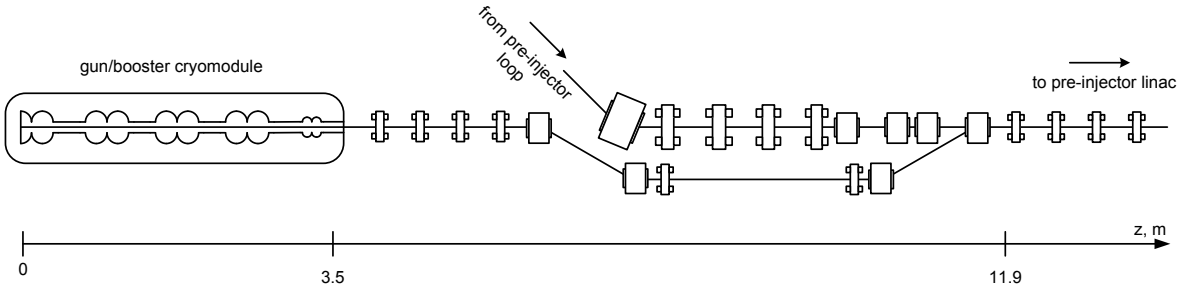

Figure 8. General layout of the FSF injector.

To generate the 0.1 mm·mrad transverse emittance bunch with maximal charge, long laser pulse is necessary. This initially long bunch must be compressed further. A 3rd harmonic cavity is included in the cryomodule to linearize the longitudinal phase space of the bunch for better compression.

As a merger section 4-dipole bypass is proposed. The advantage of the chicane in our case is the absence (at least in the ideal world) of dispersion to all orders. This is important, since (quite large, ~1%) energy spread in the bunch is needed for the compression. With other merger types (e.g. dogleg) second order dispersion would be detrimental for the transverse beam emittance. The bypass dipoles are 20deg 30 cm long. The distance between them (L= 1.10 m) defines R_{56} of about 25 cm (needed for the bunch compression) and trajectory offset D~50 cm, which should be enough to install the high energy beam line elements. Four quadrupole magnets between the booster and merger and four between merger and pre-injector linac are necessary for the transverse beam matching and emittance compensation. Two (weak) quadrupoles in the chicane are for the possible correction of the “space charge dispersion”.

A solenoid usually used for the emittance compensation in high brilliance guns has quite strong aberrations which limit the beam size in the solenoid. On the other hand, in an SRF gun the solenoid cannot be positioned closely to the gun cavity since the cavity quality factor Q is vulnerable to residual fields at cool down as well as in operation. Therefore, we choose another solution for the beam focusing after the gun: focusing with the RF field of the first cavity in the booster. This way this unavoidable and quite strong focusing is used for a benefit. On the other hand, this allows to put the gun and the booster in a single cryomodule.

We start with a particle distribution on the cathode. The transversally flat-top laser spot profile on the cathode is assumed with a full radius of 0.2 mm. The longitudinal profile of the beam is also flat-top (plateau distribution) with a 50 ps length and 5 ps rise/fall time (rms. length of ~15 ps). Alternatively,

Gaussian longitudinal profile cut off at ±3σ and rms. length of 15 ps was used. See "Appendix B: Electron beam parameters in FSF injector" for the bunch parameters on the cathode and details on ASTRA input files.

5.1.1 Beam parameters from FSF injector

Table 4. Expected beam parameters at the exit of the injector.

Parameter	Value
Beam momentum pc	10 MeV
Max average beam current	20 mA
Max bunch charge	15 pC
Longitudinal emittance (rms)	>1 keV·mm
Bunch length (rms)	0.5 - 3 ps
Transversal normalized emittance (rms)	0.07 - 0.3 mm·mrad

5.1.2 Effects leading to emittance growth in injector

5.1.2.1 Transverse space charge

The space charge effects change the motion of charged particle beam with relatively low energy and high peak current [10]. We can neglect space charge only if

$$\begin{aligned} &\frac{\varepsilon_y^2}{y^3} >> \frac{I}{I_0(\beta\gamma)^3}\frac{1}{x+y} << \frac{\varepsilon_x^2}{x^3}, \\ &\frac{5}{16}\frac{I}{\varepsilon I_0(\beta\gamma)^3}L << 1. \end{aligned} \quad (28)$$

In opposite case we have a space charge dominated beam. If the longitudinal size in the beam frame is larger than transversal, we can divide the bunch into slices, neglect interaction between them and consider the motion of slices independently from each other [12].

5.1.2.2 Longitudinal inhomogeneity of space charge density

The equations of slices motion in the space charge dominated beam are

$$x'' + \frac{(\beta\gamma)'}{\beta\gamma} x' = \frac{j}{x+y} - gx,$$
$$y'' + \frac{(\beta\gamma)'}{\beta\gamma} y' = \frac{j}{x+y} - hy, \quad (29)$$

where x and y are rms sizes of the slices.

Slices start at the cathode with the same radii and different current density. The motion of slices in phase space is different from each other. It leads to increase of the phase space area, filled with particles. As a result the emittance grows.

The (linearized) equations for the differences between rms slice size and "reference" slice size are given below:

$$\Delta x'' + \frac{(\beta\gamma)'}{\beta\gamma} \Delta x' = -\frac{j(\Delta x + \Delta y)}{(x+y)^2} - g\Delta x,$$
$$\Delta y'' + \frac{(\beta\gamma)'}{\beta\gamma} \Delta y' = -\frac{j(\Delta x + \Delta y)}{(x+y)^2} - h\Delta y, \quad (30)$$

where Δx and Δy are differences between rms slice sizes. These are equations of two coupled oscillators (with damping, if $\beta\gamma$ changes due to acceleration). It means that the slice sizes oscillate near the reference slice sizes and the frequencies of the oscillation (coupled pendulum with two eigenmodes) do not depend on the amplitude if the difference is small [10]. After half a period of the oscillation the slice size coincides again with the reference slice. At this point emittance will be also minimal ("emittance compensation").

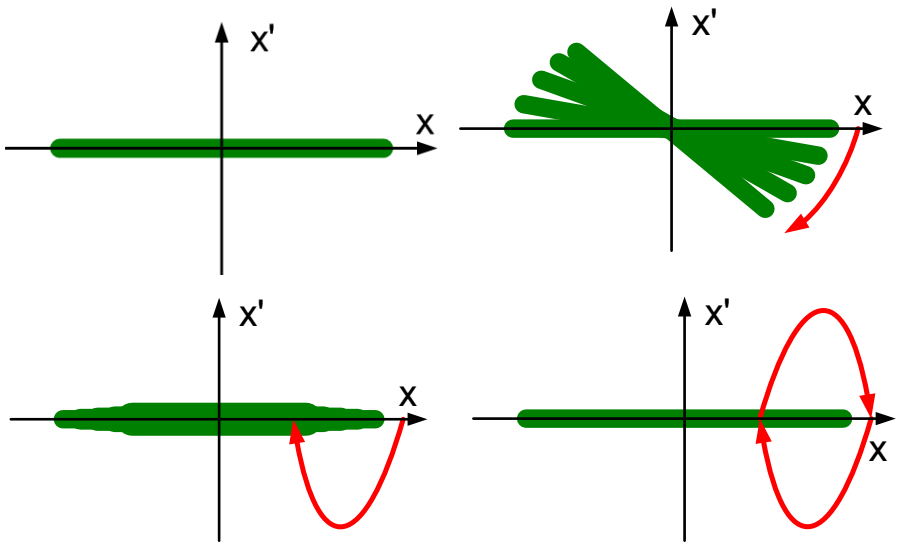

Figure 9. Slices motion.

In an axi-symmetrical system a solenoid is used to make "emittance compensation" at a certain point, usually in the booster. Estimations show, however, that the beam in the merger of FSF is still space charge dominated, therefore it is necessary to have emittance compensation point in the pre-injector linac. For a system without axial symmetry the emittance compensation technique should be used to make both x - and y - emittances minimal at the middle of the linac [11].

5.1.2.3 *Energy change in dispersion section due to longitudinal space charge ("space charge dispersion").*

In our case rms longitudinal beam size in the beam reference frame $\gamma\sigma$ is much more than the transversal beam size r. The longitudinal electrical field in the accelerator's frame can be estimate as:

$$E_z \approx \frac{Q}{\gamma 2\pi\varepsilon_0 r\sigma} \tag{31}$$

where Q is the bunch charge, r – transversal radius, σ – bunch length, ε_0 – permeability of vacuum. In the injector after the booster longitudinal electrical field is about:

$$E_z \approx \frac{15.4\cdot 10^{-12} C}{14\cdot 2\pi\cdot 8.854\cdot 10^{-12}\cdot 0.002m\cdot 0.01m} \approx 1keV/m \tag{32}$$

The main impact of the longitudinal electrical space charge field on the beam dynamics is changing of particles energy. The changing of the particle energy in a drift with non-zero dispersion δ_{sc} can be the main reason of emittance growth in the merger.

$$\delta_{sc} = \frac{\int E_z dz}{E_0} \approx \frac{E_z \cdot L}{E_0} \tag{33}$$

where L is the length of a dispersion drift.

5.1.2.4 *Mismatch of slice centers at the end of dispersion section*

The particle offset at the end of merger is about:

$$\begin{aligned} \delta x &= \int \frac{\partial \delta_{sc}}{\partial s}\cdot D ds \approx \delta_{sc}\overline{D}, \\ \delta x' &= \int \frac{\partial \delta_{sc}}{\partial s}\cdot D' ds \approx \delta_{sc}\overline{D}', \end{aligned} \tag{34}$$

D is the value of dispersion in merger. The linear offset of slice center at the end of the merger can be partly compensated by adjusting the dispersion at the end of merger (in this case the merger is not exactly achromatic). The changes of the particle energy due to longitudinal space charge field are mainly non-linear. It leads to emittance degradation in a drift with non-zero dispersion. The estimation of this effect gives for the emittance growth

$$\Delta\varepsilon^2 = \delta x^2 \langle x'^2 \rangle + \delta x'^2 \langle x^2 \rangle - \delta x \delta x' \langle x' x \rangle, \quad (35)$$

If there is no correlation between particles coordinate and angle, we can simplify.

$$\frac{\Delta\varepsilon}{\varepsilon} \approx \sqrt{\frac{\delta x^2}{x_{rms}^2} + \frac{\delta x'^2}{x'^2_{rms}}} \approx \sqrt{\left(\frac{\delta_{sc} \cdot D}{x_{rms}}\right)^2 + \left(\frac{\delta_{sc} \cdot D'}{x'_{rms}}\right)^2} \approx \frac{E_z L}{E_0} \sqrt{\left(\frac{D}{x_{rms}}\right)^2 + \left(\frac{D'}{x'_{rms}}\right)^2}, \quad (36)$$

where x_{rms} is the bunch size. Merger design with the shortest drift with non-zero dispersion seems to be the only way to avoid this effect.

5.2 Synchrotron radiation effects

The synchrotron radiation (SR) in bending magnets is one of the main reasons of the beam degradation. Ways of emittance preservation for incoherent radiation are well known, and for ERLs they are the same as for synchrotrons. Methods of emittance preservation for Coherent Synchrotron Radiation (CSR) are based on the manipulation of the betatron phase between identical bend sections [13] or the optimization of lattice functions using extension of R-matrix formalism [14].

5.2.1 Coherent SR

We need a beam of 0.1 mm·mrad normalized emittance and longitudinal size down to 10 fs. For such a beam CSR becomes an issue due to shorter bunch length and smaller emittance in comparison with, e.g. synchrotrons. One of the main CSR induced problems is the transversal emittance degradation. Thus, studies of emittance suppression of CSR-caused dilution become a demand. Logical way to solve this problem is developing emittance conservation optics [15, 16]. To develop such optics for ERL arcs consider the basic CSR model in one-dimensional approximation (1D CSR).

5.2.2 Geometrical parameters of CSR and 1D approximation

Consider applicability of 1D approximation of coherent radiation. Let a bunch with a rms length σ_z, total transversal size a move on a bending radius R inside a vacuum chamber with diameter D. Geometrical parameters of CSR are defined as in [17].

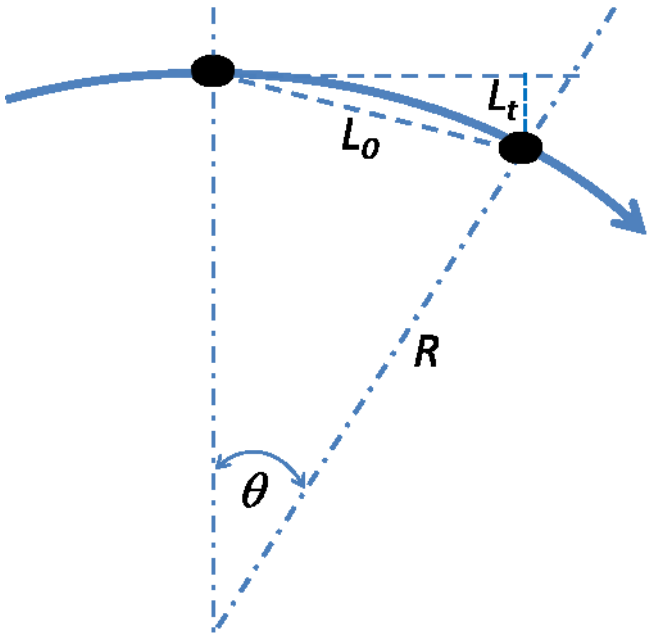

Figure 10. Geometrical parameters of CSR.

L_0 is *overtaking distance*, this is the distance the beam passes, until radiation from the tail overtakes the head. Θ is *overtaking angle*. L_t is *characteristic transverse distance*; this is the deviation of tangent from the path of the beam at the overtaking distance

$$\begin{aligned} L_o &= 2\sqrt[3]{3\sigma_z R^2}, \\ \theta &= \frac{L_o}{R} = 2\sqrt[3]{3\sigma_z / R}, \\ L_t &= \frac{\theta L_o}{2} = 2\sqrt[3]{9\sigma_z^2 R}. \end{aligned} \tag{37}$$

The characteristic transverse distance L_t can be compared with other transversal parameters of the problem: transversal bunch size and vacuum chamber diameter D. If $D < L_t$ shielding becomes important [18, 19]. If the transversal bunch size a is smaller than the characteristic transverse distance L_t, 1D model can be used [20].

We consider 1D CSR without shielding case realized in ERL based light sources. As an example we take following beam parameters: σ_z≈30 μm, normalized emittance ε_n≈0.1 mm·mrad, lattice function β≈10 m, γ≈10^4, R≈10 m, D≈20 mm)

$$a \approx 4\sqrt{\frac{\varepsilon_n}{\gamma}\beta} \approx 30\,\mu m << L_t \approx 8mm < D = 20mm \tag{38}$$

5.2.3 Emittance preservation at 1D CSR approximation

1D CSR wake depends on a longitudinal bunch profile and geometry of bends and do not depend on transversal bunch shape. All particles in one slice get the same shift of horizontal coordinate δx and angle $\delta x'$. This shift depends only on the longitudinal bunch profile and longitudinal coordinate of the slice.

Let's calculate the deflection of an electron due to the CSR in this approximation. $\delta\mathbf{X}$ is a vector (δx, $\delta x'$) of an electron position in the phase space. $\mathbf{R}_6$ is a vector (R_{16}, R_{26})

$$\delta\mathbf{X} = \int_{s_1}^{s_2} \mathbf{R}_6(s|s_2)\frac{dE}{E_0 ds}ds, \tag{39}$$

where dE is a energy loss of electron due to 1D CSR wake, E_0 is beam energy.

$$\begin{aligned} R_{16}(s|s_2) &= -R_{11}(s|s_2)D(s) - R_{12}(s|s_2)D'(s) \\ R_{26}(s|s_2) &= -R_{21}(s|s_2)D(s) - R_{22}(s|s_2)D'(s) \end{aligned} \tag{40}$$

where $\mathbf{D}$ is the vector of dispersion (D, D'), $\mathbf{M}$ is transport matrix [21].

$$\mathbf{R}_6(s|s_2) = -\mathbf{M}(s|s_2)\mathbf{D}(s), \tag{41}$$

Consider an arc consisting of N identical bending cells but with a different set of betatron phase advances. It can be done using different matching sections. $\mathbf{M_i}$ is a transport matrix of one bending cell with phase advance μ_i.

$$\begin{aligned} \mathbf{J} &= \begin{pmatrix} \alpha & \beta \\ -\gamma & -\alpha \end{pmatrix}, \\ \mathbf{M_i} &= \mathbf{I}\cos\mu_i + \mathbf{J}\sin\mu_i = e^{\mathbf{J}\mu_i}. \end{aligned} \tag{42}$$

Transport matrix of a few bending cells from j^{th} cell to N^{th} cell is following:

$$\mathbf{M}_{j\to N} = \prod_{n=j}^{N}\mathbf{M_n} = \prod_{n=j}^{N} e^{\mathbf{J}\mu_n} = \exp\left(\mathbf{J}\sum_{n=j}^{N}\mu_n\right) \tag{43}$$

The deflection of the electron due to the CSR in N bending cells is following:

$$\begin{aligned} &\delta\mathbf{X} = -\int_{s_1}^{s_2}\mathbf{M}(s|s_2)\mathbf{D}(s)\frac{dE}{E_0 ds}ds = -\sum_{j=1}^{N}\int_{s_1}^{s_2}\mathbf{M}_{j\to N}\mathbf{M}(s|s_2)\mathbf{D}(s)\frac{dE}{E_0 ds}ds = \\ &= -\sum_{j=1}^{N}\int_{s_1}^{s_2}\exp\left(\mathbf{J}\sum_{n=j}^{N}\mu_n\right)\mathbf{M}(s|s_2)\mathbf{D}(s)\frac{dE}{E_0 ds}ds = -\int_{s_1}^{s_2}\mathbf{M}(s|s_2)\mathbf{D}(s)ds\frac{dE}{E_0 ds}\cdot\sum_{j=1}^{N}\exp\left(\mathbf{J}\sum_{n=j}^{N}\mu_n\right). \end{aligned} \tag{44}$$

The electron shift $\delta\mathbf{X}$ and emittance growth is minimal if:

$$\sum_{j=1}^{N} \exp\left(\mathbf{J} \sum_{n=j}^{N} \mu_n \right) = 0 \cdot \tag{45}$$

In equation (45) we can change matrix $\boldsymbol{J}$ to imaginary unit i (due to $\boldsymbol{J}^2$=-$\boldsymbol{I}$).

$$\sum_{j=1}^{N} \exp\left(i \sum_{n=j}^{N} \mu_n \right) = 0 \cdot \tag{46}$$

Obvious solutions of (15) is

$$\mu_n = 2\pi \frac{k}{N}, \tag{47}$$

where k is any integer [14].

Let's discuss limitations of this method. This effect is related to a CSR induced longitudinal motion δct. The longitudinal dynamics in the bending cells are alike if CSR induced longitudinal motion is much smaller then rms bunch length.

$$\delta ct << \sigma_z, \tag{48}$$

$$\delta ct = \int_{s_1}^{s_2} \mathrm{R}_{56}(s|s_2) \frac{dE}{E_0 ds} ds < \frac{\Delta E_{csr}}{E_0} R_{56} = \delta_{csr} R_{56}, \tag{49}$$

where R_{56} is the longitudinal dispersion in the bending section, δ_{csr} is CSR induced relative energy spread produced in the bending section. Condition (48) is valid if δ_{csr} is small enough.

$$\delta_{csr} << \frac{\sigma_z}{R_{56}} \cdot \tag{50}$$

5.2.4 Numerical modeling

Let's construct a 30° bending section based on the introduced conception. Let's the bending radius R=15 m. The L_t equal 2 mm in this case and the 1D CSR model is valid. Let's construct 30° bending section as four 7.5° bending cells. We consider each cell to be a double bend achromat (DBA) with an anti-magnet in the middle to make the cell isochronous. The bending angle of the two main magnets is 4.05° and of the anti-magnet is -0.6°. Between the magnet and the anti-magnet there are 2 quads. Matching of the DBAs is made by 3 quads. Betatron phase advance in the cell is μ_x=3/4·2π, μ_y≈0.335·2π

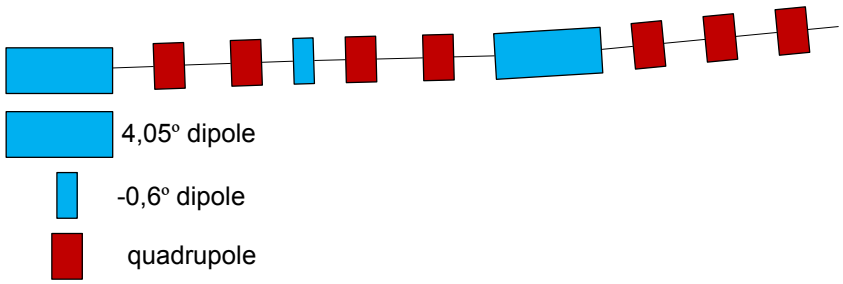

Figure 11. Scheme of a cell.

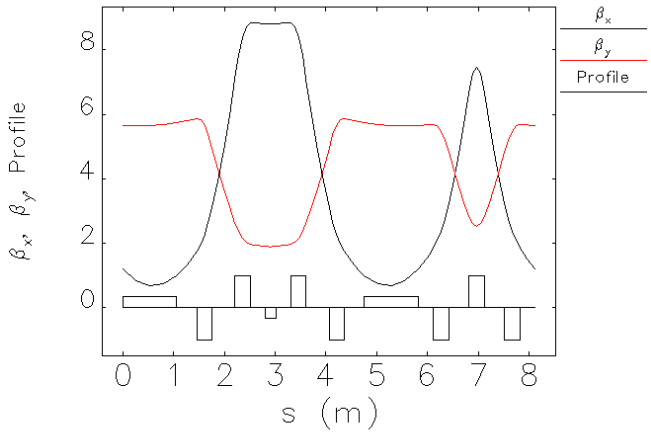

Figure 12. β functions in a cell.

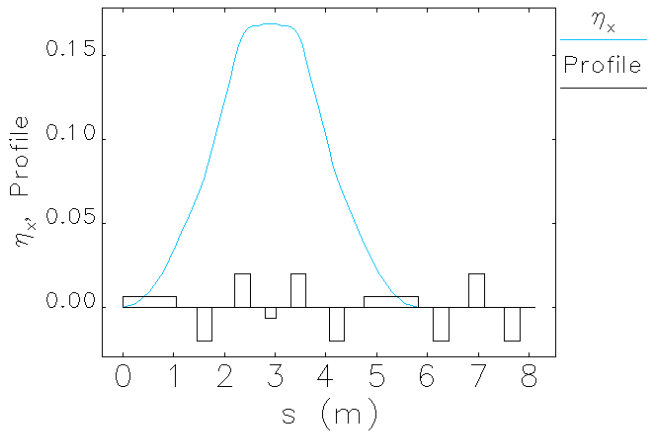

Figure 13. η function in a cell.

The 30° bending section with a 4 quad input and output matching sections is shown in Figure 14, Figure 15 and Figure 16:

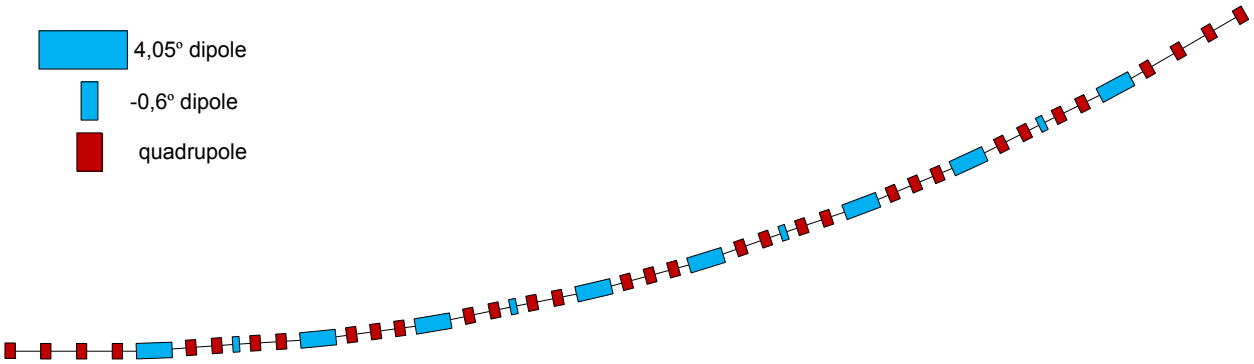

Figure 14. Scheme of the 30° bending section.

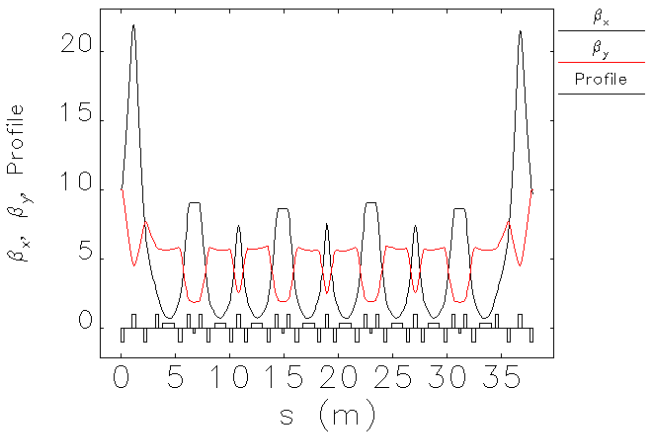

Figure 15. β functions in the 30° bending section.

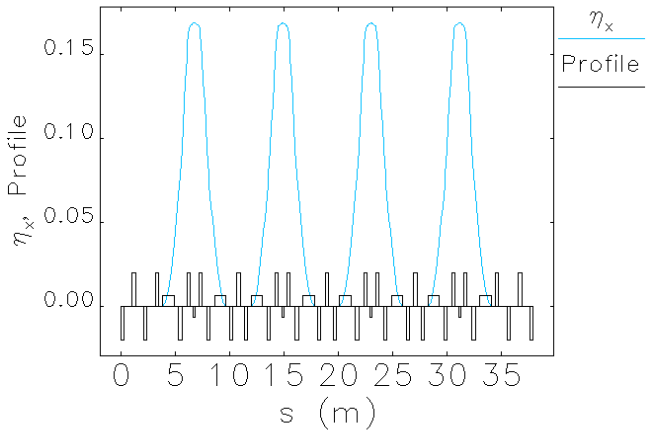

Figure 16. η function the 30° bending section.

Let's make a numerical test of such optics. Consider a bunch with σ_z=3 μm, charge Q=15.4 pC, normalized emittance ε_n=0.1 mm·mrad, energy E=6 GeV and relative energy spread δ_{rms}=10^{-4}. Let's estimate the relative energy spread produced in one cell [16].

$$\delta_{csr} \approx \frac{\sqrt{2}}{\sqrt{\pi}\sqrt[3]{3}} \frac{eQR^{1/3}\varphi}{E_0 4\pi\varepsilon_0 \sigma_z^{4/3}} \approx 10^{-4}. \quad (51)$$

The maximal longitudinal dispersion in the cell is $(R_{56})_{max}$≈1 mm and conditions of identity of longitudinal motion in the cells (51) is satisfied.

$$\delta_{csr} = 10^{-4} << \frac{\sigma_z}{(R_{56})_{\max}} = \frac{3\mu m}{1mm} \approx 3 \cdot 10^{-3}. \quad (52)$$

The modelling of the bunch motion through the bend was done by CSRtrack [22]. 3·10^5 sub-bunches with a radius 0.01 μm were used for the simulation with self-forces model 'projected' and 2·10^4 sub-bunches with a radius 0.1 μm were used for the simulation with self-forces model 'csr_g_to_p'. All simulations give the same results.

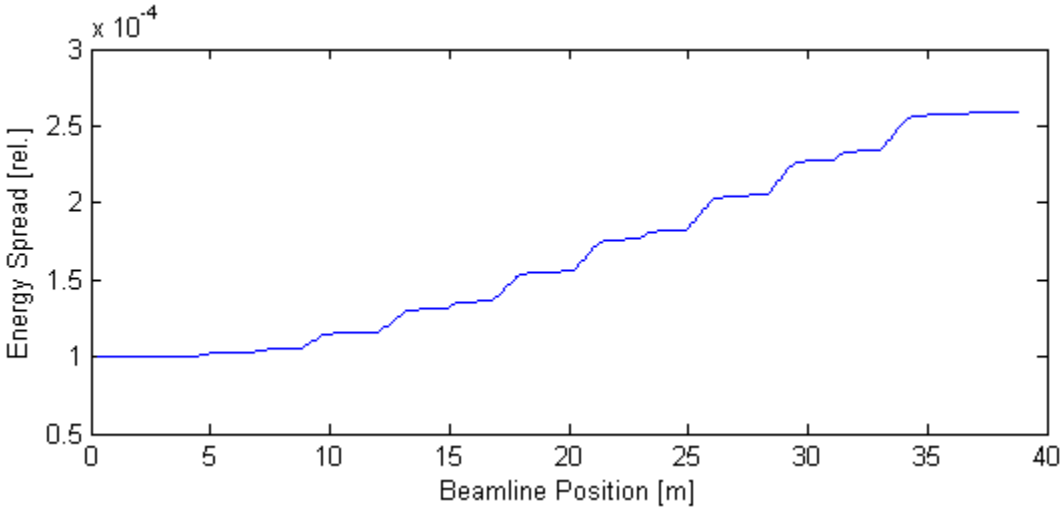

Figure 17. Relative energy spread along the bending section for test bunch.

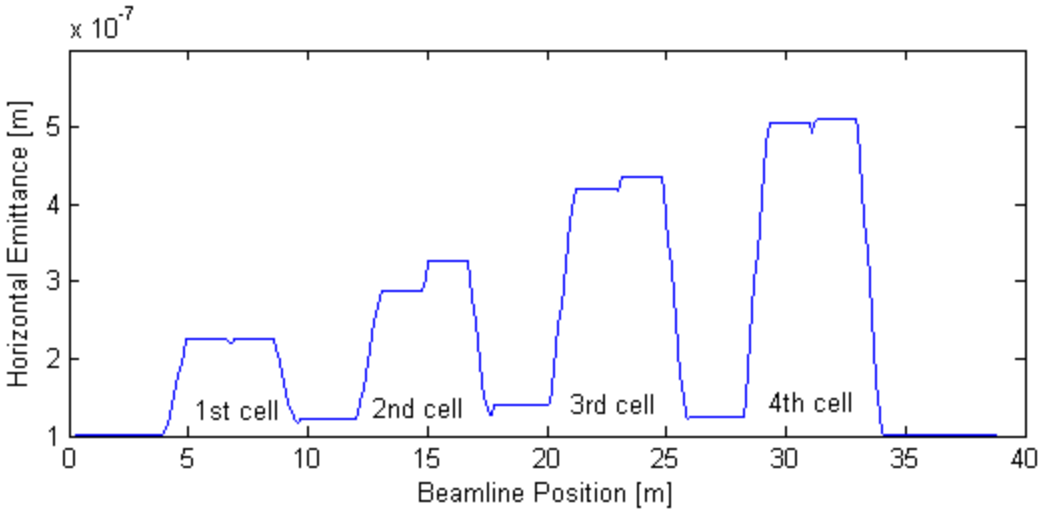

Figure 18. Normalised transversal emittance along the bending section for test bunch.

As you can see from the Figure 17, bunch radiates intensely. Figure 18 shows that transversal emittance is growing. The emittance growth inside each cell is due to dispersion. The emittance behind each cell is due to CSR induced slice shift. The emittance dilution cancels at the end of the bending section.

5.2.5 Incoherent SR

Let's estimate increase of normalize emittance due to incoherent SR in one turn.

$$\Delta\varepsilon_{ISR} = \frac{55 r_e \hbar c}{48\sqrt{3} mc^2}\gamma^6 I_5,$$
$$I_5 = \oint \frac{\gamma D^2 + 2\alpha DD' + \beta D'^2}{|R|^3} ds. \quad (53)$$

where I_5 is 5th radiation integral for a bending cell. As a rough estimate following can be used:

$$\Delta\varepsilon_{ISR} \approx \frac{r_e \hbar c}{mc^2}\gamma^6 \frac{\theta^3}{R} \approx 10^{-27} m^2 \cdot \gamma^6 \frac{\theta^3}{R} \quad (54)$$

where θ is bending angle. The increase of normalized emittance at one turn at 6 GeV is:

$$I_5 = \frac{360^\circ}{7.5^\circ} \cdot 7 \cdot 10^{-7} m^{-1} \approx 3 \cdot 10^{-5} m^{-1},$$
$$\Delta\varepsilon_{ISR} = \frac{55 \cdot 2.817 \cdot 10^{-15} m \cdot 197.3 \cdot 10^{-15} MeVm}{48\sqrt{3} \cdot 0.511 MeV}\left(\frac{6000 MeV}{0.511 MeV}\right)^6 3 \cdot 10^{-5} m^{-1} \approx 0.05 mm \cdot mrad \quad (55)$$

Let´s estimate increase of normalized emittance due to incoherent SR in an undulator at the middle of 6 GeV loop. I_5 in an undulator is:

$$I_5 = N\frac{8}{15}\frac{\beta_x 4\pi^2}{\lambda_p^2}\left(\frac{K}{\gamma}\right)^5, \tag{56}$$

$$I_5 = 5\sum_{i=1}^{6} N\frac{8}{15}\frac{\beta_x 4\pi^2}{\lambda_p^2}\left(\frac{K}{E_i/mc^2}\right)^5 = 5\sum_{i=1}^{6} 10^3\frac{8}{15}\frac{10m\cdot 4\pi^2}{(0.04m)^2}\left(\frac{2}{i\cdot 10^3 MeV/0.511MeV}\right)^5 \approx 2.4\cdot 10^{-7} m^{-1}. \tag{57}$$

So impacts from undulators are much smaller than from bending magnets.

Short bunch mode is one of the aims of FSF project. Let's estimate the bunch lengthening due to SR effect [23]. The growth of the bunch length in case of the mirror symmetric isochronous magnetic optic $R_{56}(s, L) = - R_{56}(0, s)$ is following.

$$\Delta\sigma^2 = \frac{55}{24\sqrt{3}}\frac{r_0^2}{\alpha}\gamma^5\int_0^L R_{56}^2(0,s)\cdot\frac{ds}{R^3} \tag{58}$$

Where γ is the relativistic factor, r_0 is the classical electron radius and α=1/137 is the fine structure constant. For an isomagnetic ring consisting of triple bend achromat arcs one can estimate the bunch length growth per turn as:

$$\begin{aligned}\Delta t &\approx \frac{1}{c}\sqrt{\frac{55}{24\sqrt{3}}\frac{r_0^2}{\alpha}\frac{\gamma^5}{126}\left(\frac{L_m}{R}\right)^7\frac{\pi R}{L_m}} \approx \\ &\approx \frac{1}{3\cdot 10^8 ms^{-1}}\sqrt{\frac{55}{24\sqrt{3}}\frac{(2.817\cdot 10^{-15}m)^2}{1/137}\frac{11742^5}{126}\left(\frac{1m}{15m}\right)^7\frac{\pi 15m}{1m}} \approx 0.1 fs.\end{aligned} \tag{59}$$

It is then essential to limit this growth factor as here it is analytically approximated to be more than 1% of the specified total bunch length.

The energy loss due to ISR in bending magnets:

$$P_\gamma = \frac{cC_\gamma}{2\pi}\frac{E^4}{R^2}, \quad C_\gamma = \frac{4\pi}{3}\frac{r_e}{(mc^2)^3} = 8.846\cdot 10^{-5}\frac{m}{GeV^3} \tag{60}$$

where P_γ is the ISR power:

$$\Delta E = \int P_\gamma\frac{ds}{c} = \int\frac{cC_\gamma}{2\pi}\frac{E^4}{R^2}\frac{ds}{c} = \int\frac{C_\gamma}{2\pi}\frac{E^4}{R^2}ds \tag{61}$$

Let's estimate the energy loss due to ISR in bending magnets at the middle of 6 GeV loop.

$$\Delta E = \int\frac{C_\gamma}{2\pi}\frac{E^4}{R^2}ds = \sum_{i=1}^{6}\frac{C_\gamma}{2}\frac{E_i^4}{R} = \sum_{i=1}^{6}\frac{C_\gamma}{2}\frac{E_i^4}{R} = \sum_{i=1}^{6}\frac{8.846\cdot 10^{-5}\frac{m}{GeV^3}}{2}\frac{(i\cdot GeV)^4}{15m} = 6.7MeV \tag{62}$$

The energy loss due to ISR in undulator:

$$\Delta E = \frac{1}{3} r_e mc^2 \gamma^2 K^2 \left(\frac{2\pi}{d}\right)^2 Nd \tag{63}$$

Let's estimate the energy loss due to ISR in undulators at the middle of 6 GeV loop.

$$\begin{aligned} &\Delta E = 5\sum_{i=1}^{6} \frac{1}{3} r_e mc^2 \left(\frac{E_i}{mc^2}\right)^2 K^2 \left(\frac{2\pi}{d}\right)^2 Nd = \\ &= 5\sum_{i=1}^{6} \frac{1}{3} 2.8\cdot 10^{-15} m \cdot 0.511 MeV \left(\frac{i\cdot 10^3}{0.511 MeV}\right)^2 2^2 \left(\frac{2\pi}{0.04m}\right)^2 10^3 \cdot 0.04m = 3.3 MeV \end{aligned} \tag{64}$$

So the energy loss due to ISR in undulators and bends at the middle of 6 GeV loop is 10 MeV.

Let's estimate the energy spread due to ISR in bending magnets

$$(\Delta E)^2 = \int \frac{55}{24\sqrt{3}} P_\gamma \varepsilon_c \frac{ds}{c} \tag{65}$$

where ε_c the critical photon energy.

$$\varepsilon_c = \frac{3}{2} \frac{\hbar c \gamma^3}{R}, \tag{66}$$

At 6GeV loop it is:

$$\varepsilon_c[keV] = 2.218 \cdot \frac{E[GeV]^3}{\rho[m]} = 2.218 \cdot \frac{(6GeV)^3}{15m} = 32keV, \tag{67}$$

Hence

$$\begin{aligned} &(\Delta E)^2 = \int \frac{55}{24\sqrt{3}} \cdot \frac{cC_\gamma}{2\pi} \frac{E^4}{R^2} \cdot \frac{3}{2} \frac{\hbar c \gamma^3}{R} \cdot \frac{ds}{c} = \\ &= \int \frac{55}{24\sqrt{3}} \cdot \frac{3}{4\pi} C_\gamma \frac{(mc^2)^4 \gamma^4}{R^2} \cdot \frac{\hbar c \gamma^3}{R} \cdot ds = \int \frac{55}{24\sqrt{3}} \cdot \frac{r_e mc^2 \gamma^7}{R^3} \cdot \hbar c \cdot ds = \\ &= \frac{55}{24\sqrt{3}} \alpha (\hbar c)^2 \int \frac{\gamma^7}{R^3} ds. \end{aligned} \tag{68}$$

Let's estimate the energy spread due to ISR in bending magnets at the middle of 6 GeV loop.

$$(\Delta E)^2 = \frac{55}{24\sqrt{3}}\alpha(\hbar c)^2\int\frac{\gamma^7}{R^3}ds = \frac{55}{24\sqrt{3}}\alpha(\hbar c)^2\sum_{i=1}^{6}\left(\frac{E_i}{mc^2}\right)^7\frac{\pi}{R^2} =$$
$$= \frac{55}{24\sqrt{3}}\frac{1}{137}(6.58\cdot10^{-22}\,MeVs\cdot3\cdot10^8\,ms^{-1})^2\sum_{i=1}^{6}\left(\frac{i\cdot10^3\,MeV}{0.511MeV}\right)^7\frac{\pi}{(15m)^2}\approx0.22MeV^2, \quad (69)$$
$$\Delta E = 0.47MeV.$$

Let's estimate the energy spread due to ISR in undulator:

$$(\delta\gamma)^2 = \frac{7}{15}\frac{\hbar}{mc}r_e\gamma^4\left(\frac{2\pi}{d}\right)^3K^2\left(1.2K+\frac{1}{1+1.33K+0.4K^2}\right)Nd \quad (70)$$

And the energy spread due to ISR in undulators at the middle of 6 GeV loop is following

$$(\delta\gamma)^2 = 5\sum_{i=1}^{6}\frac{7}{15}\frac{\hbar}{mc}r_e\left(\frac{E_i}{mc^2}\right)^4\left(\frac{2\pi}{d}\right)^3K^2\left(1.2K+\frac{1}{1+1.33K+0.4K^2}\right)Nd =$$
$$= 5\sum_{i=1}^{6}\frac{7}{15}3.86\cdot10^{-13}m\cdot2.8\cdot10^{-15}m\left(\frac{i\cdot10^3MeV}{0.511MeV}\right)^4\left(\frac{2\pi}{0.04m}\right)^3 2^2\left(1.2\cdot2+\frac{1}{1+1.33\cdot2+0.4\cdot2^2}\right)10^3\cdot0.04m = \quad (71)$$
$$= 0.1337$$
$$(\Delta E)^2 = (\delta\gamma)^2\cdot(mc^2)^2 = 0.036MeV^2$$
$$\Delta E = 0.19MeV$$

The growth of energy spread $\Delta E\approx0.5$MeV is comparable to the present machine technology specification for the relative energy spread $\Delta E/E\approx10^{-4}$.

5.3 Arcs

Each arc consists of 30° bending sections. Between them undulator sections are installed. In each 180° arc we have 6 bending section and 5 undulator sections.

Arcs at 1 GeV and 2 GeV are designed with adjustable R_{56} to compress the bunch. We call them 'low energy' arcs. 3 GeV, 4 GeV, 5 GeV and 6 GeV arcs are designed with a fixed R_{56}=0 and are optimized for minimal I_5. We call them 'high energy arcs'. Suppression of CSR induced transversal emittance growth is envisaged at each arc. This is achieved by adjusting phase of the betatron oscillations between the arc sections.

The 'low energy' bending section is a triple bent achromat (TBA). It consists of three 10° bends. Between the outer magnets and the middle magnet there are 3 quads. The magnets length of dipole magnets is L=1.16 m, the bending radius R=6.7 m, bending magnetic field for 2 GeV beam equal 1.0 T. 5 quadrupoles after TBA adjust latice functions and x betatron phase advance.

The ‘high energy’ bending section is described in the Ch.5.2.4. Twiss parameters and dispersion in a section of the arc is shown in Figure 19.

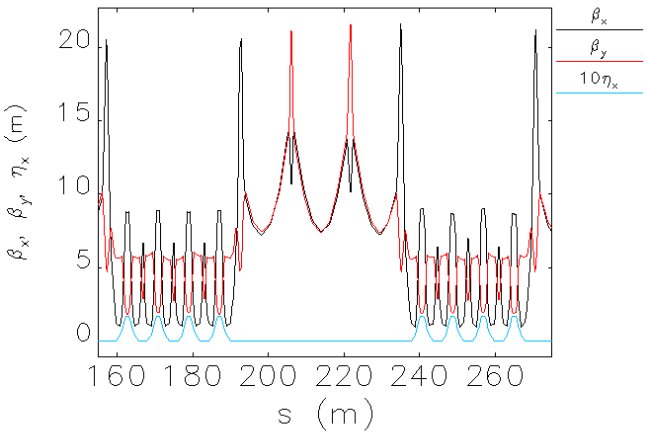

Figure 19. Twiss parameters and dispersion in a beamline with one undulator, two nearby bending sections and matching sections between them.

5.4 Beam Break Up instability in linear accelerators

In the superconducting cavities the electromagnetic field can be expressed as a sum of transverse magnetic (TM) and transverse electric (TE) modes. For TM modes there is a longitudinal electric field present and a magnetic field could be everywhere perpendicular to the longitudinal axis. For TE modes the situation is opposite with a longitudinal magnetic field and electrical field transverse to it everywhere. When a charge passes through a cavity it excites modes and induces fields which provide a retarding force. Some of the modes could be excited quite strong and lead to beam instabilities and finally to a beam loss. One of such instabilities due to dipole modes – Beam Break Up (BBU) instability – will be discussed later. There are different types of BBU instability – single bunch, which caused by short-range wake fields and two types of multi-bunch instabilities caused by long-range wakefields – cumulative and regenerative.

Some modes (e.g. quadrupole modes) might lead to beam emittance degradation. This means the loss of luminosity for colliders or, what is more important for ERL-based light sources, the brightness loss. On the other hand the excited modes give addition power dissipation in the cavity walls and increase the cryogenic losses.

Estimations show that the single bunch BBU is not relevant [24] for the stability of the beam at FSF.

A cumulative BBU occurs when there is no electromagnetic coupling between cavities but the dipole mode is excited in each cavity of the linac. The bunch is deflected in the first cavities by a dipole mode and excites the later cavities due to the off-axis position of the beam in the following cavities. The deflection grows with each cavity. Cumulative BBU is important for the facilities with a long linac.

A regenerative BBU appears in a linac when there is a strong electromagnetic coupling between the accelerating cavities. In this case the deflecting mode is “distributed” mode in a multicell structure and, when it’s phase velocity is the same as that of the beam (~c), the beam gets unstable. The excitation of the mode by the beam is carried electromagnetically from one cell to the next in the linac structure. The bunch is deflected in the first cavities and then it excites the later cavities or it excites the same cavity after recirculation so that the deviation is carried by the beam. This excitation grows with each bunch and, if the energy transfer to the cavity is greater than the ohmic losses of the cavity, then the instability develops.

This type of BBU instability can limit the beam current in energy recovery linacs. This type of instability is discussed in this chapter.

5.4.1 Beam Break Up instability in ERLs

One potential weakness of the ERLs is a regenerative form of BBU – transverse beam breakup instability, which may severely limit a beam current. The actuality of this problem was recognized in early experiments with the recirculating SRF accelerators at Stanford [25] and Illinois [26], where threshold current of this instability was measured to be few microamperes. In the works of Rand and Smith in [27] dipole high order modes were identified as a driver of this instability. In late of the 80’s the detailed

theoretical model and simulation programs had been developed [28, 29]. Nowadays the interest to this problem was renewed. The requirements for more detailed theory and simulation programs [30-33] are given by the needs of high current (~100 mA) ERLs.

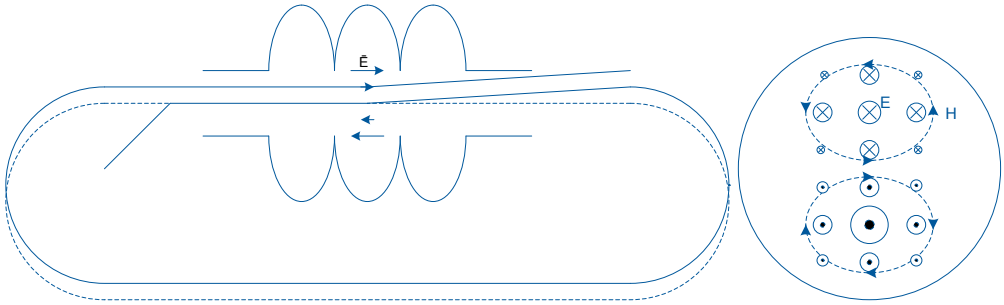

Figure 20. Mechanism of BBU instability. On the left side schematically presented a layout of an ERL and trajectory kick due to a dipole mode. On the right side the fields in the transversal plane in this mode are presented

First let us briefly explain the fundamentals of the BBU instability. If an electron bunch passes through an accelerating cavity it interacts with dipole modes (e.g. TM_{110}) in the cavity (Figure 20). First, it exchanges energy with the mode; second, it is deflected by the magnetic field of the mode. After recirculation the deflected bunch interacts with the same mode in the cavity again and transfers energy. If the net energy transfer from the beam to the mode is larger than the energy loss due to the mode damping the beam becomes unstable.

We start with a simple model of a single pass machine with one cavity with one dipole mode. We also neglect the length of the cavity and assume that the mode give a point like kick. We can assume that our bunch is one particle with the charge q. So, at the first pass we have:

$$\begin{cases} x_1 = 0 \\ x_1' = -\dfrac{eV_a}{\omega a p}\sin(\varphi)' \end{cases} \quad (72)$$

where x_1 is the coordinate (we assume beam on the axis on the 1-st pass and, therefore, there is no energy change) and x_1' is the kick angle, φ is the phase and p is the momentum of the bunch. After the pass through a recirculating ring with a transfer matrix M = $(m)_{ij}$, the bunch will come with an offset.

$$x_2 = m_{12}x_1'. \quad (73)$$

The energy deposited by the bunch in the mode can be written as:

$$\Delta U_2 = -q\frac{V_a}{a}\cos(\varphi + \omega T_r)m_{12}x_1'. \quad (74)$$

Ohmic losses in the cavity can be expressed as:

$$P_c = \frac{V_a^2}{\left(\frac{\omega}{c}\right)^2 a^2 \left(\frac{R}{Q}\right)_d Q}. \quad (75)$$

The threshold value is reached, when the ohmic losses and the average power deposited by individual bunch are equal:

$$< \Delta U_2 > f_b - P_c = 0. \quad (76)$$

The averaging over the phase of the mode φ is done. This is possible due to assumption that the bunches are coming with the frequency of the main acceleration mode, which is not a multiple to the frequency of the dipole mode. Therefore, the phase of the dipole mode at the beam passes is a random value uniformly distributed at [0; 2π]. The frequency f_b at the threshold current is given by:

$$f_b = I_{th} / q. \quad (77)$$

And now (76) leads to the final equation for the threshold current:

$$I_{th} = -\frac{2pc^2}{e\omega \left(\frac{R}{Q}\right)_d Q m_{12} \sin(\omega T_r)}. \quad (78)$$

From (78) one can see that the threshold current is proportional to the beams energy. It means that the most problematic cavities are where a beam has a lower energy. The threshold current is inversely proportional to:

- the impedance and the quality factor of the mode which should be minimized on a cavity design stage;
- the m_{12} matrix element, which for the case of a single mode and one cavity can be written as $\sqrt{\beta_1 \beta_2} \sin \mu$, where $\beta_{1,2}$ – is a Twiss parameter of a beam on the 1st and 2nd passes correspondingly, should be minimized to achieve the highest threshold current. The betatrone phase advance μ is additional optimization parameter.

It is required to know the phase of the mode φ, when the HOM frequency is equal to a harmonic number of the bunch repetition rate ($M/N \cdot f_b$, with integer M, N). In this resonant case the presented model does not provide the right solution. One has to calculate the phase using some other method or some simulation program. It should be noted that the resonance cases should be avoided on the design stage by a proper choice of the beam frequency and of the cavity parameters. Also, (78) is true only for the case when the term $m_{12} \sin(\omega T_r) < 0$. This case perfectly agrees with simulation results as it was presented in [35]. Eq. (78) gives beams stability for the opposite case, when $m_{12} \sin(\omega T_r) > 0$, but the simulation results show that the beam can be unstable with a high threshold current. This discrepancy

caused by the assumption that the voltage induced by the beam on the second pass is very small compared to the HOM voltage, which fails at high bunch charges. In this case a more complicated theory is required. Such a theory was well described by G. Hoffstaetter and I. Bazarov in [30].

5.4.2 Beam Break Up in multi-turn ERLs

In the case of multiple recirculation turns and multiple HOMs in the cavities the solution can be found by the same approach as for a single mode and single recirculation case. One just has to introduce additional indexes for the numbering of the modes and of the recirculation turns. After that it should be carefully summarized and result will be found. The threshold current for the transverse beam breakup may be estimated for the case of a single cavity and single mode for a multipass ERL in the form [33]:

$$I_b \approx I_0 \frac{\lambda\!\!\!^{-2}}{QL_{eff}\sqrt{\sum_{m=1}^{2N-1}\sum_{n=m+1}^{2N}\frac{\beta_m\beta_n}{\gamma_m\gamma_n}}}, \qquad (79)$$

where I_0- Alfven current, Q is the quality factor of HOM, $\lambda\!\!\!^{-} = \lambda/2\pi$, λ is the wavelength corresponding to the resonant frequency of the TM_{110} mode, γ_m is the relativistic factor at the m^{th} pass through the cavity, β_m – is the Twiss parameter, L_{eff} – is the effective length of the cavity, N is the number of passes during acceleration. This expression indicates the limitation for the number of passes. It should be noted in [30] it was shown that the BBU threshold current for an N-turn ERL might be roughly estimated as $N(2N-1)$ times smaller as that in a single turn machine, when (79) gives only square root of this value and it is more realistic estimation.

Eq. (79) also shows that it is preferable to have low β-functions at low energies. Therefore, the optics in the Linac should be optimised to minimize beta functions of the beam to increase the threshold current of BBU instability on one hand and to decrease the beats of the beta functions in the spreaders on the other hand.

5.4.3 Modes overlapping

In this paragraph we discuss the overlapping of the modes in different cavities. If the difference between frequencies of two modes in any pair of cavities is smaller than the width of the mode $\Delta f = f/Q$, then the HOMs of these cavities start to interact with each other and the threshold current decreases. To show this we proceed with a modelling in GBBU program [34].

Firstly, we set the FSF optic in GBBU. For simplicity we assume that betatrone phase advances in all arcs between the linacs are the multiple of 2π and the transfer matrix, therefore, is given by:

$$M_k = \begin{pmatrix} \sqrt{\frac{\beta_{f,k}}{\beta_{i,k}}} & 0 \\ \frac{(\alpha_{i,k}-\alpha_{f,k})}{\sqrt{\beta_{f,k}\beta_{i,k}}} & \sqrt{\frac{\beta_{i,k}}{\beta_{f,k}}} \end{pmatrix}, \qquad (80)$$

where $(\alpha, \beta)_{i,f}$ – are the twiss parameters of the beam and k – is the number of the arc. Optic in the linacs is discussed in Ch.5.5.

Secondly, we set the HOMs of the cavities. We assume only one basic mode in a cavity with parameters: $(R/Q)_d$ = 60 Ω, $Q = 10^4$, f_0 = 2·GHz. During production of the cavities the frequency of the mode can differ from cavity to cavity due to fabrication accuracy. This difference df_i can be simulated using a Gaussian distribution – $\Phi_{0,\sigma}{}^2$ and i = 1,...,160 – is the number of the cavity. Hundred sets of FSF cavities were generated twice with σ = 1 and 10 MHz. The results of the modeling are presented in Figure 21. The worst case (I_{th} ~ 12 mA), when all the frequencies are exactly the same, is marked by the red line. The maximum of the threshold current (~ 490 mA) in Figure 21 corresponds to the case when the frequencies were ordered with a step of 1 MHz to avoid overlapping. Finally, the FSF specification current of 20 mA is marked with green.

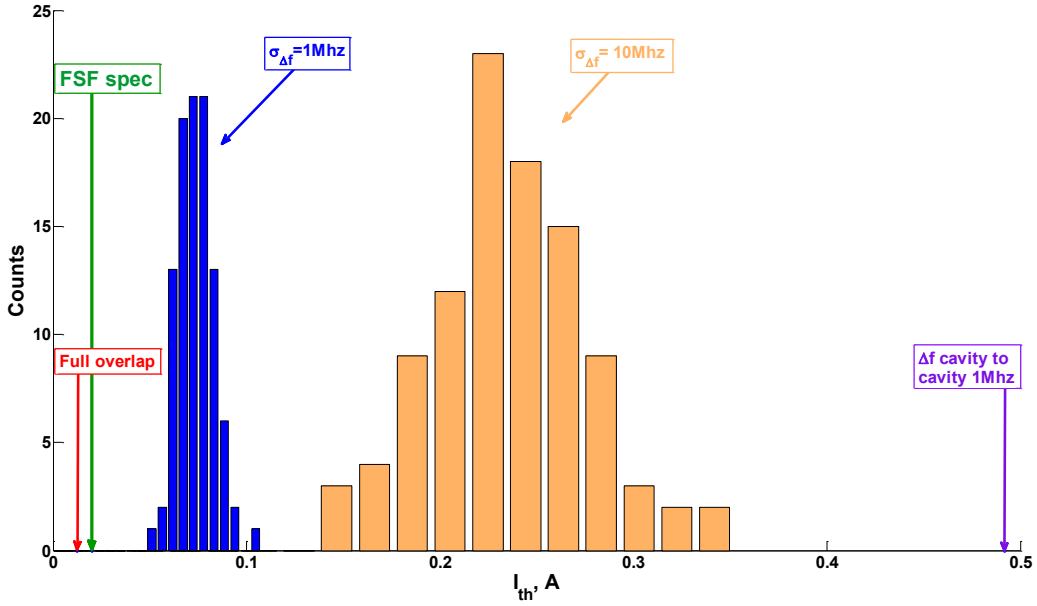

Figure 21. Results of BBU modeling for FSF with only one mode in each cavity.

5.5 Linacs optic design

In this chapter we discuss optic design of the linacs. The scheme of FSF is presented in Figure 2. The reasons why this injection-recirculation scheme was chosen are presented in 12 Appendix E.

In this scheme the energy gain in the preinjector and in two main linacs is chosen as follows: the final energy of a beam $E_{fin} = (E_0+E_{preinj})(1+2Nk) = 6$ GeV, where $E_0 = 10$ MeV is the energy after booster, E_{preinj} is the energy gain in the preinjector, $N = 3$ is the number of passes during acceleration and constant $k = 4$. Therefore, one has $E_{preinj} = 230$ MeV and $E_{linac} = 960$ MeV.

One of the main requirements for the optic was BBU instability. So the optic was calculated in order to achieve the maximum threshold current of BBU. The linacs are planned to be based on the B*ERL*inPro 7-

cell cavities. These cavities are optimized to have the lowest $(R/Q)_d \cdot Q_d$ parameter, therefore one has to minimize the beta functions in the linacs in order to achieve the highest threshold current. It was proposed to have 8 cavities in the cryomodule. The cryomodule is schematically presented in Figure 22, where λ=0.2306 m is the wavelength of the accelerating mode.

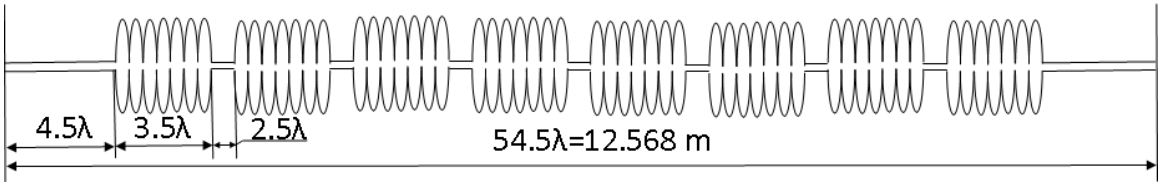

Figure 22. The scheme of the cryomodule.

5.5.1 Optic in the preinjection linac

For the preinjection linac we suggest to use two cryomodules with matching quadrupole magnets in between. The initial Twiss parameters (β_0 and α_0) to the first cryomodule are fixed by the design of the injector. In this paragraph we present the way how to match the beam after the first cryomodule to achieve the highest threshold current of BBU instability. We assume that the highest threshold current can be achieved when there are the same threshold currents for the entrance and for the middle of the linac. The solution can be used for both coordinates.

The initial beta function can be transferred through the 1st cryomodule as (see e.g. [36]):

$$\beta_1 = \frac{\gamma_1}{\gamma_0}\left(\beta_0 m_{11}^2 - 2\alpha_0 m_{11} m_{12} + \frac{1+\alpha_0^2}{\beta_0} m_{12}^2\right), \tag{81}$$

where m_{ij} is the transfer matrix of the 1st cryomodule, $\gamma_{0,1}$ – the Lorentz factors before and after the first cryomodule.

After the first cryomodule there are 4 quadrupole magnets which match the beam to the second cryomodule β_2 and α_2. So the beta function at the end of the linac can be found as:

$$\beta_f = \frac{\gamma_f}{\gamma_1}\left(\beta_2 t_{11}^2 - 2\alpha_2 t_{11} t_{12} + \frac{1+\alpha_2^2}{\beta_2} t_{12}^2\right), \tag{82}$$

where t_{ij} is the transfer matrix of the 2nd cryomodule and γ_f is the Lorentz factor at the end of the linac.

The minimum of the β_f is reached, when

$$\frac{\partial \beta_f}{\partial \alpha_2} = 0 \Rightarrow \alpha_2 = \frac{t_{11}}{t_{12}}\beta_2 . \tag{83}$$

The threshold current is defined by the equation (79) for a multi-pass ERL with one cavity and one mode in it. We want to keep the same threshold currents for the first and last cavity of the cryomodule that gives:

$$\sqrt{\frac{\beta_0\beta_f}{\gamma_0\gamma_f}} = \sqrt{\frac{\beta_1\beta_2}{\gamma_1^2}}\,. \tag{84}$$

The solution is given by:

$$\beta_2^2 = \frac{\beta_0 t_{12}^2}{\beta_0 m_{11}^2 - 2\alpha_0 m_{11} m_{12}\dfrac{1+\alpha_0^2}{\beta_0} m_{12}^2}\,. \tag{85}$$

The matrices of the cryomodules can be found using e.g. Elegant program for SPM: m_{11}= -0.8084, m_{12}= 1.6788, t_{11}= 0.6056, t_{12}= 7.2694. And finally the initial parameters to the second cryomodule are: α_{2x} = 1.1768, β_{2x}= 14.13 m and α_{2y} = 1.1798, β_{2y}= 14.1667 m. Optic for this solution is presented in Figure 23.

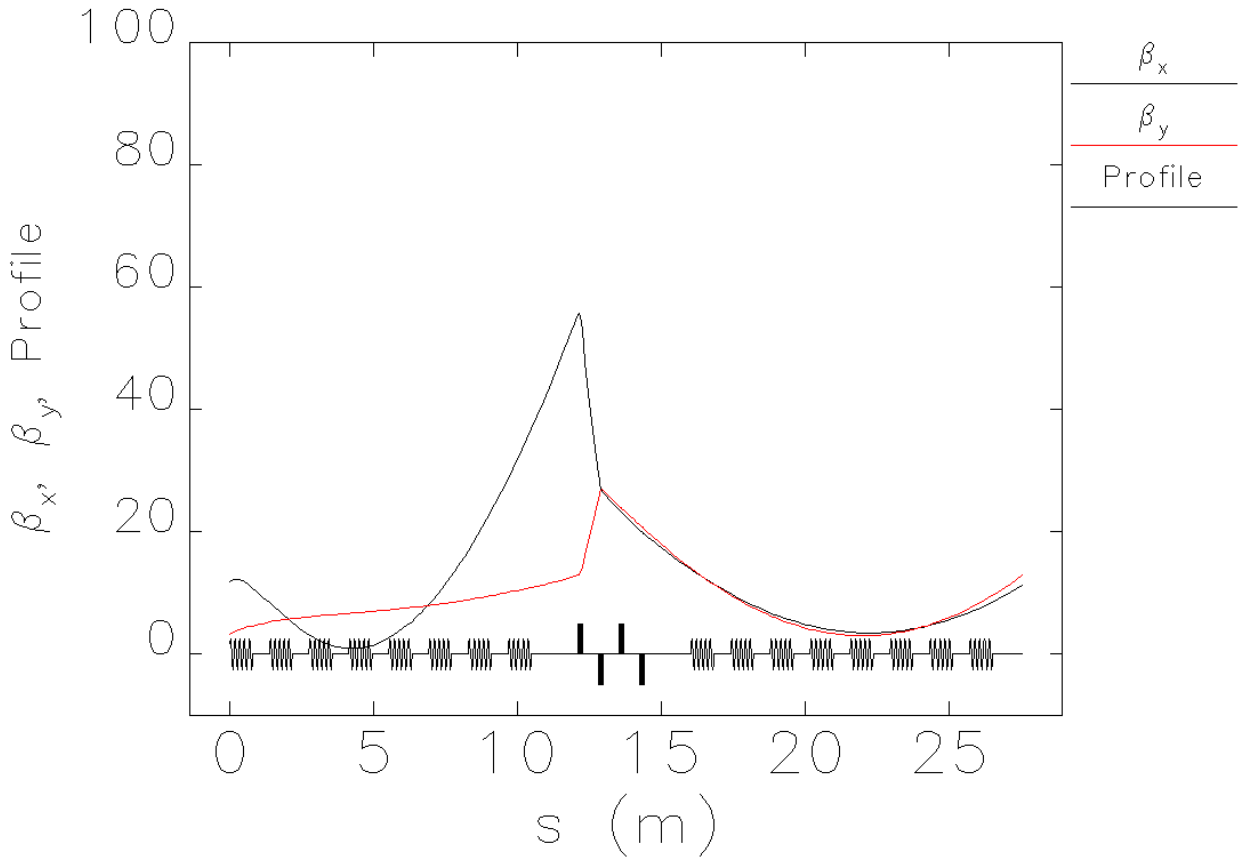

Figure 23. Optic in the FSF preinjector for SPM.

5.5.2 Optic in the main linacs

To reach 960 MeV in the main linac we took 9 cryomodules. Triplets of quadrupoles are planned to be in between the cryomodules in the linac. The full length of the linac is then about 140 m. The strengths of the quadrupoles were optimized to have the minimum of the beta functions on the 1st pass. The initial Twiss parameters for the 2nd and 3rd passes were found in order to minimize the maximum of the β-function. Optic for the 3 passes through the first and the second main linacs is presented in Figure 24, Figure 25. In both linacs quadrupoles are assumed to be located symmetrically at the middle of the 5th cryomodule, therefore optic on deceleration is given from right to left.

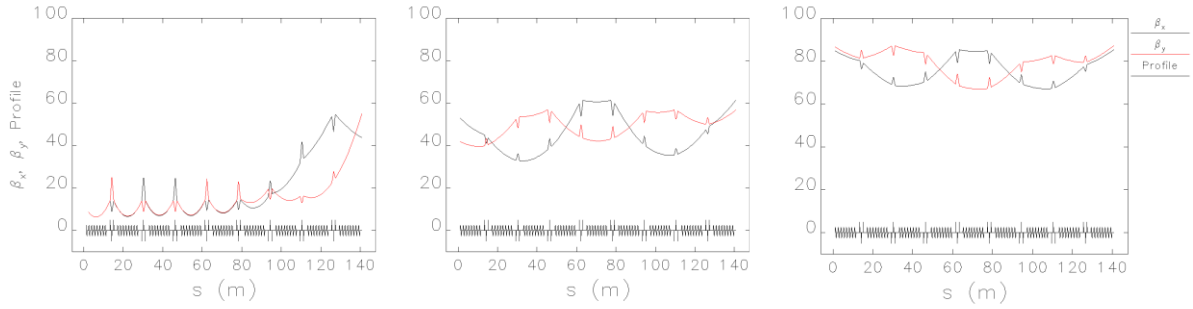

Figure 24. Optic design of the 1st 0.96 GeV linac of FSF. 3 passes on acceleration are presented from left to right.

The threshold currents can be estimated using:

$$I_{th} = \frac{2mc^3}{e\omega\left(\frac{R}{Q}\right)_d Q_d} \frac{1}{\sqrt{\sum_{m=1}^{5}\sum_{n=m+1}^{6}\frac{\beta_m\beta_n}{\gamma_m\gamma_n}}}, \quad (86)$$

which is a combination of Eqs. (78) and (79). For a mode with $(R/Q)_d \cdot Q = 6\cdot10^5$ Ω, $\omega = 2\pi\cdot2\cdot10^9$ Hz one could get for the beginning of the first linac I_{th} = 0.73 A and for the second I_{th} = 2.34 A, when for the preinjector it is about 0.48 A (for x-coordinate, middle of the linac). That means the instability develope in the preinjection linac.

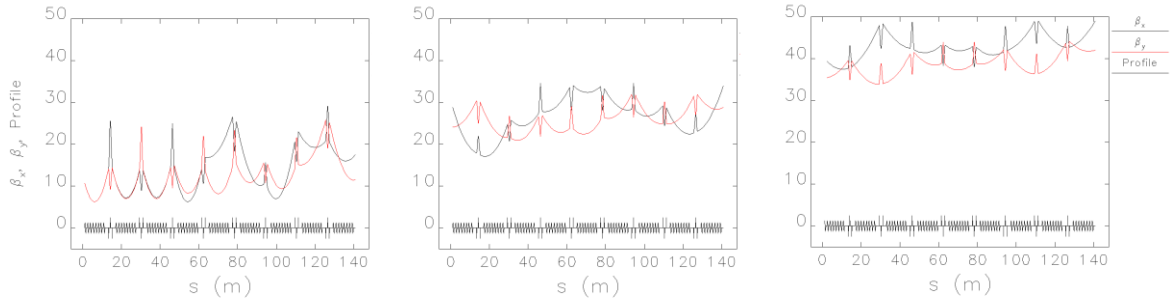

Figure 25. Optic design of the 2nd 0.96 GeV linac of FSF. 3 passes on acceleration are presented from left to right.

5.6 Spreaders/recombiners

In the multi-turn accelerator all energy beams pass through the linac. Linac's optics is fixed on a lowest energy bunch and it focuses high energy beams insufficiently. In our case, the size of 1 GeV linac is 140 meter. Therefore, the output linac β-functions reach 100 meters for 5 GeV and 6 GeV beams. But at that energy beamlines should also be optimized for minimum I_5. It is complicated optics spreaders/recombiners setting and make necessitates usage in spreader magnets with large bending radius that reduce I_5. Each spreaders beamline are achromatic and isochronous. Firstly, beams spread at vertical dipole. Then 4 GeV and 6 GeV beams spread horizontally by Lambertson septum like magnets. The distance between 4 GeV, 5 GeV and 6 GeV beams at entrance of septum magnet are 30 mm, 20 mm respectively. Thus 1 GeV, 2 GeV, 3 GeV and 5 GeV beamlines are vertically separated; 4 GeV and 6 GeV beamlines are 3-dimentional. A little coupling which appears there is decoupled by solenoids. Below is the schema of spreaders.

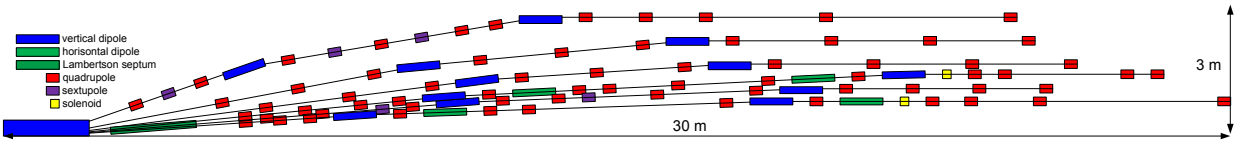

Figure 26. Schema of spreader

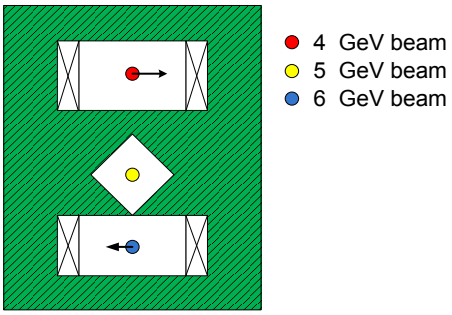

Figure 27. Scheme of horizontal separation by Lambertson septum like magnet.

Latice functions are presented in Appendix C: Latice functions in spreaders/recombiners

5.7 Start to end beam dynamics simulation

Setting the start-to-end simulations of the FSF shall prove the integrity of the optic concept and give a fealing of cumulative effect of the beam delution effects.

Unfortunately, there was no one single package available that would cover the needs of FSF optic modelling. Therefore, the low energy (<50 MeV) section (injector and a part of the injection linac of the 2nd injection stage) was modelled with ASTRA [8] as described in Ch.5.1. Space charge effects are strong in this part of the accelerator and their influence can only be neglected at the beam energies above several 10's of MeV. Afterwards, Elegant code [38] is used to calculate linear and non-linear beam dynamics, including collective effects (CSR in 1D approximation) as well as incoherent synchrotron radiation. Low energy section of the accelerator after beam deceleration was modelled further on with the Elegant code, since we are flexible with the values of the transverse beam emittance and the influence of the space charge effects on the beam size is negligible here. The 1D model was benchmarked for simple magnetic strutures using full 3D CSR tracking codes like CSRTrack [22] and gave completely satisfying results for FSF beam parameters in all operation modes.

Main results of the start-to-end simulations are presented in the following subchapters. First, high brilliance mode is considered. Afterwords, results for the short pulse mode are given.

5.7.1 High Brilliance Mode

A staged injection was incorporated into the FSF. The benefits of including an intermediate linac and staging the injection are comprehensively discussed in [24]. Simulations show that higher injection energy increases the Transversal Beam Break-Up (TBBU) threshold in the first split linac. Here a compromise between the injection and main linac energy was found for a two staged scheme.

The additional linac and arc are also useful for bunch compression. The combination of off-crest acceleration in the linac and the R_{56} in the arc compress the beam from 2 to 1 ps in both operation modes. Investigations described in Ch.5.7.2.4 show the extent of the compression at this stage are critical for the optimum beam parameters at high energy. Next generation light sources require CW linac operation to achieve high average currents. This sole desire has supported the development of SRF based injectors. Although higher peak field gradients are attainable using normal conducting technology the duty cycle remains low. Also, the lowest emittance in CW mode operation is achievable only with SRF based photo-injectors.

Figure 8 shows a schematic of the FSF injector. A booster module of three cavities is implemented directly after the SRF gun to combat the space charge forces acting on the bunch at low energy which are seen as the main limitations on the transversal emittance. The merger section shares a final bending magnet in the transferline chicane of the 2nd stage of the injection loop on route to the main 230 MeV injector linac. The first few cavities, not shown, of this linac are also used in the emittance optimization as space charge forces are still significant up to beam energies of 50 MeV. Hence the injection energy is referred here as 50 MeV rather than 10 MeV as quoted in Ch.5.1.1.

Table 5. Injection parameters from ASTRA simulations of the 15 pC HBM.

Pos	ε_{nx} (mm mrad)	ε_{ny} (mm mrad)	σ_z (mm)	E_b (MeV)
Gun	0.27	0.27	2.50	1.91
Booster	0.22	0.22	2.38	9.45
Merger	0.19	0.16	0.95	9.45
Injection Linac	0.13	0.09	0.93	53.41

Table 5 shows the beam parameters of the subtle transformation through the space charge dominated injection process to produce a low emittance beam in both transverse planes.

The start-to-end simulations leave ASTRA at this stage in the facility. The ASTRA beam distributions at 50 MeV for both modes are converted, matched and tracked onwards using Elegant. The space charge effects above 50 MeV are negligible so the remaining 8 km long optic of the FSF was simulated using Elegant to save on computational expense.

A possible scenario to make good use of the 100 m long transferline between the 230 MeV injector and arc is to envisage optic that may be used at a future date to aid the non-linear beam dynamics. For example, on the acceleration side, a series of laser heater undulators could be implemented and used to suppress the micro-bunching instability at the expense of the longitudinal emittance. Such a scheme could be based on [39] where a TiSa laser is used to overlap and interact with the electron beam. At this relatively low energy stage with $\gamma=480$, one could consider a laser of wavelength $\lambda=800$ nm and routine undulator parameters to develop this interaction.

The following section describes the beam parameters of the HBM. Both HBM and SPM operation share the same magnetic elements. The two modes should be compatible and share the same optic where possible. Elegant was used for the start-to-end tracking simulations. Elegant is capable of tracking particles through large complex lattice structures that incorporate all the relevant elements needed for acceleration and beam transport. For the simulations, all radiations effects are present [40] and 100 000 particles are tracked unless otherwise stated.

The schematic of the FSF presented in the machine design and philosophy section earlier is depicted again in Figure 28 as a blueprint for the simulations. The arcs are aligned so that they would fit in a single tunnel, and the independent energy orbits are stepwise stacked above each other.

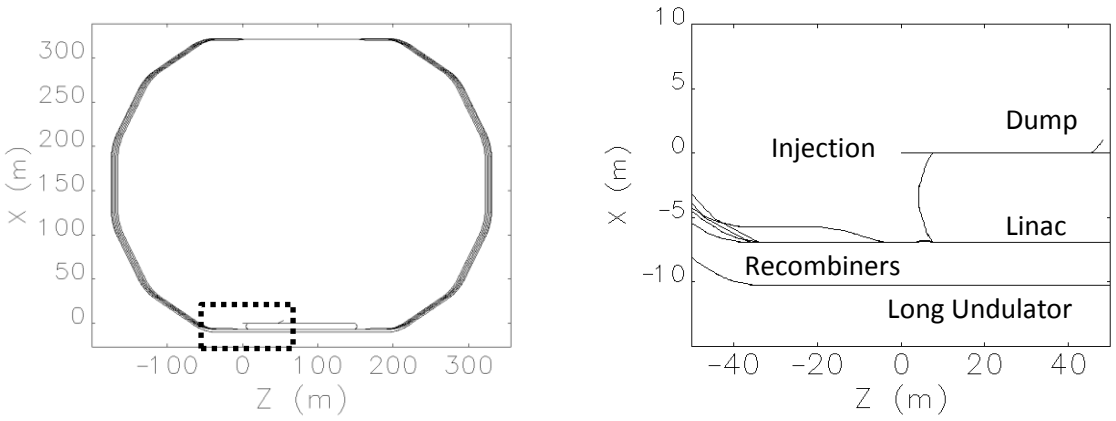

Figure 28. The FSF as depicted by the simulation program, LHS: Blueprint of the FSF, RHS dashed injection region.

The RHS figure highlights the injection stage; first 1 GeV split linac and the multiple orbits. The bunch is injected at the (0, 0) origin and dumped approximately at coordinate (45, 1). The philosophy of the optic design is to share magnets between the different energy beamlines where possible and hold planar symmetry. The first dipole of the low energy recovery arc at (5, -7) is used as part of the chicane merger to the split linac section. The spreaders and recombiners are used to stack the arcs into the tunnel depending on the orbit energy. The long undulator is slightly offset from the first split linac. Figure 3 shows the low energy 1 GeV orbit at the top of the stairwell and both accelerating and decelerating beams are present.

The energy of the bunch as shown in Figure 29 is symmetrically increased from 50 MeV in the injector to a final beam energy of 6 GeV and then recovered to 10 MeV in the dump. After twelve passes, the total linac length traversed is approximately a 5th of the facility length.

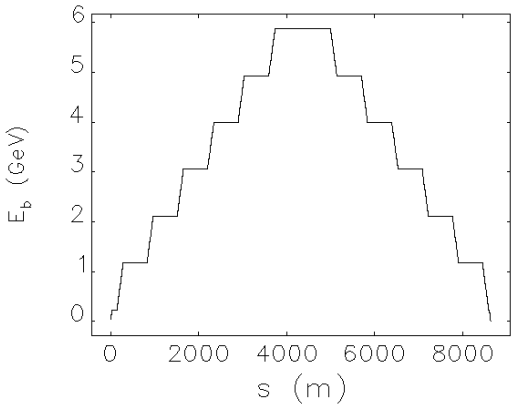

Figure 29. Energy of the bunch throughout the FSF.

Sections of four quadrupoles and suitably long drifts are used to match the transverse beta-functions between the different stages throughout the machine. The lengths of the matching sections are

adjusted to set the path lengths to $N\lambda_{RF}/2$ for recovery. The maximum beta-function value in the linacs is approximately given by the length of the linac, $\beta_{x,y} \sim L_{LINAC} \sim 100$ m.

This value is then at least doubled in the first few quadrupoles of the spreaders to produce peaks over 400 m as seen in Figure 30. The heavy demands on the optic in the spreaders were discussed in Ch5.6. The optic in the linac is designed to suppress the TBBU instability. Triplets are positioned between the cryomodules to minimize the beta-functions and increase the TBBU thresholds.

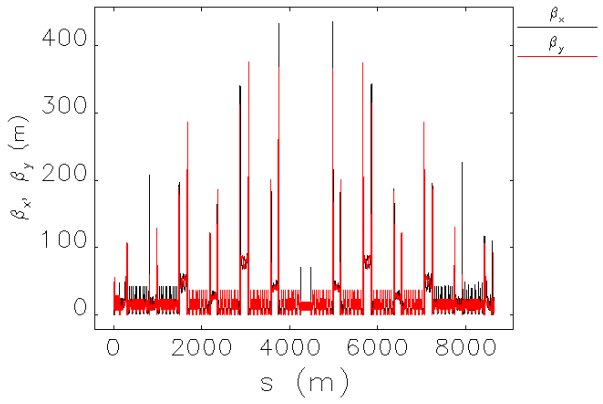

Figure 30. Transverse beta-functions along the FSF.

The high energy arcs in Figure 30 between 2 km < *s* < 7 km, are designed to manipulate the horizontal phase advance to nullify CSR induced emittance growth using the theory described in Ch5.2.4. The 8 km long optic is mostly periodic and repeats throughout each arc.

For completeness, we plot firstly Figure 31 to show the normalized transverse emittance value with the dispersion subtracted. This is in essence the "true" value of the emittance at the undulator since they will be positioned in dispersive free sections. When one compares Figure 31 with Figure 32 it is this dispersion that produces the numerous black peaks in the horizontal arcs, and red only in the vertical spreaders. The peaks are shown not to mislead the reader, moreover to help depict the positioning of the arcs and beam energy at that point.

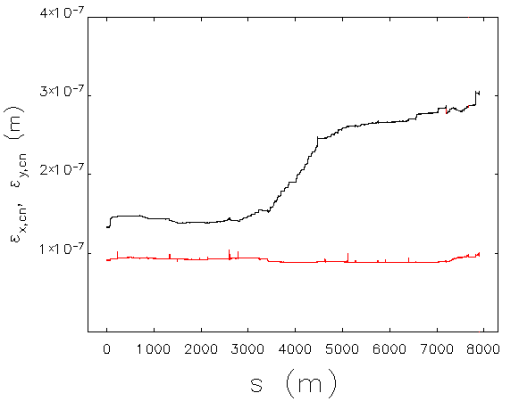

Figure 31. Transversal normalized emittance in the high brightness mode of FSF. Emittance growth due to incoherent synchrotron radiation can be seen in the horizontal plane mainly in the 5 and 6 GeV arcs. Vertical emittance is preserved down to the beam dump.

For the HBM, with all the suppression techniques described in place, the transversal emittance mainly grows due to ISR effects. This effect is analytically estimated for the high energy arc using the radiation integral I_5 in Ch5.2.5. The most effective option is to minimize the bend angle θ and maximize the radius R hence keeping the I_5 value as small as possible throughout the arc. The emittance growth due to ISR given in (55) corresponds well with the value at $s \sim 4$ km plotted in Figure 32.

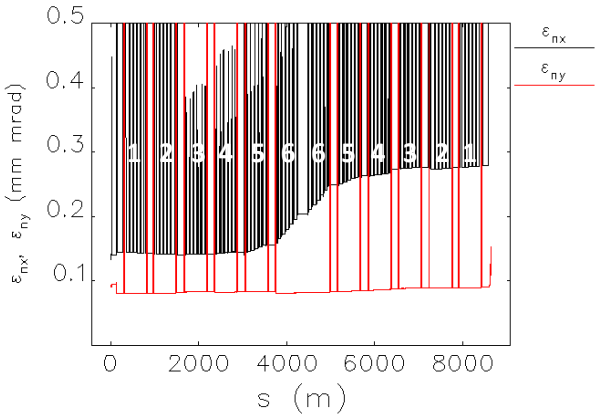

Figure 32. Transverse emittance plot along the FSF.

The transverse emittance growth is kept to a minimum throughout the whole facility to utilize the undulator radiation in all acceleration and deceleration stages in order to maximize user potential. Plotted is both the horizontal and vertical normalized emittance including the dispersive contributions and the beam energy is given in units of GeV.

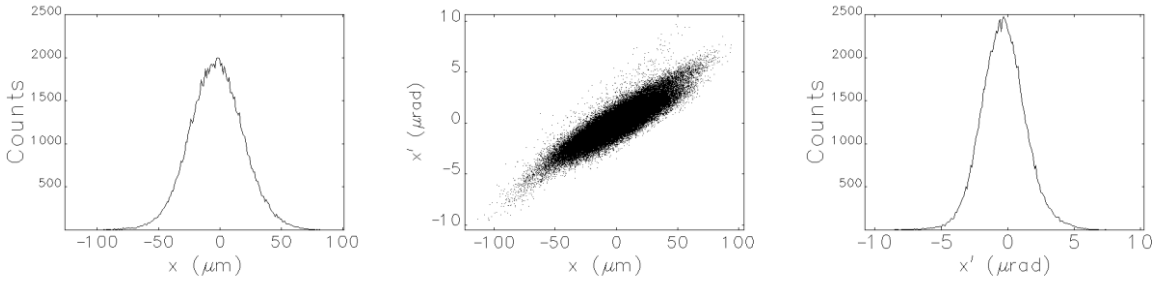

Figure 33. Horizontal beam distribution at the entrance to the long undulator, LHS: *x*-projection, CENTRE: *x,x'* phase space and RHS: *x'*-projection.

The horizontal beam size σ_x as shown in Figure 33 is a few tens of μm at the entrance to the long undulator. The emittance at this point in the facility is ε_{nx} = 0.2 mm mrad. The projections either side of the phase space plot both portray Gaussian like particle distributions.

Table 6 summarizes the main beam dynamic parameters from the HBM start-to-end simulations at various stages in the facility. The input emittance, optimized in the injector Ch5.1, is close to the 0.1 mm mrad project goal value. The radiation effects double this emittance budget at 6 GeV.

Table 6. Start-to-end beam parameters for the 15 pC HBM

Pos	ε_{nx} (mm mrad)	ε_{ny} (mm mrad)	σ_t (ps)	σ_E (10^{-3})	E_b (MeV)
Input	0.13	0.09	3.09	2.93	50
1st user station	0.14	0.08	2.13	0.21	1000
Undulator	0.20	0.08	2.13	0.18	6000
Final user station	0.28	0.09	2.13	0.66	1000
Dumpline	1.24	0.11	3.60	7.26 %	10

Table 6 shows that the beam is still of very high quality even after the final recovery stage at 1 GeV. The normalized emittance is comparable with any present day 3rd generation light source. During the final deceleration stage the relative energy spread of the beam shown on the LHS of Figure 34 increases by a factor $E_{240MeV} / E_{10MeV} = 24$ to over 7 %.

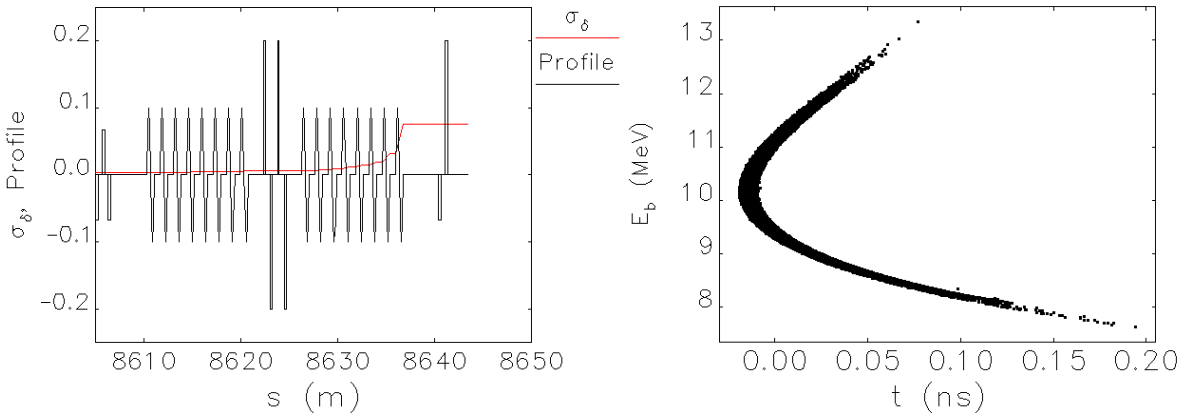

Figure 34. Energy spread characteristics on recovery, LHS: Energy spread in the low energy recovery stage and RHS: Longitudinal phase space plot at the 10 MeV dump.

The profile shows from left to right, firstly the three bending magnets of the low energy chicane, then the two linac sections separated by four matching quadrupoles and finally the bend at *s=8640* m is used to deliver the beam to the dump. The RHS of Figure 34 shows the longitudinal phase space plot of the bunch in the dump. The bunch length has increased from 3.6 ps to 19 ps due to the R_{56} in the bend used to transport the low energy bunch out of the recovery optic.

An energy spread σ_E*<10 %* is seen as unproblematic for the dumpline. Additional quadrupoles in the dumpline after the final bending magnet are foreseen to correct the dispersion and produce a transversal beam size of 1 mm in both planes at the dump.

The optic for the HBM described in this section is fixed. The HBM is the primary mode in the FSF and the following sections on the SPM operation must use this magnetic lattice. The implementation of sextupoles will be shown to be a necessity.

5.7.2 Short Pulse Mode

The motivation for generating short bunches is introduced in Ch4 and more comprehensively in [41]. This chapter summarizes the investigations relevant to the FSF in [41]. The expectations of the spectral properties regarding peak brilliance are shown in Figure 7. The limitation on the fundamental bunch length due to ISR effects is estimated in (59) and precaution is taken to suppress the more prominent effect due to CSR using dedicated optic introduced in Ch.5.2.3. This section expands these findings and integrates them into the FSF to theoretically produce a 10 fs bunch.

The FSF philosophy introduced the facility layout and reiterated the primary operational mode is to achieve high brilliance. The optic for the high energy arcs is fixed and common to both modes, so now attention is paid to the lower achromatic arcs to induce beam compression. A telescopic compression scheme is truncated to the 2nd order to incorporate the non-linear aspects of acceleration and compression. The model is then validated using particle tracking simulations and integrated into the start-to-end optic. The section ends with a brief summary of the beam energy loss due to radiation.

5.7.2.1 Telescopic Compression

The main acceleration stage uses a scheme based on telescopic compression. In this regime the combination of the linac chirps and the longitudinal dispersion (R_{56}) in the Arcs are described as a simple focusing (F) and defocussing (f) lens system, Eq (87).

The shortest pulse achievable from a multi-turn structure is one with full compression in the final arc, blue in Figure 35. However, a remaining high correlated energy spread in the beam (pictorially seen as a slope in the figure) makes the use of long undulators ineffective.

$$\begin{pmatrix} z \\ \Delta E/E \end{pmatrix}_1 = \begin{pmatrix} f/F & F-f \\ 0 & F/f \end{pmatrix} \begin{pmatrix} z \\ \Delta E/E \end{pmatrix}_0 \tag{87}$$

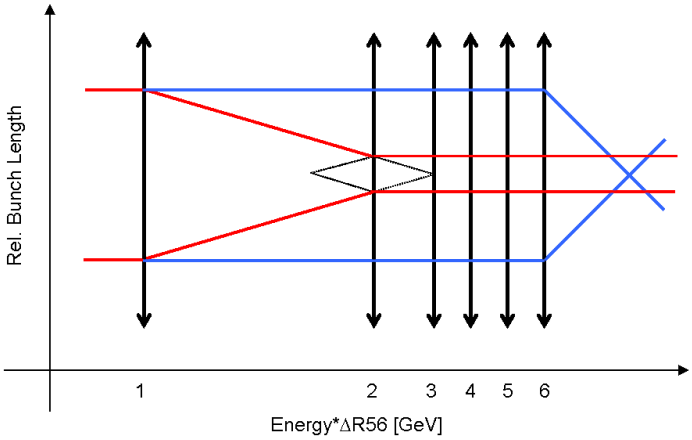

Figure 35. Telescopic bunch compression to preserve energy spread.

In order to remove this correlated energy spread after compression, consider an alternative solution based on a telescopic lattice, red in Figure 35. Implementing the first two arcs as achromats and accelerating either side of on-crest in each linac, the two "lenses" can share the same focal plane, just like for a refracting telescope, to maximize the angular magnification (compression) and still recover the originally low energy correlation of the injected beam.

Assuming simple linear optic, the minimal bunch length of the final beam into the long undulators is restricted by the requirement of an rms energy spread given by

$$\frac{\Delta E}{E} \sim \frac{1}{N} \sim 10^{-4}. \tag{88}$$

In order to compress the beam the first and second Arc are required to have non-zero longitudinal dispersion (R_{56}). To restrict unwanted higher order beam degradation the maximum value of R_{56} in each complete ARC was limited to 20 cm. This is attainable using simple periodic optic such as double (DBA) or triple (TBA) bend achromats without excessive demands being placed on the strong focusing quadrupoles. With this and the telescopic compression technique in mind, suitable values for the magnification were analytically investigated. A compromise between minimum bunch length and energy

spread for a given linac phase and R_{56} values was found. Taking $\sigma_t \sim \varepsilon_z / (\Delta E/E)$ and implementing an input beam of say 2 ps, the minimum bunch length is approximately 10 fs.

The parameters from the numerical calculations are seen as the starting point for the optimization of the start-to-end particle tracking simulations. The general compression scheme for the SPM is listed below. Each off-crest acceleration followed by achromatic arc constitute to a 'lens' in the telescopic compression scheme in the lower energy acceleration sections. The first two arcs up to a beam energy of 2 GeV have positive R_{56} values. On recovery the phase is shifted in both linacs $\phi_d \rightarrow \phi_a + 180°$ (ERL process) and the recovery arcs have the corresponding negative R_{56} values.

Off crest acceleration in both 1 GeV linacs	$\phi_1 = 10°$ and $\phi_2 = -20°$

Telescopic Compression

Arc 1 TBA R_{56} = 20 cm

Arc2 TBA R_{56} = 5 cm

High Energy Arcs

3 GeV -> 6 GeV DBA with anti-magnet Figure 14

Off crest deceleration in both 1 GeV linacs	$\phi_1 = 190°$ and $\phi_2 = 160°$

6 GeV -> 3 GeV DBA with anti-magnet

Telescopic Decompression

Arc 2 TBA R_{56} = -5 cm

Arc1 TBA R_{56} = -20 cm

The main points to consider from this SPM optic is that the recovery is symmetric in the sense the phase in the linacs shift by 180° and the R_{56} values on deceleration are negative to again remove all correlated energy spread on recovery for optimal beam conditions at the entrance to the beam dump transferline. The initial beam parameters are determined in the injector. The following section summarizes the main simulation results from the appendix for the 5 pC bunch charge case.

5.7.2.2 Compression in the Injector

Producing a femto-second low energy spread pulse starts at the Gun. Here in the 1st part of the two stage injection scheme the longitudinal electron beam properties, Table 7, are restricted by the photo-injector laser pulse and the superconducting RF acceleration. A 3rd harmonic cavity is used to linearize the longitudinal phase space and lower the emittance (see Figure 48). The primary subtle compression in the Merger between the Booster and linac minimizes transversal emittance growth due to space charge effects.

Table 7. Injector longitudinal beam parameters from ASTRA simulations 5 pC.

Component	Bunch Length (mm)	Long. Emittance (keV mm)	Energy (MeV)
Gun	2.37	11.05	1.90
Booster	2.23	0.84	9.47
Merger	0.63	1.11	9.47
Two Stage Injector Linac Entrance	0.60	2.36	53.41

The 2nd part of the two stage injection scheme uses an injector Linac and Arc to prepare the beam for the main accelerator. The combination of off-crest acceleration in the linac and the R_{56} in the Arc further compress the beam from 2 to 1 ps. Investigations described later in this chapter show the extent of this compression at this stage is critical for the optimum beam properties at high energy. Creating the shortest bunch length is the goal of this SPM. To actively control the bunch length in each Arc for a "real" beam that is subject to higher order effects a longitudinal emittance recovery scheme is considered.

5.7.2.3 Longitudinal Emittance Recovery

The longitudinal emittance can be described as an ellipse occupying a density of particles in ($c\Delta t$, δ) phase space. The non-linear properties of RF acceleration can alter the longitudinal phase space distributions varying the normalized emittance. An emittance compensation scheme using higher order magnetic terms created in the Arcs to counteract the non-linear RF acceleration is described here.

Using the linacs relative energy (89) and the Arcs bunch length (90) variations respectively one can calculate the emittance variation across the two stages as follows.

Linac

$$\begin{aligned}\delta_1 &= \delta_0 + R_{65}c\Delta t_0 + T_{655}(c\Delta t_0)^2 \\ c\Delta t_1 &= c\Delta t_0\end{aligned} \tag{89}$$

+ARC

$$\begin{aligned}\delta_2 &= \delta_1 \\ c\Delta t_2 &= c\Delta t_1 + R_{56}\delta_1 + T_{566}\delta_1^2\end{aligned} \tag{90}$$

Keeping only second order terms, assuming $\delta_0 = 0$, the emittance can be approximated as

$$\begin{aligned}\varepsilon_2^2 &= \left\langle (c\Delta t_2)^2 \right\rangle \left\langle \delta_2^2 \right\rangle - \left\langle c\Delta t_2 \delta_2 \right\rangle^2 \\ \varepsilon_2^2 &\cong \left(T_{566}R_{65}^3 - T_{655}\right)^2 \left\langle (c\Delta t_0)^4 \right\rangle \left\langle (c\Delta t_0)^2 \right\rangle\end{aligned} \tag{91}$$

One can interpret (91) as a useful tool to control the normalized emittance. The accelerating phase determines both the R_{65} and T_{655} terms and sextupoles terms in the bend can manipulate T_{566} to compensate longitudinal emittance growth.

This tool was implemented on the FSF optic. Finding the optimum settings to control the longitudinal emittance in the extensive FSF optic is an iterative process. To save on computational time, the next few figures shown were produced with only a sample fraction of the original injector particle distribution and the radiation effects were partially restricted.

Figure 36 shows the longitudinal emittance recovery scheme adapted for the two stage telescopic bunch compression, the vertical axis is logarithmic. (where $\log 10^{-14}$ s → 10 fs). Using

$$\varepsilon_{nz} = \gamma\varepsilon_z \tag{92}$$

the normalized longitudinal emittance, shown as a black line initially increases due to the off crest acceleration in the pre-injector linac and then once again in the first 1 GeV linac. The phase in each linac is tuned so that after the first Arc, at approximately 700 m, the longitudinal emittance of the injected beam is fully recovered.

This allows the full potential for further 2nd order compression in the following arc. The combination of the various T_{566} values in all the low energy arcs and their respective spreaders, are optimized for a given linac phase. The process is then reversed and iterative until both phase setting and arc optic are optimal to produce a final bunch length in red slightly less than 10 fs at 2 GeV.

After optimization the deviation from the starting parameters is only slight. The SPM condition to produce the plot in Figure 36 is ϕ_1 = 10.45° and ϕ_2 =-21.00° with $R_{56,Arc1}$=20 cm and $R_{56,Arc2}$=8 cm. Only the longitudinal dispersion in the second Arc was significantly changed in order to retain the proposed telescopic compression qualities.

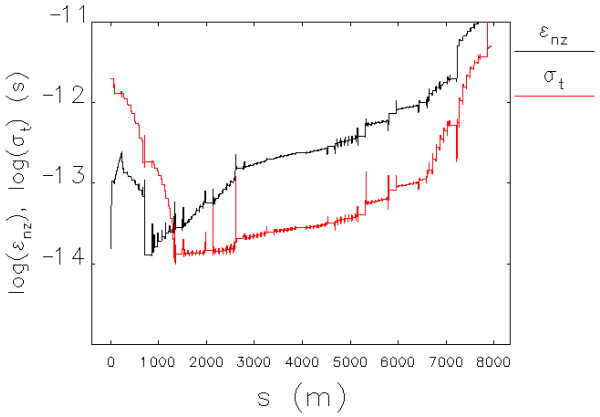

Figure 36. Longitudinal bunch properties along the FSF.

One can also apply additional longitudinal gymnastics in the high energy arcs as shown in Figure 37 to obtain 10 fs at 6 GeV. Additional sextupoles are implemented so that the increase in bunch length in the 4 GeV spreader (step at *s*=2500 m) is re-compressed using 2nd order terms to replenish the 10 fs project goal at 6 GeV. However, the inclusion of such higher order magnets has a negative impact on the transversal emittance and realistic recovery is not possible at a bunch charge of 5 pC using the present spreader optic. A compromise is necessary as the spreader optic is common to both operation modes.

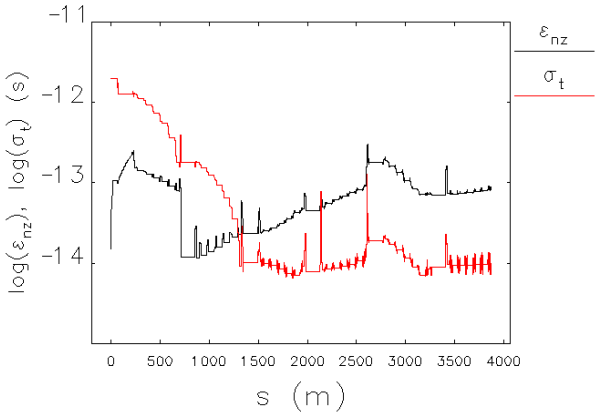

Figure 37. Additional 2nd order bunch compression in the high energy arcs using sextupoles.

5.7.2.4 Start-to-end SPM simulations

The results of the SPM start-to-end simulations shown in this section were undertaken as in the case of the HBM, with 100 000 particles and all relevant radiation effects accounted for. As previously discussed in Ch5.2.4 although a slight over approximation, the 1D CSR wake model in Elegant will suffice. Bunches of 1, 3 and 5 pC charge were successfully tracked through the full optic. The figures in this section are all taken for the 3 pC case, unless otherwise stated.

Figure 38 shows in the blue dashed boxes, the asymmetric beta-functions in the low energy stages of acceleration and recovery. The Twiss-parameters in the arcs differ according to their longitudinal dispersion value. Bunch compression and decompression is achieved with positive and negative R_{56} values respectively. The maximum beta-function value in both planes in all the arcs is less than 50 m. Again, as was the case for the HBM, the peaks are due to the spreaders and recombiners. The remaining linear optic in the high energy arcs is identical to the HBM.

Sextupoles are implemented into all spreaders and recombiners up to 3 GeV. This is necessary to suppress the dramatic growth in the vertical emittance when passing through these short but complex structures. The vertical beam size due to the T_{366} term became comparable with the geometric beam size as a relatively high energy spread is present in the SPM.

$$\sigma_{y,geo} \sim \sqrt{\varepsilon\beta} \sim 25\mu m \quad (93)$$

$$\sigma_{y,2nd} \sim T_{366}\delta^2 \sim 14\mu m \quad (94)$$

The sextupoles were used to correct $T_{366}\rightarrow 0$ to allow for a safe passage through the spreaders. Additional care was taken not to significantly change the other 2nd order terms relevant for the longitudinal emittance recovery scheme such as T_{566}.

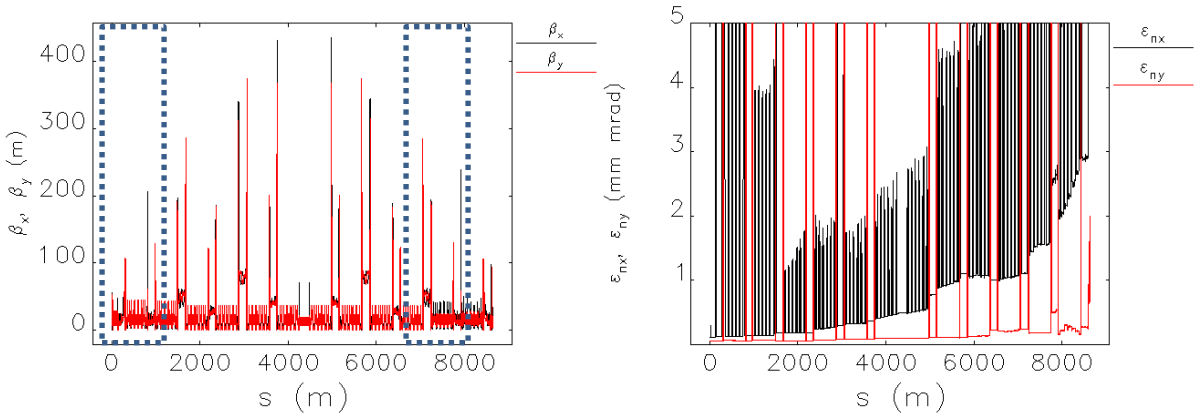

Figure 38. Transversal beam properties of the SPM, RHS: Beta-functions and LHS: emittance growth along the FSF.

The additional energy spread due to the CSR wake dictates the trend of the transversal emittance plots shown on the RHS of Figure 38. The non-linear energy correlation depending on the longitudinal bunch properties dominate this operational mode. This imprint is not seen in the HBM as it operates outside of this regime. For the SPM, the bunch length is less than 50 fs for the majority of the facility as shown in RHS of Figure 39.

Sextupoles are required in the final recovery arc to suppress the horizontal emittance growth due to chromatic aberrations. Without correction, the horizontal beam size becomes so large it spoils the other beam dimensions and causes substantial beam loss even before the dumpline when one assumes a vacuum chamber diameter of 40 mm. Again refer to [41] for a comprehensively investigation. Here the sextupole strengths

$$k_s = \frac{e}{pc}\frac{2B_{max}}{r^2} \tag{95}$$

were compared with the magnetic field at the pole B_{max} to be comfortably within the technical limits for the 1 GeV recovery arc.

The energy spread of the bunch for both the HBM and SPM are compared in Figure 39. The main difference occurs in the low energy ($s<2$ km) stages of the facility where off-crest acceleration is required for the bunch compression in the SPM. At 6 GeV (s~4 km), the energy spread of the HBM is at least a factor 5 lower than that of the SPM. At the dump, the values are both in the region of 10 % due to the fact that the HBM is tracked with considerably more bunch charge than the SPM.

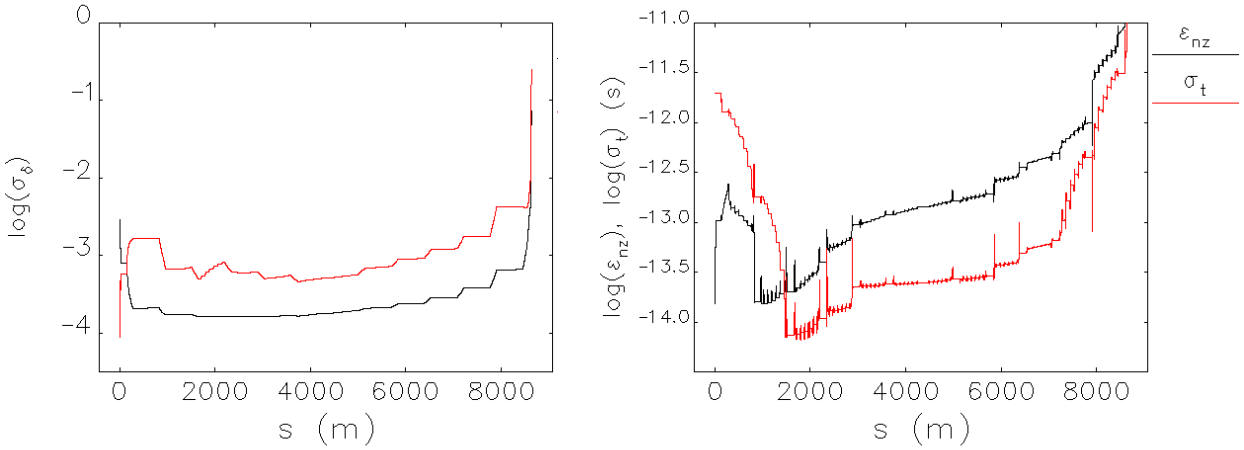

Figure 39. Longitudinal beam properties of the FSF, RHS: Energy spread comparison for the two modes, black HBM and red SPM, LHS: Longitudinal emittance and bunch length.

The longitudinal bunch properties on the LHS of Figure 39 show the emittance recovery technique, used to good effect. As intended the longitudinal emittance ε_{nz} of the injected bunch is recovered during the bunch compression stages. With all relevant radiation effects simulated, the bunch length at 3 GeV is less than 10 fs and steadily increases to 25 fs at full energy. As already mentioned, other than the

sextupoles in the spreaders and recombiners, no additional higher order magnets are required to produce compression in this elegant manner.

Figure 40 compares the longitudinal properties of the SPM bunch at 240 MeV and 10 MeV. The average beam energy is subtracted in both cases so that the plots overlap. The relative energy increases by the fraction of the deceleration to approximately 14 %. Without careful consideration, the fraction of particles with energies above the ±5 MeV acceptance may be lost in the dumpline.

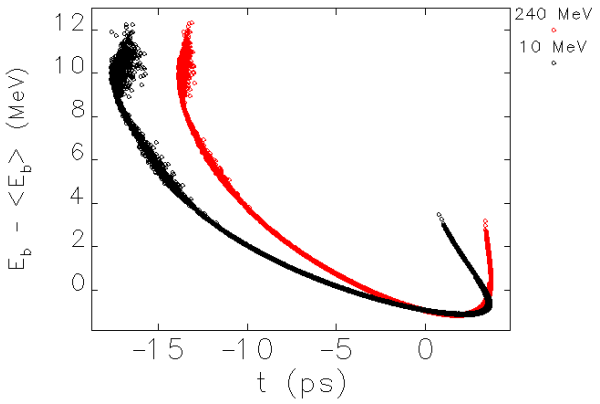

Figure 40. Comparison of the longitudinal phase space plots at the final stages of recovery.

Table 8 presents the results of the most relevant beam properties of the SPM start-to-end simulations. The input from the injector studies is successfully tracked through the 8 km optic to the dump. Even in this SPM, the electron beam properties up till the point of low energy on recovery remain admirable. Normalized emittances of 1 mm mrad combined with 50 fs bunch lengths are again beyond the capabilities of present 3rd generation facilities. The bunch length in the final stage of recovery compared to injection has doubled. This is instigated as a compromise to relax the transversal plane parameters in these critical sections of the machine.

Following the introduction in Ch.5.2.1 the steady state energy loss of the bunch due to CSR can be approximated as

$$\Delta E_{CSR} \sim \frac{q^2}{\sigma_z^{4/3}} \quad . \tag{96}$$

Where q is the bunch charge and σ_z is the bunch length. Since the beam degradation due to the CSR wake is heavily dependent on the bunch charge, one can envisage lowering the charge of a given injector input until 10 fs at 6 GeV is reached without sextupoles in the higher energy arcs. Lowering the bunch charge addresses the impact of CSR but the damaging chromatic effects of the intricate spreaders due to the beams high energy spread in this operation mode still exist. One cannot freely optimize the spreaders higher order terms to cancel out this effect and achieve full compression. The beam clearly needs to be short but not at the cost of beam loss in another plane.

Table 8. Start-to-end beam parameters for the 3 pC SPM

Pos	ε_{nx} (mm mrad)	ε_{ny} (mm mrad)	σ_t (fs)	σ_E (10^{-3})	E_b (MeV)
Input	0.11	0.06	1990.09	0.46	50
Two stage injection	0.12	0.06	1281.99	0.57	240
Low energy arcs	0.18	0.06	7.39	0.71	2000
High energy arcs	0.30	0.08	22.59	0.62	4000
Long undulator	0.49	0.10	24.73	0.52	6000
High energy arcs	1.00	0.23	48.70	0.92	4000
Low energy arcs	2.52	0.49	452.22	1.77	2000
Two stage recovery	8.47	0.93	3924.42	6.34	240
Dumpline	32.88	0.64	4430.29	14.66 %	10

Equation (96) can be reduced to the single particle energy loss (in an assumption, that this energy spread limits the beam recovery efficiency through unacceptable beam losses) as

$$\Delta E_{CSR} \sim \mathrm{q}/\left(\sigma_t^2 - \sigma_0^2\right)^{2/3} \tag{97}$$

where σ_0=5 fs is the zero-charge bunch length. Particle tracking simulation results with both the 3 and 5 pC bunches show the SPM to be dominated by CSR effects. Intricate 2nd order optic is used on recovery to ensure that the energy spreads of these two bunch charges at the dump are similar. If one assumes that these settings represent the `limit' for any given bunch charge the results can be extrapolated to form a boundary of the minimum bunch length for a given charge.

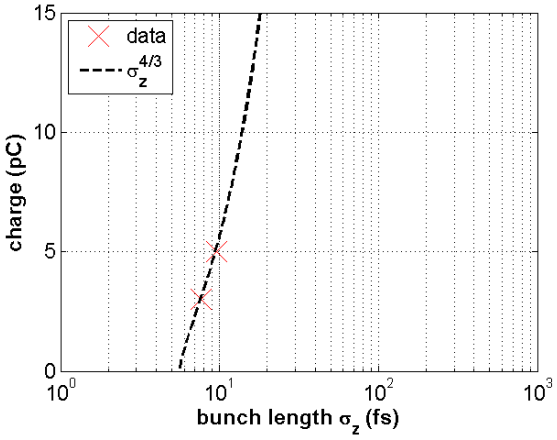

Figure 41. Boundary of minimum bunch length due to CSR effects for the FSF.

Bunch charges and lengths to the left of the boundary are not feasible; the distortion due to CSR will be too large to recover the beam at 10 MeV. To the right of the boundary all settings are possible. The upper charge boundary of 15 pC is the limit from the injector studies and the 1 ps long bunch extremity on the far right hand of the figure is due to the RF curvature in the linac. Notably the HBM would exist in the top right hand corner of Figure 41 suggesting that the operation mode is well above the CSR limit and bunch compression is possible if it is beneficial for the light source.

In the SPM, the strict transversal properties are then sacrificed to achieve fs bunch lengths and maximum peak brilliance B_p. The largest value of brilliance is a correct balance between low transversal emittance and relatively short bunch lengths.

For the peak brilliance one needs to consider the 6D phase space of the emitted photons. The bunch length is then extremely relevant in this case and the radiation associated with (9) needs to be considered per bunch rather than second. The power density of the emitted photons becomes equivalent to the brilliance of the electron beam

$$B_p = \frac{\mathrm{N}}{(2\pi)^2 \varepsilon_x \varepsilon_y \varepsilon_z} \equiv \frac{\mathrm{qC}_\gamma}{(2\pi)^2 \varepsilon_x \varepsilon_y \varepsilon_z}. \quad (98)$$

where C_γ is the number of photons emitted per electron and q is the bunch charge. Figure 42 highlights the necessity of optimizing for the minimum emittance in all planes. The SPM compression scheme uses only the low energy arcs and full compression is achieved at 2 GeV. The 5 pC bunch is the highest of the first peaks at s~1 km as the bunch lengths of all three charges are approximately 10 fs. The trend that follows is due to the extent of the CSR induced transversal beam degradation and bunch lengthening. The next peaks at 3 GeV show both the 3 and 5 pC bunches emitting similar peak brilliance. Then as the transversal emittance growth establishes itself in the high energy arcs, the brilliance of the higher charged beams falls away. At 6 GeV, (largest peak at s~4 km) the light source produces most brilliance for lower charges. Also at 6 GeV one sees a similar fall in peak brilliance for all charges over the final high

energy turn due to the ISR induced emittance growth that is heavily dependent on beam energy $\Delta\varepsilon_{n,ISR} \sim E_b^6$.

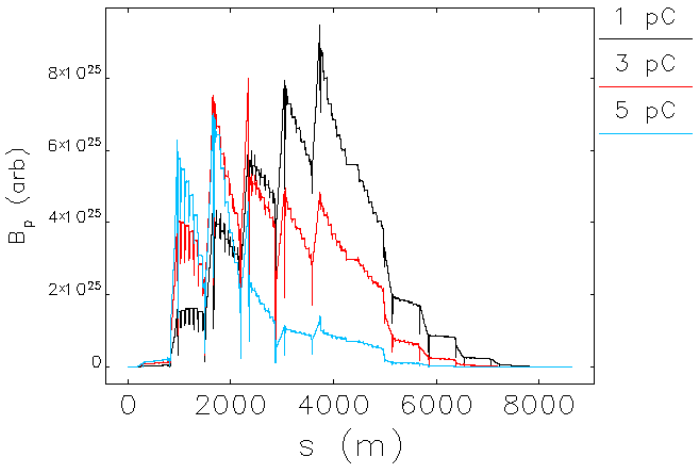

Figure 42. Peak brilliance curves throughout the FSF for various bunch charges of the SPM.

If bunch compression was possible in all arcs, the highest peak for a given charge could be engineered to suit the user using a staggered compression scheme.

5.7.2.5 Energy Loss Considerations

It is envisaged that the energy loss due to radiation in the arcs alone will exceed the original 10 MeV injection energy of the FSF. This section describes an energy loss budget for the different sources of radiation induced energy loss. Common to both modes, the energy loss due to ISR in an FSF arc investigated in Ch.5.2.5 is in the order of 8 MeV. In a similar manner, the energy loss due to the abundance of undulators given that there are five sections each 40 m long between the 30° periodic bends and using the undulator parameters in Table 3 amounts to an energy loss of 4 MeV in the 6 GeV turn.

The CSR contribution in the HBM is negligible compared to that of the SPM. The amount of energy loss due to CSR taken from the results of the particle tracking simulations is shown in Figure 43 for a 5 pC bunch charge in the SPM.

The large contribution from CSR at 3 GeV is in keeping with the shorter bunch lengths, seen as the light blue line. The shortest bunch is created after the 2 GeV arc and hence the CSR effect is most dominant in the following 3 GeV arc. The bunch length in the final two high energy arcs is relatively stable and accordingly shows similar CSR proportions.

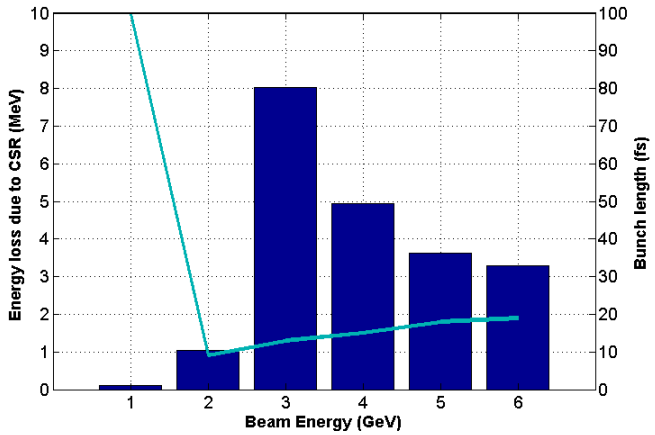

Figure 43. Energy loss due to CSR for the 5 pC SPM on acceleration.

Equation (99) for a rectangular bunch [32] model can be used to verify the total CSR contribution. For the 5 pC bunch the total energy loss would be approximately 20 MeV which is in good agreement with the particle tracking results

$$\Delta E_{CSR} \approx \left(\frac{3^{2/3} e^2 N^2}{l_b^{4/3} R^{2/3}}\right)(R\varphi_m)\left(1+\frac{3^{1/3}4}{9}\frac{l_b^{1/3}}{R^{1/3}\varphi_m}\left[\ln\left(\frac{l_b\gamma^3}{R}\right)-4\right]\right), \quad (99)$$

Booster modules were implemented in the simulations to compensate for this energy loss due to radiation. These modules operate without energy recovery and require approximately 300 kW and 200 kW of total power for the HBM and SPM respectively. The location and peak voltage of these modules were studied in order to optimize their effectiveness. For the SPM one would require a minimum of eight modules, shared between acceleration and deceleration, located after each (3→6 GeV and 6→3 GeV) high energy arc in the beamline before their respective spreaders. The boosters were optimized to keep the mean energy of the bunch to ±100 keV of the reference particle defined by Elegant.

6 Costs estimate

Table 9. Costs estimation of FSF.

Component	Unit cost	Total cost
1. Infrastructure/tunnel		
a) Land	0.16 k€/m^2	31 M€ (350x550 m^2)
b) Tunnel	10 k€/m	15 M€ (~1.5 km)
c) Users buildings		50 M€
d) Technical buildings		10 M€
Subtotal		110 M€
2. SRF		
a) Cryogenic plant		20 M€
b) Cryomodules	5 M€	100 M€
c) RF generators	1.5 M€ for injector (200 kW), 0.4 M€ for linacs (each of 10 kW)	65.5 M€
Subtotal		190
3. Warm machine		
a) Magnets	10 k€	43 M€ (~ 4300 magnets)
b) Undulators	1, 5 M€ - short, long	65 M€ (60 short + 1 long)
c) Vacuum system + diagnostics/control	10 k€/m	75 M€
d) Power supplies	10 k€	43 M€
Subtotal		230 M€
4. People		
a) Staff	50 k€/year	50 M€ (10 years, 100 people)
b) Beamline scientists	100 k€/year	50 M€ (10 years, 50 people)

c) Users stations		200 M€
d) Overhead	Not included	Not included
Subtotal		300 M€
Total		830 M€

7 References

1. H.Wiedemann, “Particle accelerator physics”, 3rd ed. Springer Berlin Heidelberg New York.
2. A. Föhlisch, A. Jankowiak, J.Knobloch, P. Kuske A. Neumann, M. Ries and G. Wüstefeld, “Vision for the Future: BESSY^{VSR} A Variable Pulse Length Storage Ring”, ICFA Workshop on Future Light Sources, 2012.
3. G. Wuestefeld, A. Jankowiak, J. Knobloch, M. Ries, “SIMULTANEOUS LONG AND SHORT ELECTRON BUNCHES IN THE BESSY II STORAGE RING”, Proceedings of IPAC’11, pp. 2936-2938.
4. P. Elleaume, “Ultimate Hard X-Ray Storage-Ring-Based Light Source”, white paper.
5. M. Scheer, WAVE - A Computer Code for the Tracking of Electrons through Magnetic Fields and the Calculation of Spontaneous Synchrotron Radiation, ICAP 2012.
6. “X-ray data booklet” available online at http://xdb.lbl.gov/
7. “A next generation light source” proposal, LBNL, December 2010.
8. K. Flöttmann, ”Astra”, DESY, Hamburg, www.desy.de/~mpyflo
9. I.V.Bazarov, Synchrotron radiation representation in phase space, PRST AB 15, 050703 (2012)
10. S.V. Miginsky. Space charge effects, coherence of charge oscillation, and emittance. Technical Physics, 2008. Vol. 78, №9, pp. 96-106.
11. S.V. Miginsky. Emittance compensation of elliptical beam. NIM A 603 (2009), pp 32-34.
12. S.V. Miginsky. Scope of the locally cold beam model. NIM A 603 (2009), pp 28-31.
13. D. Douglas, Thomas Jefferson Natl. Acc. Lab. Tech. Note, JLAB-TN-98-012 (1998); J.H. Wu et al., Proc. 2001 Particle Accelerator Conference, Chicago, USA (IEEE, New Jersey, 2001) p. 2866.
14. R. Hajima, JAERI, R-matrix analysis of the CSR effect in a future ERL light source, Proceedings of APAC 2004, Gyeongju, Korea.
15. P. Emma, R. Brinkmann, ‘‘Emittance Dilution Through Coherent Energy Spread Generation in Bending System’’, SLAC Report 7554, May, 1997.
16. S.Di Mitri, M. Cornacchia, S. Spampinati, ‘‘Cancellation of Coherent Synchrotron Radiation Kicks with Optics Balance’’, Physical Review Letters 110, 014801, 2013
17. Ya.S. Derbenev, V.D. Shiltsev, ‘‘Transverse Effects of Microbunch Radiative Interaction’’, SLAC Report 7181, June, 1996.
18. C.E. Mayes, G.H. Hoffstaetter, ‘‘Coherent Synchrotron Radiation Simulations for the Cornell Energy Recovery Linac’’, Proceedings IPAC 2010, Kyoto, Japan.
19. V. Yakimenko, et.al, ‘‘CSR Shielding experiment’’, Proceedings of 2011 Particle Accelerator Conference, New York, USA
20. R.D. Ryne et al, ‘‘Lage Scale Simulation of Synchrotron Radiation Using a Lienard-Wiechert Approach’’, Proceedings IPAC 2012, New Orleans, USA.
21. A.W. Chao, M. Tigner, Handbook of Accelerator Physics and Engeneering, 1998, Chapter 2, Sec. 2.1, p. 50.
22. M. Dohlus, T. Limberg, CSRtrack User’s Manual
23. A.N. Matveenko, O.A. Shevchenko, N.A. Vinokurov, Isochronous Bend for High Gain Ring FEL, Proceedings of FEL 2004.
24. Y. Petenev, Analysis of injection and recovery schemes for ERL based light source, PhD thesis, Humboldt-Universität zu Berlin, 2014.

25. Claude M. Lyneis, Michael S. McAshan, Roy E. Rand, H. Alan Schwettman, Todd I. Smith and John P. Turneaure, The Stanford Superconducting Recyclotron, IEEE Transactions on Nuclear Science, Vol. NS-26, No. 3, June 1979.
26. P.Axel, L.S.Cardman, H.D.Graef, A.O.Hanson, R.A.Hoffswell, D.Jamnik, D.C.Sutton, R.H.Taylor, and L.M.Young, Operating Experience with MUSL-2, IEEE Transactions on Nuclear Science, Vol. NS-26, No. 3, June 1979.
27. R.E. Rand and T.I. Smith, Beam optical control of beam breakup in a recirculating electron accelerator, Particle accelerators, Vol. 11, pp. 1-13 (1980).
28. J.J. Bisognano, R.L. Gluckstern, in Proceedings of the 1987 Particle Accelerator Conference, Washington, DC (IEEE Catalog No. 87CH2387-9), pp. 1078-1080.
29. G.A. Krafft, J.J. Bisognano, in Proceedings of the 1987 Particle Accelerator Conference, Washington, DC (IEEE Catalog No. 87CH2387-9), pp. 1356-1358.
30. G.H. Hoffstaetter, I.V. Bazarov, „Beam-breakup instability theory for the energy recovery linacs", Phys. Rev. ST AB 7, 054401 (2004).
31. E. Pozdeyev, et al., "Multipass beam breakup in energy recovery linacs", NIM A 557 (2006) 176-188.
32. E.L. Saldin, E.A. Schneidmiller and M.V. Yurkov, On the Coherent Radiation of an Electron Bunch Moving in an Arc of a Circle, NIM A 398 (1997) 373-394.
33. N.A. Vinokurov et al., Proc. of SPIE Vol. 2988, p. 221 (1997).
34. Generic Beam BreakUp (GBBU) by E. Pozdeyev.
35. E. Pozdeyev, Regenerative multipass beam breakup in two dimensions, PRST AB 8, 2005.
36. K. Wille, Physic der Teilchenbeschleuniger und Synchrotronstrahlungsquellen, B.G. Teubner Stuttgart, 1992. (in German).
37. I.V.Bazarov, Synchrotron radiation representation in phase space, PRST AB 15, 050703 (2012).
38. M. Borland, "User's Manual for elegant," available on-line at http://www.aps.anl.gov/Accelerator_Systems_Division/Accelerator_Operations_Physics/manuals/elegant_latest/elegant.html
39. Z. Huang et al., "Measurement of the LCLS laser Heater and its impact on the X-ray FEL performance", SLAC-PUB-13854.
40. M. Borland, "Simple method for particle tracking with coherent synchrotron radiation" Phys. Rev. ST, Vol 4, 070701 (2001).
41. T. Atkinson, Modeling of Magnetic Optic for the Short Pulse Mode Operation of Energy Recovery Linac based Light Sources, PhD thesis, Humboldt-Universität zu Berlin, 2015.

8 Appendix A: Brilliance of the undulator radiation in the case of an electron beam with an energy spread

The radiation spectrum of a single electron on axis of an undulator is given by [1, 23.53]. For a large enough number of undulator periods N>>1 the spectrum is proportional to

$$\frac{\mathrm{d}^2 W_k(\omega)}{\mathrm{d}\omega \mathrm{d}\Omega} \sim \mathrm{sinc}^2(\pi N \Delta\omega_k/\omega_1)$$

where $\Delta\omega_k/\omega_1 = \omega/\omega_1 - k$, N is the number of undulator periods, k is the harmonic number, ω_1 is the frequency of the first harmonic. The width of a harmonic for a single electron or a monoenergetic beam can be calculated as

$$\pi N \Delta\omega_k/\omega_1 = \pi \Rightarrow \Delta\omega_k/\omega_k = 1/kN.$$

On the other hand, for an electron with the energy error $\Delta\gamma/\gamma = \delta$ the spectrum is shifted ($\lambda = \frac{d}{2\gamma^2}\left(1+\frac{K^2}{2}\right)$) by

$$\Delta\omega/\omega = -\Delta\lambda/\lambda = 2\delta$$

It is obvious, that for some harmonic number k $\frac{1}{kN} < 2\delta$ and brilliance of the radiation will be decreased (the spectrum of the radiation will be broadened) due to the beam energy spread.

In the following we will derive an approximated formula for the brilliance including the energy spread of the bunch. We do it for a zero-emittance electron bunch for the sake of simplicity. More rigorous treatment which allows to account for transverse emittances and the energy spread of the beam simultaneously can be found in [37]. For our aim it is enough to use more simple approximation.

The form of the spectral line will be given by a convolution of the single electron spectrum and the energy distribution of the electrons in the bunch (incoherent radiation).

$$\frac{\mathrm{dN}}{\mathrm{d}\lambda} \sim \int \mathrm{sinc}^2(\pi N \Delta\omega_k/\omega_1) f(\gamma-\gamma_0) d(\gamma-\gamma_0)$$

where *f(γ)* is the energy distribution in the bunch and γ_0 is given by the average bunch energy.

We define the brilliance at a wavelength with a maximal spectral brightness. For symmetrical distributions *f(γ)* the maximal spectral brightness is at $\lambda = \frac{\lambda_1(\gamma_0)}{k}$. In this case

$$\frac{\mathrm{dN}}{\mathrm{d}\lambda}_{\max} \sim \int \mathrm{sinc}^2(2\pi kN\frac{\gamma-\gamma_0}{\gamma_0}) f(\gamma-\gamma_0)d(\gamma-\gamma_0) \sim \int \mathrm{sinc}^2(\tau)\exp\left(-\left(\frac{\tau^2}{8(\pi kN\delta)^2}\right)\right)d\tau$$

where we used $\Delta\omega/\omega = -\Delta\lambda/\lambda = 2\delta$, $\omega_k = k\omega_1$ and assumed the Gaussian energy distribution with an rms relative energy spread δ.

$$f(\gamma-\gamma_0) = \frac{1}{\sqrt{2\pi}\delta\gamma_0}\exp\left(-\left(\frac{(\gamma-\gamma_0)^2}{2\delta^2\gamma_0^2}\right)\right).$$

The previous integral cannot be expressed in elementary functions, but we can find a reasonable approximation for it. If the spectrum of undulator radiation of a single electron were a Gaussian, the spectrum of the bunch with a Gaussian energy distribution would be a Gaussian again, the width of which would be a square root of the sum of squares of the widths of energy spread and spectrum. This will be hold true approximately in our case too. Therefore, we take the limit of the spectral brightness for monoenergetic bunch

$$\frac{\mathrm{dN}}{\mathrm{d}\lambda}_{\max} \sim \int \mathrm{sinc}^2(\tau)\exp\left(-\left(\frac{\tau^2}{8(\pi kN\delta)^2}\right)\right)d\tau \xrightarrow{\delta\to 0} \sqrt{8\pi}\cdot\pi kN\delta$$

and the limit for large energy spread $kN\delta >> 1$:

$$\frac{\mathrm{dN}}{\mathrm{d}\lambda}_{\max} \sim \int \mathrm{sinc}^2(\tau)\exp\left(-\left(\frac{\tau^2}{8(\pi kN\delta)^2}\right)\right)d\tau \xrightarrow{\delta >> 1/kN} \pi .$$

Comparing them we see, that for all δ should hold approximately true

$$\frac{\mathrm{dN}}{\mathrm{d}\lambda}_{\max} \sim \frac{\mathrm{dN}}{\mathrm{d}\lambda}_{\max,\delta=0} \frac{1}{\sqrt{1+8\pi(kN\delta)^2}} .$$

This expression is asymptotically correct for very small and very large $kN\delta$. How good this approximation is can be seen from the following plots.

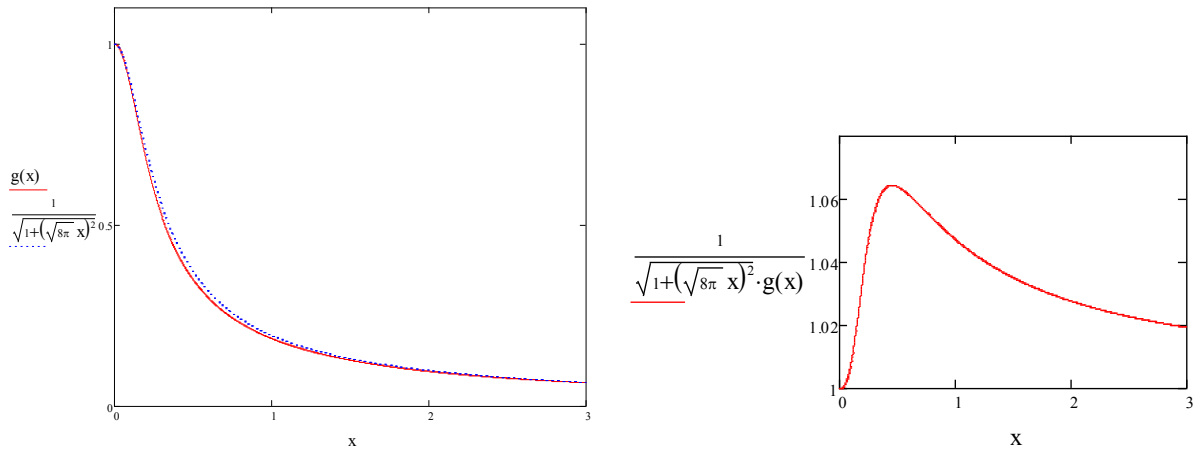

Figure 44. Exact integral and approximation for the brilliance of a bunch with an energy spread δ in an undulator. $x=kN\delta$, g(x) is the normalized numerically integrated brilliance. Right plot shows the ratio (relative error of the approximation).

9 Appendix B: Electron beam parameters in FSF injector

In this Appendix ASTRA input files and some results of the modeling of the FSF injector are given. We consider several operation modes and bunch charges respectively. First, the results for the low emittance mode with 15 pC bunch charge are given. Second, short bunch mode with 1 pC is considered. Third, 5 pC bunch with "intermediate" parameters will be shown.

9.1 Low emittance mode

9.1.1 Beam parameters at 19.5 m (inside the pre-injection linac)

In the following table beam parameters inside the pre-injector linac (at z=19.5 m from cathode) are summarized. At this point beam energy has reached ~50 MeV and space charge oscillations in the bunch are frozen ("emittance compensation" shall be achieved here).

Table 10: Beam parameters at the exit of the injector.

Parameter	Value
Beam momentum *pc*	50 MeV
Max average beam current	20 mA
Max bunch charge	15 pC
Longitudinal emittance (rms)	9 keV·mm
Bunch length (rms)	3 ps
Transversal normalized emittance (x/y, rms)	0.13/0.10 mm·mrad

Following subchapters describe the beam parameters in the injector in more details.

9.1.2 Particle distribution at the cathode

Table 11: Output of the ASTRA postprocessing program for the electron distribution at the cathode (flat top longitudinal profile).

```
100000 particles from file my1_4cell_2.ini
   Cathode located at:              z =      0.000     m
   Particles taken into account     N =     100000
   total charge                     Q =    -1.5000E-02 nC
   horizontal beam position         x =    -3.7656E-09 mm
   vertical beam position           y =    -7.6135E-09 mm
   longitudinal beam position       z =      0.000     m
   horizontal beam size         sig x =     0.1000     mm
   vertical beam size           sig y =     0.1000     mm
   longitudinal beam size       sig z =      0.000     mm
```

```
     total emission time              t =     7.1349E-02 ns
     rms emission time            sig t =     1.4611E-02 ns
     average kinetic energy           E =     3.1500E-07 MeV
     energy spread                   dE =     7.7477E-07 keV
     transverse beam emittance    eps x =     5.2962E-02 pi mrad mm
     correlated divergence        cor x =     5.2744E-05 mrad
     transverse beam emittance    eps y =     5.2962E-02 pi mrad mm
     correlated divergence        cor y =     4.0671E-05 mrad
     longitudinal beam emittance  eps z =      0.000     pi keV mm
     correlated energy spread     cor z =      0.000     keV
     emittance ratio eps y/eps x       =      1.000
     Reduced emittances:
     hor. emittance minus z correlation:     =     5.2962E-02 pi mrad mm
     hor. emittance minus z & E correlation: =     5.2847E-02 pi mrad mm
     ver. emittance minus z correlation:     =     5.2962E-02 pi mrad mm
     ver. emittance minus z & E correlation: =     3.8978E-02 pi mrad mm
```

Input file of the generator.exe

```
&INPUT
  FNAME = 'my1_4cell_2.ini'
  IPart=100000
  Species='electrons'
  Probe=.True.
  Noise_reduc=.True.
  Cathode=.True.
  Q_total=15.0E-3
  Ref_zpos=0.0
  Ref_clock=0.0E0
  Ref_Ekin=0.1E-6

  Dist_z='p'
  Lt=0.05
  rt=0.005

  Dist_pz='i'
  LE=0.215E-3

  Dist_x='r'
  sig_x=0.1
  Dist_px='g'

  Dist_y='r'
  sig_y=0.1
  Dist_py='g'
/
```

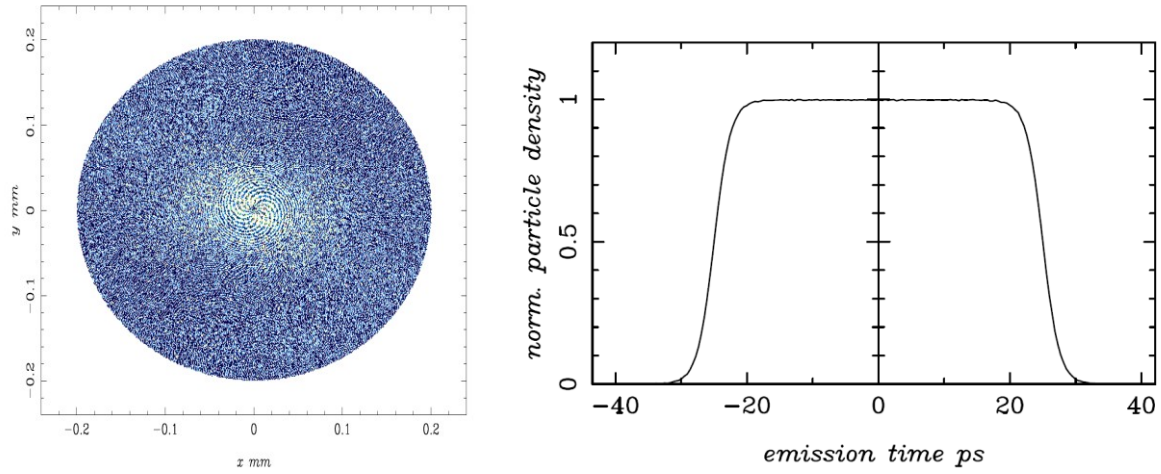

Figure 45. Laser spot at the cathode (left) and time profile of the laser (right) (flat top profile with 50 ps length and 5 ps rise/fall time).

9.1.3 Gun and booster section

Input file for the gun and booster modeling:

```
&NEWRUN
  Head='FSF-Injector 15.0pC, low emittance mode'
  RUN=2
  Loop=.f , NLoop=2
  Distribution = 'my1_4cell_2.ini',Xoff=0.0, Yoff=0.0
  Lmagnetized=.F
  EmitS=.T
  PhaseS=.T
  TrackS=.T
  RefS=.F
  Qbunch=15.0E-3
  TcheckS=.F
  CathodeS=.F
  TRACK_ALL=.T,   PHASE_SCAN=.F,    AUTO_PHASE=.T
  check_ref_part=.F
  ZSTART=0.0, ZSTOP=3.5
  Zemit=300
  Zphase=30
  H_max=0.001
  H_min=0.0001
 /

 &CHARGE
  LSPCH=.t
  Nrad=32, Nlong_in=64
  Cell_var=0.3
  min_grid=0.4D-6
  Max_scale=0.05
  Max_count=100
  Lmirror=.t
 /

&CAVITY
```

```
  LEFieLD=.t
  FILE_EFieLD(1)='Ez_1_4cell_cathode2_0mm.txt',          C_HIGHER_ORDER(1)=.t,
C_SMOOTH(1)=5,       Nue(1)=1.3,       MaxE(1)=-0.250000E+02,       Phi(1)=-9.0,
C_pos(1)=0.021926,

  FILE_EFieLD(2)='CBFp_sym.dat',      C_HIGHER_ORDER(2)=.t,      C_SMOOTH(2)=5,
Nue(2)=1.3, MaxE(2)=-23.500, Phi(2)=-0.0, C_pos(2)=0.073400E+01,

  FILE_EFieLD(3)='CBFp_sym.dat',      C_HIGHER_ORDER(3)=.t,      C_SMOOTH(3)=5,
Nue(3)=1.3, MaxE(3)=-25.000, Phi(3)=-3.0, C_pos(3)=0.152200E+01,

  FILE_EFieLD(4)='CBFp_sym.dat',      C_HIGHER_ORDER(4)=.t,      C_SMOOTH(4)=5,
Nue(4)=1.3, MaxE(4)=-30.0, Phi(4)=-3.0, C_pos(4)=0.238700E+01,

  FILE_EFieLD(5)='CBFp_3h_sym1.dat',    C_HIGHER_ORDER(5)=.t,    C_SMOOTH(5)=5,
Nue(5)=3.9, MaxE(5)=37.0, Phi(5)=180.0, C_pos(5)=0.317500E+01,
/
```

Table 12: Output of the ASTRA postprocessing program for the z=3.5

```
     FSF-Injector 15.0pC, low emittance mode
  100000 particles from file gun_booster.0350.002
     Particles taken into account      N =     100000
     total charge                      Q =    -1.5000E-02 nC
     horizontal beam position          x =    -2.6896E-05 mm
     vertical beam position            y =    -8.8459E-05 mm
     longitudinal beam position        z =      3.500     m
     horizontal beam size          sig x =      1.136     mm
     vertical beam size            sig y =      1.136     mm
     longitudinal beam size        sig z =      2.377     mm
     average kinetic energy            E =      9.449     MeV
     energy spread                    dE =      37.57     keV
     transverse beam emittance     eps x =     0.2177     pi mrad mm
     correlated divergence         cor x =    -0.6754     mrad
     transverse beam emittance     eps y =     0.2178     pi mrad mm
     correlated divergence         cor y =    -0.6754     mrad
     longitudinal beam emittance   eps z =      3.068     pi keV mm
     correlated energy spread      cor z =     -37.55     keV
     emittance ratio eps y/eps x         =     0.9992
     Reduced emittances:
     hor. emittance minus z correlation:     =     8.6216E-02 pi mrad mm
     hor. emittance minus z & E correlation: =     8.6211E-02 pi mrad mm
     ver. emittance minus z correlation:     =     8.6386E-02 pi mrad mm
     ver. emittance minus z & E correlation: =     8.6382E-02 pi mrad mm
```

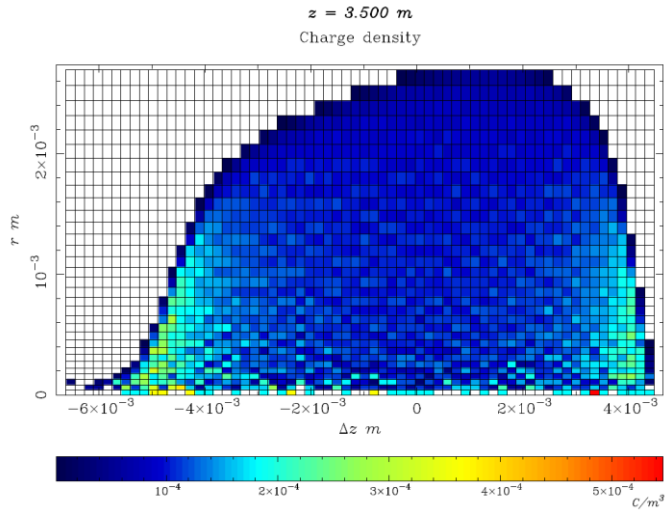

Figure 46. Charge density distribution at 3.5 m from the cathode. Small sizes of the bunch slices in the head and tail of the bunch require small radial mesh to resolve space charge fields. (Cell_var=0.3 is used in the "Charge" namelist of ASTRA to account for that.)

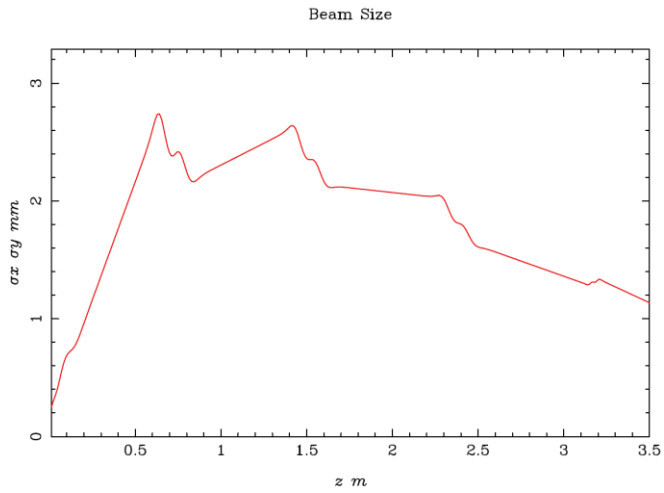

Figure 47. Transverse beam size in the gun/booster cryomodule.

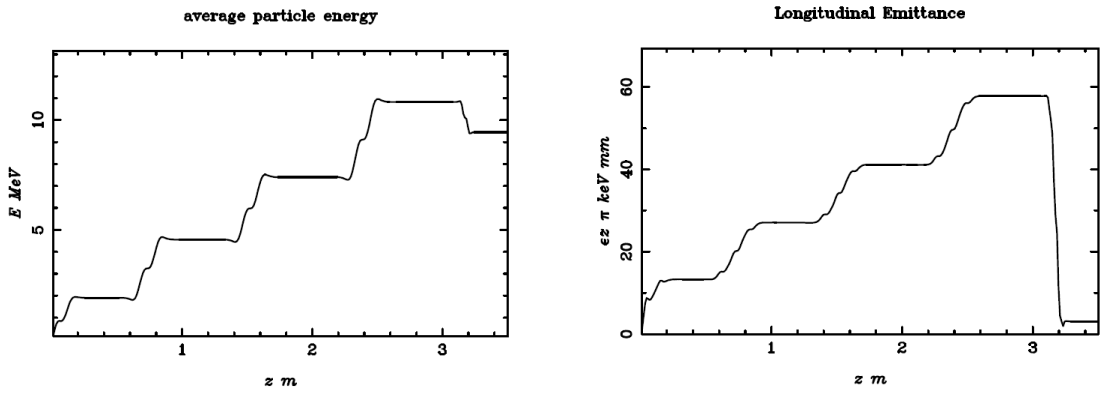

Figure 48. Average kinetic energy and longitudinal emittance in the FSF injector. 3rd harmonic cavity at ~3.2 m is used for the linearization of the longitudinal phase space.

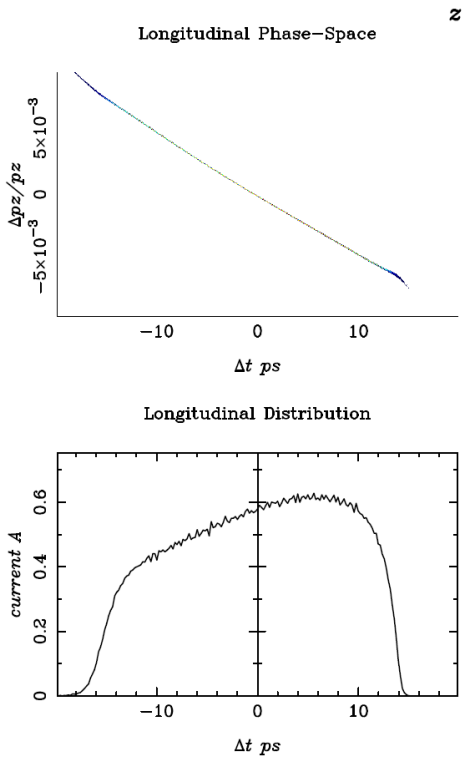

Figure 49. Longitudinal phase space (above) and current profile (below) at z=3.5 m. The correlated energy spread is imposed for further bunch compression in the merger section.

9.1.4 Merger section

Input file for the merger section:

```
&NEWRUN
  Version = 2
  Head='bypass 20deg, L= 110 cm, R56~33cm, offset D~50 cm'
  RUN=3
```

```
 Distribution = 'gun_booster.0350.002',Xoff=0.0, Yoff=0.0
 EmitS=.T
 PhaseS=.T
 TrackS=.T
 RefS=.F
 Qbunch=15.0E-3
 TcheckS=.F
 CathodeS=.F
 TRACK_ALL=.T,   PHASE_SCAN=.F,    AUTO_PHASE=.F
 check_ref_part=.F
 ZSTART=3.50, ZSTOP=11.9
 Zemit=300
 Zphase=30
 H_max=0.001
 H_min=0.0001
/

&CHARGE
 LSPCH=T
 LSPCH3D=T
 Nzf = 128
 Nz0 = 3
 Smooth_z = 1
 Nxf = 128
 Nx0 = 3
 Smooth_x = 1
 Nyf = 32
 Ny0 = 2
 Smooth_y = 1
 Max_scale=0.03
 Max_count=10
/

&QUADRUPOLE
 LQUAD=T

 Q_length(1)=0.15
 Q_grad(1)=0.020734293
 Q_bore(1)=0.04
 Q_pos(1)=3.95

 Q_length(2)=0.15
 Q_grad(2)=0.136052267
 Q_bore(2)=0.04
 Q_pos(2)=4.5

 Q_length(3)=0.15
 Q_grad(3)=0.058753387
 Q_bore(3)=0.04
 Q_pos(3)=5.05

 Q_length(4)=0.15
 Q_grad(4)=0.3598624
 Q_bore(4)=0.04
 Q_pos(4)=5.6

 Q_length(5)=0.15
```

```
 Q_grad(5)=0.0045
 Q_bore(5)=0.04
 Q_pos(5)=7.975
 Q_xoff(5)=0.506

 Q_length(6)=0.15
 Q_grad(6)=-0.006
 Q_bore(6)=0.04
 Q_pos(6)=9.725
 Q_xoff(6)=0.506
/

&DIPOLE
 LDipole=T

 D_Type(1) = horizontal
 D1(1)=(0.1,6.0),D2(1)=(-0.1,6.0),D3(1)=(0.1,6.3),D4(1)=(-0.1,6.3)
 D_radius(1) = -0.87714, D_Gap(1,1)=0.04, D_Gap(2,1)=0.04

 D_Type(2) = horizontal
 D1(2)=(0.6,7.4),D2(2)=(0.4,7.4),D3(2)=(0.6,7.7),D4(2)=(0.4,7.7)
 D_radius(2) = 0.87714, D_Gap(1,2)=0.04, D_Gap(2,2)=0.04

 D_Type(3) = horizontal
 D1(3)=(0.6,10.0),D2(3)=(0.4,10.0),D3(3)=(0.6,10.3),D4(3)=(0.4,10.3)
 D_radius(3) = 0.87714, D_Gap(1,3)=0.04, D_Gap(2,3)=0.04

 D_Type(4) = horizontal
 D1(4)=(0.1,11.4),D2(4)=(-0.1,11.4),D3(4)=(0.1,11.7),D4(4)=(-0.1,11.7)
 D_radius(4) = -0.87714, D_Gap(1,4)=0.04, D_Gap(2,4)=0.04
/
```

Table 13: Output of the ASTRA postprocessing program at z=11.9

```
    bypass 20deg, L= 110 cm, R56~33cm, offset D~50 cm
 100000 particles from file merger.1190.003
    Particles taken into account      N =     100000
    total charge                      Q =    -1.5000E-02 nC
    horizontal beam position          x =    -2.3883E-03 mm
    vertical beam position            y =     2.9209E-06 mm
    longitudinal beam position        z =      11.90     m
    horizontal beam size          sig x =     0.3152     mm
    vertical beam size            sig y =     5.7967E-02 mm
    longitudinal beam size        sig z =     0.9540     mm
    average kinetic energy            E =      9.449     MeV
    energy spread                    dE =      36.15     keV
    transverse beam emittance     eps x =     0.1852     pi mrad mm
    correlated divergence         cor x =     9.9086E-03 mrad
    transverse beam emittance     eps y =     0.1582     pi mrad mm
    correlated divergence         cor y =     0.1430     mrad
    longitudinal beam emittance   eps z =      3.410     pi keV mm
    correlated energy spread      cor z =     -35.98     keV
    emittance ratio eps y/eps x         =      1.171
    Reduced emittances:
    hor. emittance minus z correlation:     =     0.1547     pi mrad mm
    hor. emittance minus z & E correlation: =     0.1547     pi mrad mm
    ver. emittance minus z correlation:     =     8.6354E-02 pi mrad mm
```

```
     ver. emittance minus z & E correlation: =      8.5954E-02 pi mrad mm
```

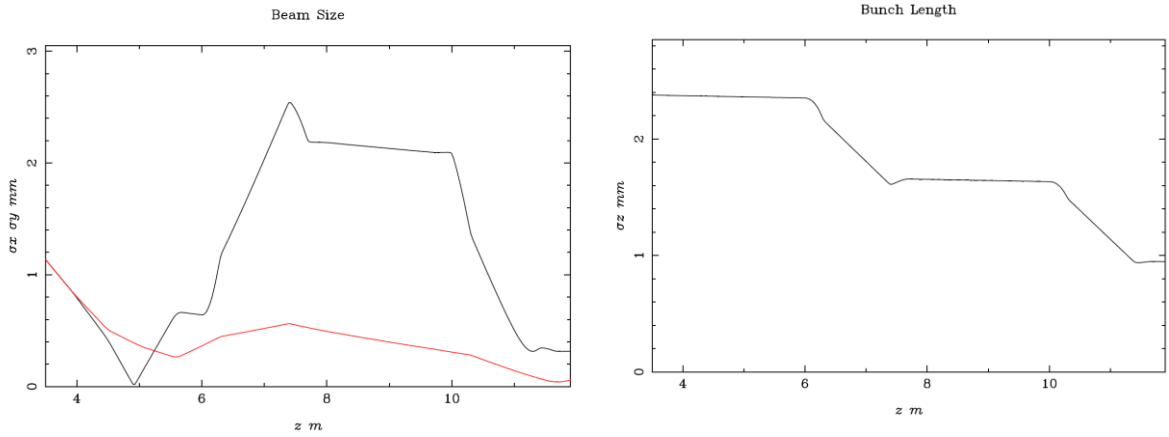

Figure 50. Transverse beam sizes (left, black curve – horizontal (x), red – vertical (y)) and bunch length (right) in the merger section. High energy spread in the merger dominates the horizontal beam size between merger dipoles (6 to 11 m from the cathode).

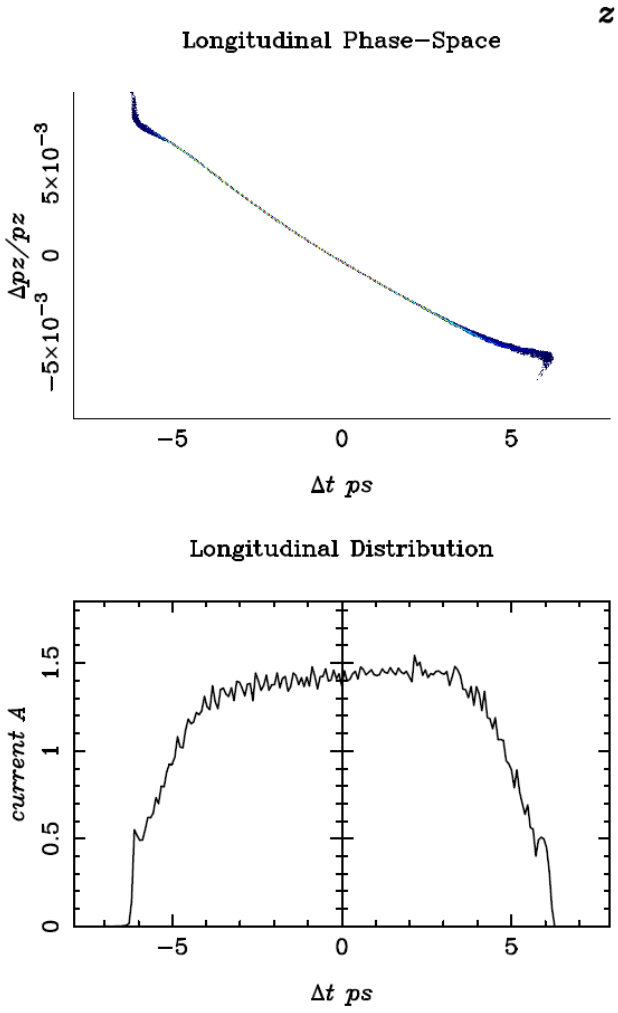

Figure 51. Longitudinal phase space (above) and current profile (below) at z=11.9 m (behind the merger section). The bunch is compressed to the rms length of ~3 ps. Quite flat peak current profile in the bunch is reached by adjusting the amplitude of the 3rd harmonic cavity.

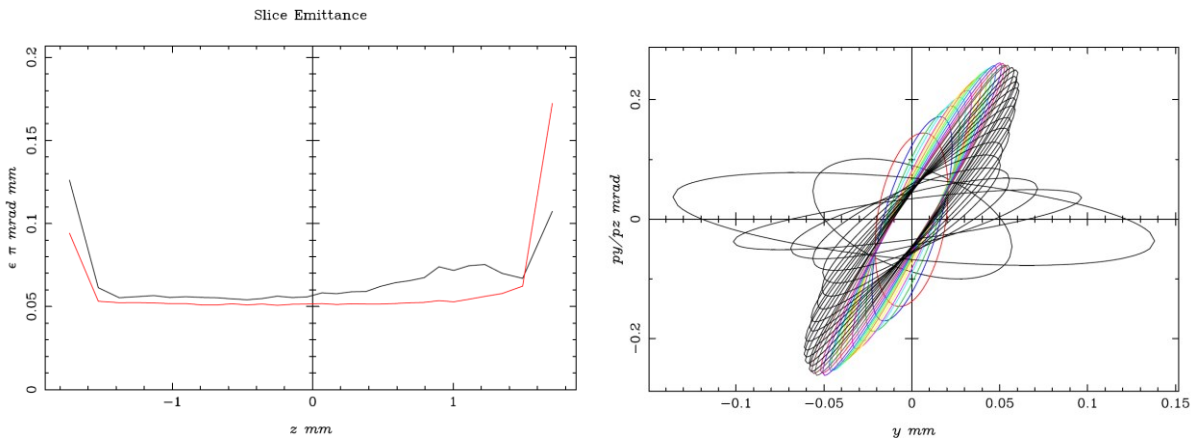

Figure 52. Left: slice emittances at z=11.9 m (behind the merger section). Right: phase space ellipses for the slices. The emittances of 30 slices are plotted. Black curve on the left picture – horizontal normalized emittance, red – vertical. The slice emittances are nearly preserved in the merger section. Right picture shows the "rotation" of the phase space ellipses of the slices (vertical plane), demonstrating the cause for the projected emittance growth. "Emittance compensation" is possible and will reduce the projected emittance downstream the beam line. Also, the head and tail slices demonstrate higher slice emittance and deviating Twiss parameters. This is due to the low charge density in the slice.

9.1.5 Linac section

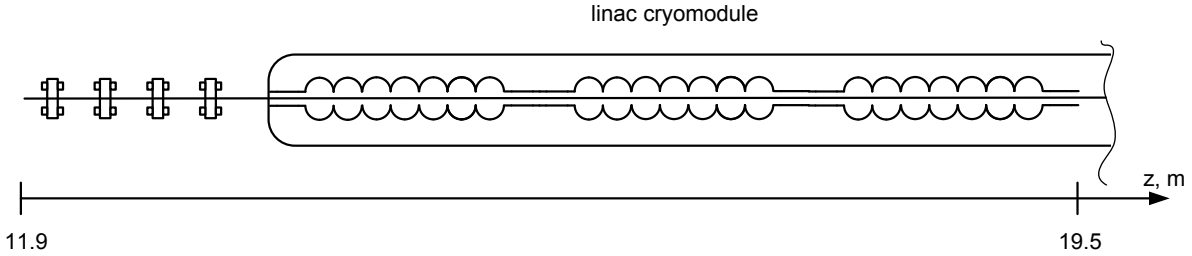

Figure 53. Sketch of the part of pre-injector linac used in ASTRA modeling for "emittance compensation".

Input file for the linac section:

```
&NEWRUN
  Version = 2
  Head='linac'
  RUN=3
  Distribution = 'merger.1190.003',Xoff=0.0, Yoff=0.0
  EmitS=.T
  PhaseS=.T
  TrackS=.T
  RefS=.F
  TcheckS=.F
  CathodeS=.F
  TRACK_ALL=.T,   PHASE_SCAN=.F,    AUTO_PHASE=.T
  check_ref_part=.F
```

```
  ZSTART=11.90, ZSTOP=19.5
  Zemit=300
  Zphase=30
  H_max=0.001
  H_min=0.0001
 /

 &CHARGE
  LSPCH=T
  LSPCH3D=T
  Nzf = 128
  Nz0 = 3
  Smooth_z = 1
  Nxf = 64
  Nx0 = 3
  Smooth_x = 1
  Nyf = 64
  Ny0 = 3
  Smooth_y = 1
  Max_scale=0.03
  Max_count=10
 /

&CAVITY

  Loop=.f
  LEFieLD=.t

FILE_EFieLD(1)='ref_7cell_centered.dat',C_HIGHER_ORDER(1)=.t,C_SMOOTH(1)=5,Nu
e(1)=1.3, MaxE(1)=-35.1, Phi(1)=10.0, C_pos(1)=15.394,

FILE_EFieLD(2)='ref_7cell_centered.dat',C_HIGHER_ORDER(2)=.t,C_SMOOTH(2)=5,Nu
e(2)=1.3, MaxE(2)=-35.1, Phi(2)=10.0, C_pos(2)=16.782,

FILE_EFieLD(3)='ref_7cell_centered.dat',C_HIGHER_ORDER(3)=.t,C_SMOOTH(3)=5,Nu
e(3)=1.3, MaxE(3)=-35.1, Phi(3)=10.0, C_pos(3)=18.17,
 /

 &QUADRUPOLE
  LQUAD=T

  Q_length(1)=0.15
  Q_grad(1)=0.0
  Q_bore(1)=0.04
  Q_pos(1)=3.95

  Q_length(2)=0.15
  Q_grad(2)=0.0
  Q_bore(2)=0.04
  Q_pos(2)=4.5

  Q_length(3)=0.15
  Q_grad(3)=-0.0
  Q_bore(3)=0.04
  Q_pos(3)=5.05

  Q_length(4)=0.15
```

```
Q_grad(4)=0.0
Q_bore(4)=0.04
Q_pos(4)=5.6

Q_length(5)=0.15
Q_grad(5)=0.230744533
Q_bore(5)=0.04
Q_pos(5)=12.15

Q_length(6)=0.15
Q_grad(6)=-0.437197867
Q_bore(6)=0.04
Q_pos(6)=12.7

Q_length(7)=0.15
Q_grad(7)=0.09250624
Q_bore(7)=0.04
Q_pos(7)=13.25

Q_length(8)=0.15
Q_grad(8)=0.084497387
Q_bore(8)=0.04
Q_pos(8)=13.8/
```

Table 14: Output of the ASTRA postprocessing program at z=19.5 m.

```
   linac
100000 particles from file linac.1950.003
   Particles taken into account      N =     100000
   total charge                      Q =    -1.5000E-02 nC
   horizontal beam position          x =     6.4841E-04 mm
   vertical beam position            y =    -5.8899E-06 mm
   longitudinal beam position        z =      19.50     m
   horizontal beam size          sig x =     7.3836E-02 mm
   vertical beam size            sig y =     8.5279E-02 mm
   longitudinal beam size        sig z =     0.9254     mm
   average kinetic energy            E =      52.74     MeV
   energy spread                    dE =      155.7     keV
   transverse beam emittance     eps x =     0.1330     pi mrad mm
   correlated divergence         cor x =     2.0528E-02 mrad
   transverse beam emittance     eps y =     9.2931E-02 pi mrad mm
   correlated divergence         cor y =     2.7263E-03 mrad
   longitudinal beam emittance   eps z =      9.057     pi keV mm
   correlated energy spread      cor z =      155.4     keV
   emittance ratio eps y/eps x         =      1.432
   Reduced emittances:
   hor. emittance minus z correlation:     =     0.1274     pi mrad mm
   hor. emittance minus z & E correlation: =     0.1274     pi mrad mm
   ver. emittance minus z correlation:     =     8.8447E-02 pi mrad mm
   ver. emittance minus z & E correlation: =     8.8376E-02 pi mrad mm
```

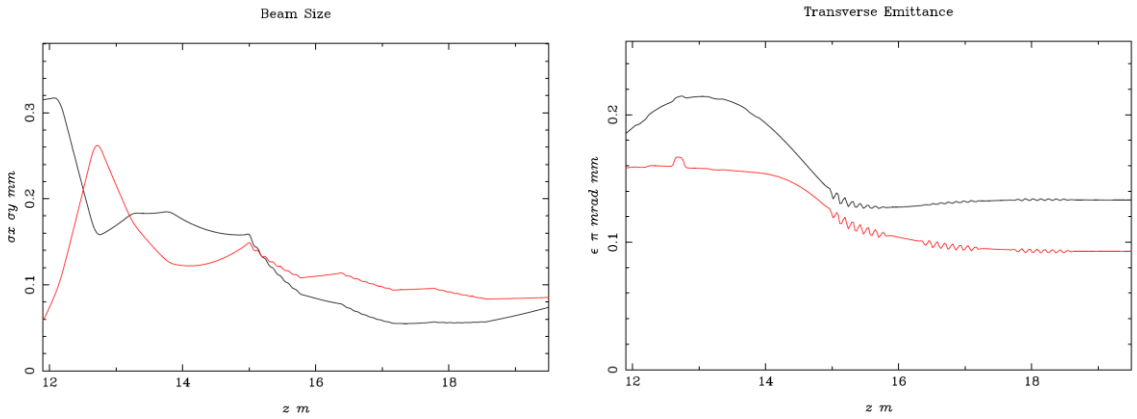

Figure 54. Transverse beam sizes (left) and projected emittances (right) in the linac section. Last stage of the "emittance compensation" can be seen.

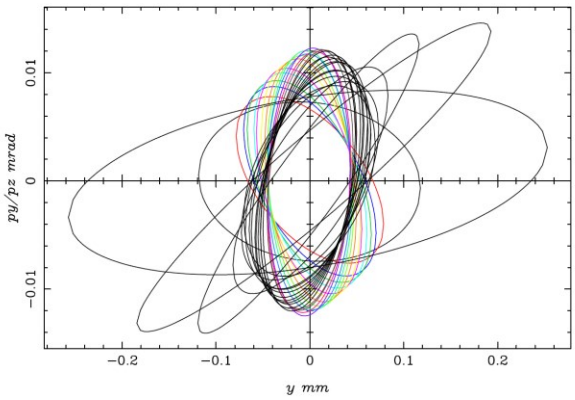

Figure 55. Phase space ellipses overlap in the vertical plane behind the linac ("emittance compensation point"). This picture is to compare with the ellipses in Figure 52.

9.2 Short bunch mode, 1 pC bunch

9.2.1 Beam parameters at 19.5 m (inside the pre-injection linac)

Table 15: Beam parameters at the exit of the injector.

Parameter	Value
Beam momentum *pc*	50 MeV
Max average beam current	1.3 mA
Max bunch charge	1 pC
Longitudinal emittance (rms)	0.75 keV·mm
Bunch length (rms)	0.62 ps
Transversal normalized emittance (x/y, rms)	0.18/0.08 mm·mrad

9.2.2 Particle distribution at the cathode

The same cathode laser parameters as for the low emittance mode are assumed with lower laser power (1 pC bunch charge).

9.2.3 Gun and booster section

Gun and booster settings are essentially the same as in the low emittance mode. The phases of the 2nd and 3rd booster cavities are adjusted to provide the necessary energy chirp for stronger compression in the merger section. The amplitude of the 3rd harmonic cavity is adjusted to minimize the longitudinal emittance for the low charge bunch.

Input file for the gun and booster modeling:

```
&NEWRUN
  Head='FSF-Injector 1.0pC, short bunch mode'
  RUN=2
  Loop=.f , NLoop=2
  Distribution = 'my1_4cell_2.ini',Xoff=0.0, Yoff=0.0
  Lmagnetized=.F
  EmitS=.T
  PhaseS=.T
  TrackS=.T
  RefS=.F
!  Qbunch=1.0E-3
  TcheckS=.F
```

```
  CathodeS=.F
  TRACK_ALL=.T,   PHASE_SCAN=.F,    AUTO_PHASE=.T
  check_ref_part=.F
  ZSTART=0.0, ZSTOP=3.5
  Zemit=300
  Zphase=30
  H_max=0.001
  H_min=0.0001
 /

 &CHARGE
  LSPCH=.t
  Nrad=32, Nlong_in=64

  Cell_var=0.3
  min_grid=0.4D-6
  Max_scale=0.05
  Max_count=100
  Lmirror=.t
 /

&CAVITY
  LEFieLD=.t
  FILE_EFieLD(1)='Ez_1_4cell_cathode2_0mm.txt',          C_HIGHER_ORDER(1)=.t,
C_SMOOTH(1)=5,      Nue(1)=1.3,      MaxE(1)=-0.250000E+02,      Phi(1)=-9.0,
C_pos(1)=0.021926,

  FILE_EFieLD(2)='CBFp_sym.dat',      C_HIGHER_ORDER(2)=.t,      C_SMOOTH(2)=5,
Nue(2)=1.3, MaxE(2)=-23.500, Phi(2)=-0.0, C_pos(2)=0.073400E+01,

  FILE_EFieLD(3)='CBFp_sym.dat',      C_HIGHER_ORDER(3)=.t,      C_SMOOTH(3)=5,
Nue(3)=1.3, MaxE(3)=-25.000, Phi(3)=-5.5, C_pos(3)=0.152200E+01,

  FILE_EFieLD(4)='CBFp_sym.dat',      C_HIGHER_ORDER(4)=.t,      C_SMOOTH(4)=5,
Nue(4)=1.3, MaxE(4)=-30.0, Phi(4)=-5.5, C_pos(4)=0.238700E+01,

  FILE_EFieLD(5)='CBFp_3h_sym1.dat',    C_HIGHER_ORDER(5)=.t,    C_SMOOTH(5)=5,
Nue(5)=3.9, MaxE(5)=36.0, Phi(5)=180.0, C_pos(5)=0.317500E+01,
 /
```

Table 16: Output of the ASTRA postprocessing program for the z=3.5

```
     FSF-Injector 1.0pC, short bunch mode
  100000 particles from file gun_booster.0350.002
     Particles taken into account      N =     100000
     total charge                      Q =    -9.9998E-04 nC
     horizontal beam position          x =    -2.1585E-06 mm
     vertical beam position            y =    -6.8384E-07 mm
     longitudinal beam position        z =      3.500     m
     horizontal beam size          sig x =     0.1157     mm
```

```
vertical beam size              sig y =     0.1157      mm
longitudinal beam size          sig z =      2.176      mm
average kinetic energy              E =      9.460      MeV
energy spread                      dE =      51.02      keV
transverse beam emittance       eps x =     5.5984E-02 pi mrad mm
correlated divergence           cor x =    -7.4838E-02 mrad
transverse beam emittance       eps y =     5.5984E-02 pi mrad mm
correlated divergence           cor y =    -7.4831E-02 mrad
longitudinal beam emittance     eps z =     0.9961     pi keV mm
correlated energy spread        cor z =     -51.02     keV
emittance ratio eps y/eps x             =      1.000
Reduced emittances:
hor. emittance minus z correlation:     =     5.5381E-02 pi mrad mm
hor. emittance minus z & E correlation: =     5.5381E-02 pi mrad mm
ver. emittance minus z correlation:     =     5.5384E-02 pi mrad mm
ver. emittance minus z & E correlation: =     5.5384E-02 pi mrad mm
```

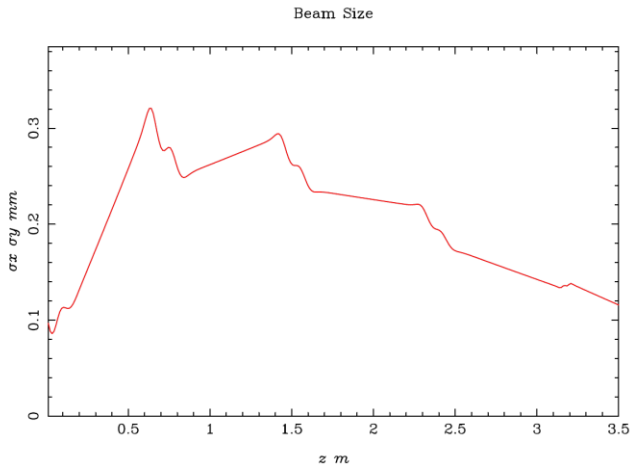

Figure 56. Transverse beam size in the gun/booster cryomodule.

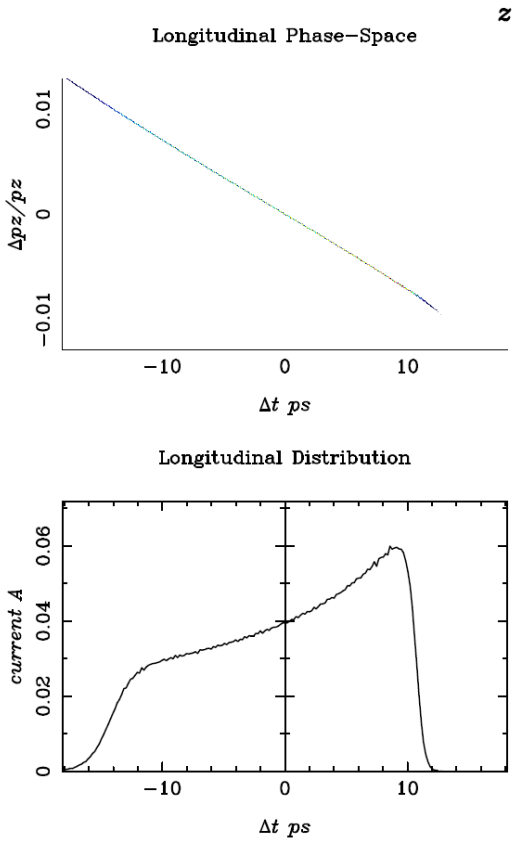

Figure 57. Longitudinal phase space (above) and current profile (below) at z=3.5 m. The correlated energy spread is imposed for further bunch compression in the merger section.

9.2.4 Merger section

Input file for the merger section:

```
&NEWRUN
  Version = 2
  Head='bypass 20deg, L= 110 cm, R56~33cm, offset D~50 cm'
  RUN=2
  Distribution = 'gun_booster.0350.002',Xoff=0.0, Yoff=0.0
  EmitS=.T
  PhaseS=.T
  TrackS=.T
  RefS=.F
!  Qbunch=1.0E-3
  TcheckS=.F
  CathodeS=.F
  TRACK_ALL=.T,   PHASE_SCAN=.F,    AUTO_PHASE=.F
  check_ref_part=.F
  ZSTART=3.50, ZSTOP=11.9
  Zemit=300
  Zphase=30
  H_max=0.001
  H_min=0.0001
 /
```

```
&CHARGE
 LSPCH=T
 LSPCH3D=T
 Nzf = 128
 Nz0 = 3
 Smooth_z = 1
 Nxf = 128
 Nx0 = 3
 Smooth_x = 1
 Nyf = 32
 Ny0 = 2
 Smooth_y = 1
 Max_scale=0.03
 Max_count=10
/

&QUADRUPOLE
 LQUAD=T

 Q_length(1)=0.15
 Q_grad(1)=0.0929277
 Q_bore(1)=0.04
 Q_pos(1)=3.95

 Q_length(2)=0.15
 Q_grad(2)=-0.0502569
 Q_bore(2)=0.04
 Q_pos(2)=4.5

 Q_length(3)=0.15
 Q_grad(3)=0.163916
 Q_bore(3)=0.04
 Q_pos(3)=5.05

 Q_length(4)=0.15
 Q_grad(4)=0.285505
 Q_bore(4)=0.04
 Q_pos(4)=5.6
/

&DIPOLE
 LDipole=T

 D_Type(1) = horizontal
 D1(1)=(0.1,6.0),D2(1)=(-0.1,6.0),D3(1)=(0.1,6.3),D4(1)=(-0.1,6.3)
 D_radius(1) = -0.87714, D_Gap(1,1)=0.04, D_Gap(2,1)=0.04

 D_Type(2) = horizontal
 D1(2)=(0.6,7.4),D2(2)=(0.4,7.4),D3(2)=(0.6,7.7),D4(2)=(0.4,7.7)
 D_radius(2) = 0.87714, D_Gap(1,2)=0.04, D_Gap(2,2)=0.04

 D_Type(3) = horizontal
 D1(3)=(0.6,10.0),D2(3)=(0.4,10.0),D3(3)=(0.6,10.3),D4(3)=(0.4,10.3)
 D_radius(3) = 0.87714, D_Gap(1,3)=0.04, D_Gap(2,3)=0.04

 D_Type(4) = horizontal
```

```
 D1(4)=(0.1,11.4),D2(4)=(-0.1,11.4),D3(4)=(0.1,11.7),D4(4)=(-0.1,11.7)
 D_radius(4) = -0.87714, D_Gap(1,4)=0.04, D_Gap(2,4)=0.04
/
```

Table 17: Output of the ASTRA postprocessing program at z=11.9

```
   bypass 20deg, L= 110 cm, R56~33cm, offset D~50 cm
100000 particles from file merger.1190.002
   Particles taken into account      N =     100000
   total charge                      Q =   -9.9997E-04 nC
   horizontal beam position          x =    6.5281E-04 mm
   vertical beam position            y =    1.5940E-06 mm
   longitudinal beam position        z =     11.90     m
   horizontal beam size          sig x =    0.2892     mm
   vertical beam size            sig y =    4.2966E-02 mm
   longitudinal beam size        sig z =    0.2168     mm
   average kinetic energy            E =     9.460     MeV
   energy spread                    dE =     50.48     keV
   transverse beam emittance     eps x =    0.1221     pi mrad mm
   correlated divergence         cor x =    7.2102E-02 mrad
   transverse beam emittance     eps y =    6.0732E-02 pi mrad mm
   correlated divergence         cor y =   -0.1120     mrad
   longitudinal beam emittance   eps z =    0.9892     pi keV mm
   correlated energy spread      cor z =    -50.28     keV
   emittance ratio eps y/eps x       =     2.010
   Reduced emittances:
   hor. emittance minus z correlation:     =    9.0518E-02 pi mrad mm
   hor. emittance minus z & E correlation: =    9.0232E-02 pi mrad mm
   ver. emittance minus z correlation:     =    5.5468E-02 pi mrad mm
   ver. emittance minus z & E correlation: =    5.5456E-02 pi mrad mm
```

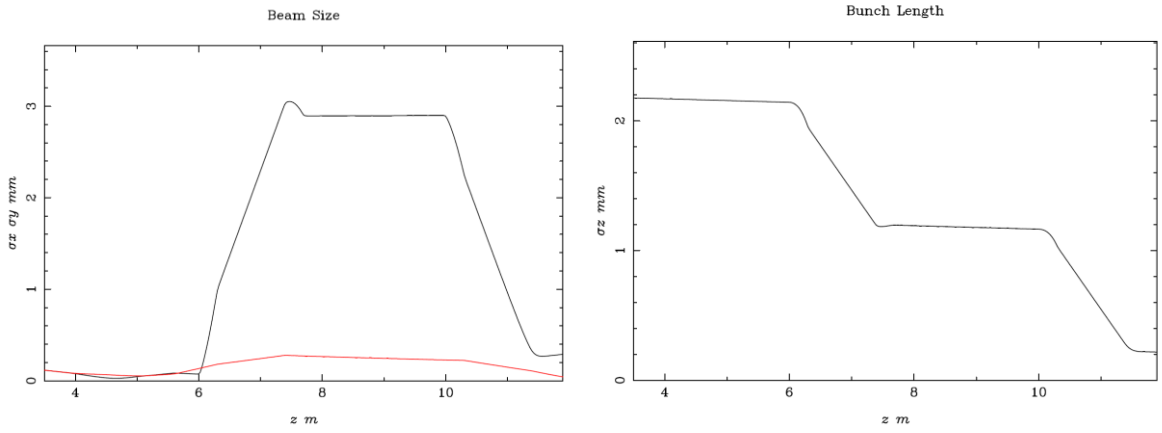

Figure 58. Transverse beam sizes (left, black curve – horizontal (x), red – vertical (y)) and bunch length (right) in the merger section. High energy spread in the merger dominates the horizontal beam size between merger dipoles (6 to 11 m from the cathode). Bunch compression down to 0.2 mm longitudinal size is possible with 1 pC.

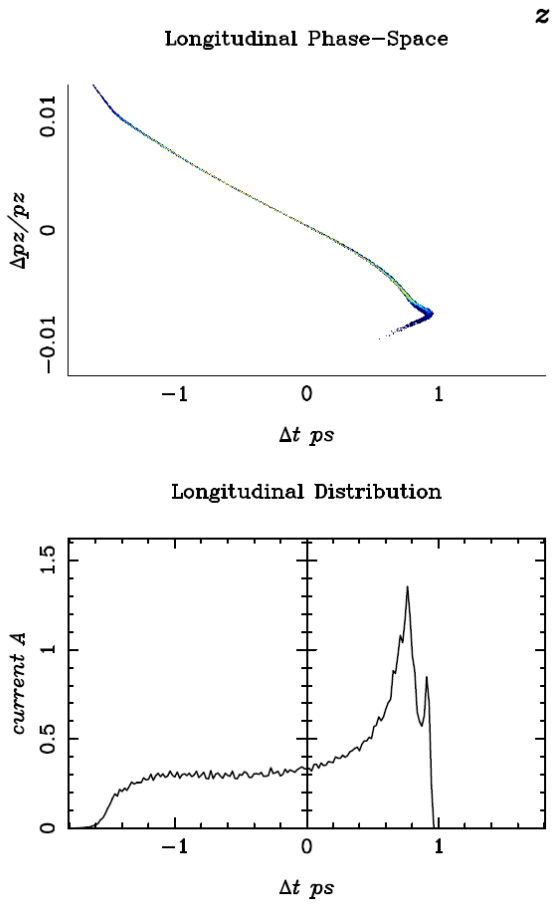

Figure 59. Longitudinal phase space (above) and current profile (below) at z=11.9 m (behind the merger section). The bunch is compressed to the rms length of ~0.6 ps. Peak current is limited to ca. the same value (1.5 A) as for the low emittance mode to avoid large emittance growth.

9.2.5 Linac section

Input file for the linac section:

```
&NEWRUN
  Version = 2
  Head='linac'
  RUN=2
  Distribution = 'merger.1190.002',Xoff=0.0, Yoff=0.0
  EmitS=.T
  PhaseS=.T
  TrackS=.T
  RefS=.F
!  Qbunch=1E-3
  TcheckS=.F
  CathodeS=.F
  TRACK_ALL=.T,   PHASE_SCAN=.F,    AUTO_PHASE=.T
  check_ref_part=.F
```

```
  ZSTART=11.90, ZSTOP=19.5
  Zemit=300
  Zphase=30
  H_max=0.001
  H_min=0.0001
 /

&CHARGE
  LSPCH=T
  LSPCH3D=T
  Nzf = 128
  Nz0 = 3
  Smooth_z = 1
  Nxf = 64
  Nx0 = 3
  Smooth_x = 1
  Nyf = 64
  Ny0 = 3
  Smooth_y = 1
  Max_scale=0.03
  Max_count=10
 /

&CAVITY

  Loop=.f
  LEFieLD=.t

FILE_EFieLD(1)='ref_7cell_centered.dat',C_HIGHER_ORDER(1)=.t,C_SMOOTH(1)=5,Nu
e(1)=1.3, MaxE(1)=-35.1, Phi(1)=1.0, C_pos(1)=15.394,

FILE_EFieLD(2)='ref_7cell_centered.dat',C_HIGHER_ORDER(2)=.t,C_SMOOTH(2)=5,Nu
e(2)=1.3, MaxE(2)=-35.1, Phi(2)=1.0, C_pos(2)=16.782,

FILE_EFieLD(3)='ref_7cell_centered.dat',C_HIGHER_ORDER(3)=.t,C_SMOOTH(3)=5,Nu
e(3)=1.3, MaxE(3)=-35.1, Phi(3)=1.0, C_pos(3)=18.17,
/
 &QUADRUPOLE
  LQUAD=T

  Q_length(1)=0.15
  Q_grad(1)=0.0929277
  Q_bore(1)=0.04
  Q_pos(1)=3.95

  Q_length(2)=0.15
  Q_grad(2)=-0.0502569
  Q_bore(2)=0.04
  Q_pos(2)=4.5
```

```
  Q_length(3)=0.15
  Q_grad(3)=0.163916
  Q_bore(3)=0.04
  Q_pos(3)=5.05

  Q_length(4)=0.15
  Q_grad(4)=0.285505
  Q_bore(4)=0.04
  Q_pos(4)=5.6

  Q_length(5)=0.15
  Q_grad(5)=0.204
  Q_bore(5)=0.04
  Q_pos(5)=12.15

  Q_length(6)=0.15
  Q_grad(6)=-0.402634
  Q_bore(6)=0.04
  Q_pos(6)=12.7

  Q_length(7)=0.15
  Q_grad(7)=0.18186
  Q_bore(7)=0.04
  Q_pos(7)=13.25

  Q_length(8)=0.15
  Q_grad(8)=-0.0333541
  Q_bore(8)=0.04
  Q_pos(8)=13.8
/
```

Table 18: Output of the ASTRA postprocessing program at z=19.5 m.

```
     linac
  100000 particles from file linac.1950.002
     Particles taken into account      N =     100000
     total charge                      Q =    -9.9996E-04 nC
     horizontal beam position          x =     1.4997E-05 mm
     vertical beam position            y =    -4.2019E-06 mm
     longitudinal beam position        z =      19.50     m
     horizontal beam size          sig x =     7.5986E-02 mm
     vertical beam size            sig y =     6.9683E-02 mm
     longitudinal beam size        sig z =     0.1724     mm
     average kinetic energy            E =      53.40     MeV
     energy spread                    dE =      44.54     keV
     transverse beam emittance     eps x =     0.1904     pi mrad mm
     correlated divergence         cor x =     4.1202E-02 mrad
     transverse beam emittance     eps y =     8.0352E-02 pi mrad mm
     correlated divergence         cor y =    -1.1770E-02 mrad
```

```
longitudinal beam emittance   eps z =     0.7509     pi keV mm
correlated energy spread      cor z =     -44.33     keV
emittance ratio eps y/eps x         =      2.370
Reduced emittances:
hor. emittance minus z correlation:     =     0.1669     pi mrad mm
hor. emittance minus z & E correlation: =     0.1669     pi mrad mm
ver. emittance minus z correlation:     =     6.5429E-02 pi mrad mm
ver. emittance minus z & E correlation: =     6.5415E-02 pi mrad mm
```

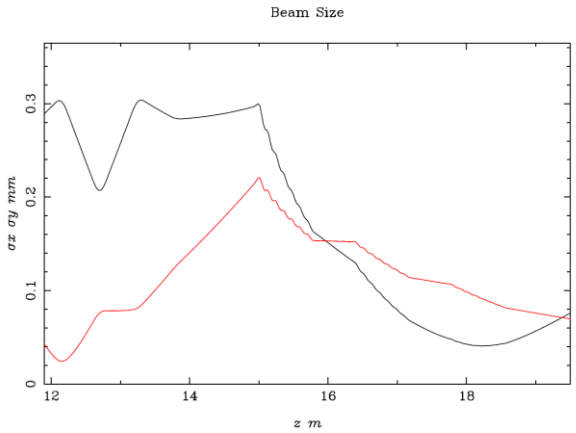

Figure 60. Transverse beam sizes in the linac section.

9.3 Short bunch mode, 5 pC bunch

9.3.1 Beam parameters at 19.5 m (inside the pre-injection linac)

Table 19: Beam parameters at the exit of the injector.

Parameter	Value
Beam momentum *pc*	50 MeV
Max average beam current	6.5 mA
Max bunch charge	5 pC
Longitudinal emittance (rms)	2.5 keV·mm
Bunch length (rms)	2 ps
Transversal normalized emittance (x/y, rms)	0.11/0.06 mm·mrad

9.3.2 Particle distribution at the cathode

The same cathode laser parameters as for the low emittance mode are assumed with lower laser power (5 pC bunch charge).

9.3.3 Gun and booster section

Gun and booster settings are essentially the same as in the low emittance mode. The phases of the 2nd and 3rd booster cavities are adjusted to provide the necessary energy chirp for a little bit stronger compression in the merger section.

Input file for the gun and booster modeling:

```
&NEWRUN
  Head='FSF-Injector 5.0pC, short bunch mode'
  RUN=2
  Loop=.f , NLoop=2
  Distribution = 'my1_4cell_2.ini',Xoff=0.0, Yoff=0.0
  Lmagnetized=.F
  EmitS=.T
  PhaseS=.T
  TrackS=.T
  RefS=.F
!  Qbunch=5.0E-3
  TcheckS=.F
  CathodeS=.F
  TRACK_ALL=.T,   PHASE_SCAN=.F,    AUTO_PHASE=.T
```

```
  check_ref_part=.F
  ZSTART=0.0, ZSTOP=3.5
  Zemit=300
  Zphase=30
  H_max=0.001
  H_min=0.0001
 /

 &CHARGE
  LSPCH=.t
  Nrad=32, Nlong_in=64
  Cell_var=0.3
  min_grid=0.4D-6
  Max_scale=0.05
  Max_count=100
  Lmirror=.t
 /

&CAVITY
  LEFieLD=.t
  FILE_EFieLD(1)='Ez_1_4cell_cathode2_0mm.txt',          C_HIGHER_ORDER(1)=.t,
C_SMOOTH(1)=5,       Nue(1)=1.3,       MaxE(1)=-0.250000E+02,       Phi(1)=-9.0,
C_pos(1)=0.021926,

  FILE_EFieLD(2)='CBFp_sym.dat',      C_HIGHER_ORDER(2)=.t,      C_SMOOTH(2)=5,
Nue(2)=1.3, MaxE(2)=-23.500, Phi(2)=-0.0, C_pos(2)=0.073400E+01,

  FILE_EFieLD(3)='CBFp_sym.dat',      C_HIGHER_ORDER(3)=.t,      C_SMOOTH(3)=5,
Nue(3)=1.3, MaxE(3)=-25.000, Phi(3)=-4.0, C_pos(3)=0.152200E+01,

  FILE_EFieLD(4)='CBFp_sym.dat',      C_HIGHER_ORDER(4)=.t,      C_SMOOTH(4)=5,
Nue(4)=1.3, MaxE(4)=-30.0, Phi(4)=-4.0, C_pos(4)=0.238700E+01,

  FILE_EFieLD(5)='CBFp_3h_sym1.dat',    C_HIGHER_ORDER(5)=.t,    C_SMOOTH(5)=5,
Nue(5)=3.9, MaxE(5)=36.0, Phi(5)=180.0, C_pos(5)=0.317500E+01,
 /
```

Table 20: Output of the ASTRA postprocessing program for the z=3.5

```
     FSF-Injector 5.0pC, short bunch mode
  100000 particles from file gun_booster.0350.002
     Particles taken into account      N =     100000
     total charge                      Q =    -4.9998E-03 nC
     horizontal beam position          x =    -1.0224E-05 mm
     vertical beam position            y =    -1.8600E-05 mm
     longitudinal beam position        z =      3.500     m
     horizontal beam size          sig x =     0.4630     mm
     vertical beam size            sig y =     0.4630     mm
     longitudinal beam size        sig z =      2.227     mm
     average kinetic energy            E =      9.474     MeV
```

```
energy spread                    dE =      41.71     keV
transverse beam emittance     eps x =     7.0658E-02 pi mrad mm
correlated divergence         cor x =    -0.2805     mrad
transverse beam emittance     eps y =     7.0734E-02 pi mrad mm
correlated divergence         cor y =    -0.2804     mrad
longitudinal beam emittance   eps z =     0.9186     pi keV mm
correlated energy spread      cor z =     -41.71     keV
emittance ratio eps y/eps x          =     0.9989
Reduced emittances:
hor. emittance minus z correlation:     =     6.6096E-02 pi mrad mm
hor. emittance minus z & E correlation: =     6.6096E-02 pi mrad mm
ver. emittance minus z correlation:     =     6.6150E-02 pi mrad mm
ver. emittance minus z & E correlation: =     6.6150E-02 pi mrad mm
```

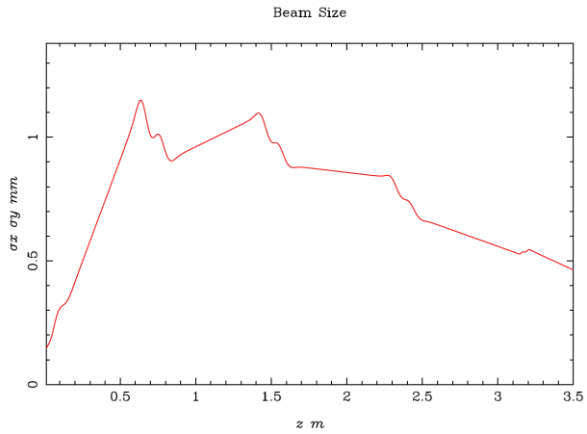

Figure 61. Transverse beam size in the gun/booster cryomodule.

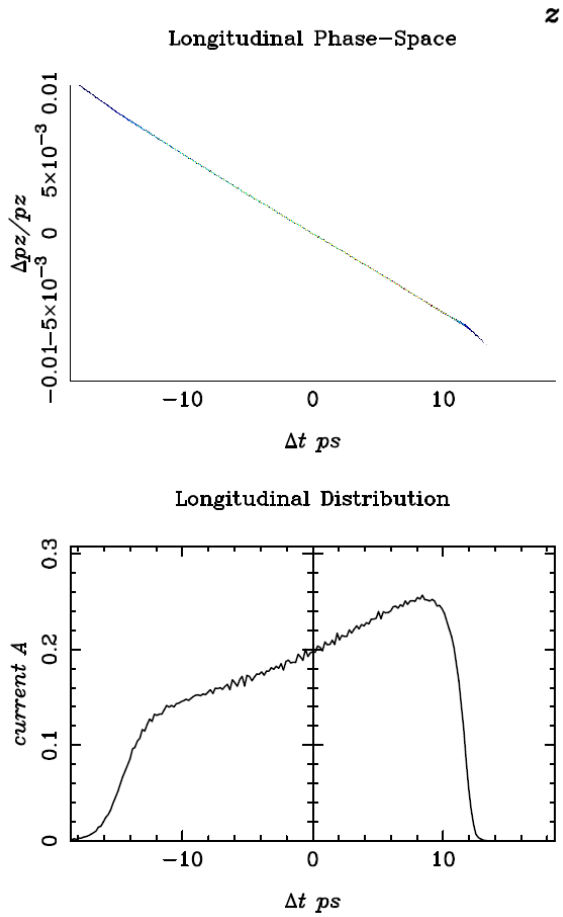

Figure 62. Longitudinal phase space (above) and current profile (below) at z=3.5 m. The correlated energy spread is imposed for further bunch compression in the merger section.

9.3.4 Merger section

Input file for the merger section:

```
&NEWRUN
  Version = 2
  Head='bypass 20deg, L= 110 cm, R56~33cm, offset D~50 cm'
  RUN=2
  Distribution = 'gun_booster.0350.002',Xoff=0.0, Yoff=0.0
  EmitS=.T
  PhaseS=.T
  TrackS=.T
  RefS=.F
!  Qbunch=5.0E-3
  TcheckS=.F
  CathodeS=.F
  TRACK_ALL=.T,   PHASE_SCAN=.F,    AUTO_PHASE=.F
  check_ref_part=.F
  ZSTART=3.50, ZSTOP=11.9
```

```
  Zemit=300
  Zphase=30
  H_max=0.001
  H_min=0.0001
 /
 &CHARGE
  LSPCH=T
  LSPCH3D=T
  Nzf = 128
  Nz0 = 3
  Smooth_z = 1
  Nxf = 128
  Nx0 = 3
  Smooth_x = 1
  Nyf = 32
  Ny0 = 2
  Smooth_y = 1
  Max_scale=0.03
  Max_count=10
 /
&QUADRUPOLE

  LQUAD=T

  Q_length(1)=0.15
  Q_grad(1)=0.0929277
  Q_bore(1)=0.04
  Q_pos(1)=3.95

  Q_length(2)=0.15
  Q_grad(2)=-0.0502569
  Q_bore(2)=0.04
  Q_pos(2)=4.5

  Q_length(3)=0.15
  Q_grad(3)=0.163916
  Q_bore(3)=0.04
  Q_pos(3)=5.05

  Q_length(4)=0.15
  Q_grad(4)=0.285505
  Q_bore(4)=0.04
  Q_pos(4)=5.6
 /

 &DIPOLE
  LDipole=T

  D_Type(1) = horizontal
```

```
  D1(1)=(0.1,6.0),D2(1)=(-0.1,6.0),D3(1)=(0.1,6.3),D4(1)=(-0.1,6.3)
  D_radius(1) = -0.87714, D_Gap(1,1)=0.04, D_Gap(2,1)=0.04

  D_Type(2) = horizontal
  D1(2)=(0.6,7.4),D2(2)=(0.4,7.4),D3(2)=(0.6,7.7),D4(2)=(0.4,7.7)
  D_radius(2) = 0.87714, D_Gap(1,2)=0.04, D_Gap(2,2)=0.04

  D_Type(3) = horizontal
  D1(3)=(0.6,10.0),D2(3)=(0.4,10.0),D3(3)=(0.6,10.3),D4(3)=(0.4,10.3)
  D_radius(3) = 0.87714, D_Gap(1,3)=0.04, D_Gap(2,3)=0.04

  D_Type(4) = horizontal
  D1(4)=(0.1,11.4),D2(4)=(-0.1,11.4),D3(4)=(0.1,11.7),D4(4)=(-0.1,11.7)
  D_radius(4) = -0.87714, D_Gap(1,4)=0.04, D_Gap(2,4)=0.04
/
```

Table 21: Output of the ASTRA postprocessing program at z=11.9

```
     bypass 20deg, L= 110 cm, R56~33cm, offset D~50 cm
  100000 particles from file merger.1190.002
     Particles taken into account      N =     100000
     total charge                      Q =    -4.9997E-03 nC
     horizontal beam position          x =    -1.8808E-04 mm
     vertical beam position            y =     9.7990E-06 mm
     longitudinal beam position        z =      11.90     m
     horizontal beam size          sig x =     0.1850     mm
     vertical beam size            sig y =     5.1949E-02 mm
     longitudinal beam size        sig z =     0.6327     mm
     average kinetic energy            E =      9.474     MeV
     energy spread                    dE =      40.78     keV
     transverse beam emittance     eps x =     0.1274     pi mrad mm
     correlated divergence         cor x =     5.0789E-02 mrad
     transverse beam emittance     eps y =     6.2683E-02 pi mrad mm
     correlated divergence         cor y =     1.1447E-02 mrad
     longitudinal beam emittance   eps z =      1.111     pi keV mm
     correlated energy spread      cor z =     -40.74     keV
     emittance ratio eps y/eps x         =      2.032
     Reduced emittances:
     hor. emittance minus z correlation:     =     0.1238     pi mrad mm
     hor. emittance minus z & E correlation: =     0.1237     pi mrad mm
     ver. emittance minus z correlation:     =     5.6224E-02 pi mrad mm
     ver. emittance minus z & E correlation: =     5.6223E-02 pi mrad mm
```

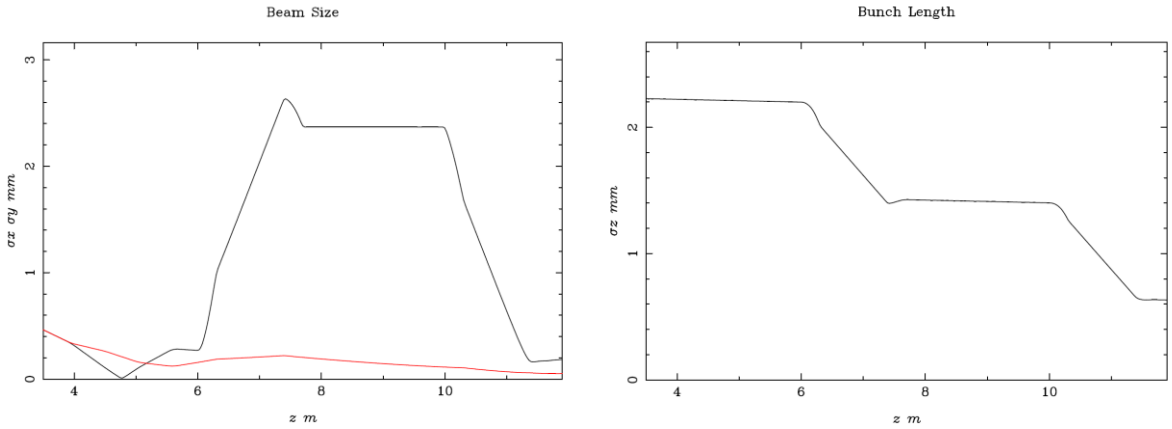

Figure 63. Transverse beam sizes (left, black curve – horizontal (x), red – vertical (y)) and bunch length (right) in the merger section. High energy spread in the merger dominates the horizontal beam size between merger dipoles (6 to 11 m from the cathode).

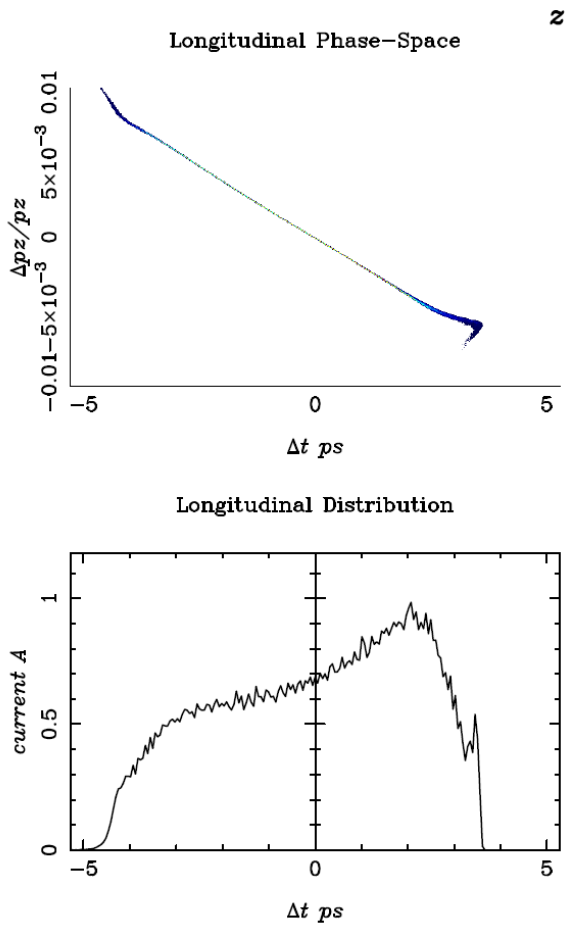

Figure 64. Longitudinal phase space (above) and current profile (below) at z=11.9 m (behind the merger section). The bunch is compressed to the rms length of ~2 ps.

9.3.5 Linac section

Input file for the linac section:

```
&NEWRUN
  Version = 2
  Head='linac'
  RUN=2
  Distribution = 'merger.1190.002',Xoff=0.0, Yoff=0.0
  EmitS=.T
  PhaseS=.T
  TrackS=.T
  RefS=.F
!  Qbunch=5E-3
  TcheckS=.F
  CathodeS=.F
  TRACK_ALL=.T,   PHASE_SCAN=.F,    AUTO_PHASE=.T
  check_ref_part=.F
  ZSTART=11.90, ZSTOP=19.5
  Zemit=300
  Zphase=30
  H_max=0.001
  H_min=0.0001
 /

 &CHARGE
  LSPCH=T
  LSPCH3D=T
  Nzf = 128
  Nz0 = 3
  Smooth_z = 1
  Nxf = 64
  Nx0 = 3
  Smooth_x = 1
  Nyf = 64
  Ny0 = 3
  Smooth_y = 1
  Max_scale=0.03
  Max_count=10
 /
&CAVITY

  Loop=.f
  LEFieLD=.t

FILE_EFieLD(1)='ref_7cell_centered.dat',C_HIGHER_ORDER(1)=.t,C_SMOOTH(1)=5,Nu
e(1)=1.3, MaxE(1)=-35.1, Phi(1)=1.0, C_pos(1)=15.394,

FILE_EFieLD(2)='ref_7cell_centered.dat',C_HIGHER_ORDER(2)=.t,C_SMOOTH(2)=5,Nu
e(2)=1.3, MaxE(2)=-35.1, Phi(2)=1.0, C_pos(2)=16.782,
```

```
FILE_EFieLD(3)='ref_7cell_centered.dat',C_HIGHER_ORDER(3)=.t,C_SMOOTH(3)=5,Nu
e(3)=1.3, MaxE(3)=-35.1, Phi(3)=1.0, C_pos(3)=18.17,
 /

&QUADRUPOLE

  LQUAD=T

  Q_length(1)=0.15
  Q_grad(1)=0.0929277
  Q_bore(1)=0.04
  Q_pos(1)=3.95

  Q_length(2)=0.15
  Q_grad(2)=-0.0502569
  Q_bore(2)=0.04
  Q_pos(2)=4.5

  Q_length(3)=0.15
  Q_grad(3)=0.163916
  Q_bore(3)=0.04
  Q_pos(3)=5.05

  Q_length(4)=0.15
  Q_grad(4)=0.285505
  Q_bore(4)=0.04
  Q_pos(4)=5.6

  Q_length(5)=0.15
  Q_grad(5)=0.204
  Q_bore(5)=0.04
  Q_pos(5)=12.15

  Q_length(6)=0.15
  Q_grad(6)=-0.402634
  Q_bore(6)=0.04
  Q_pos(6)=12.7

  Q_length(7)=0.15
  Q_grad(7)=0.18186
  Q_bore(7)=0.04
  Q_pos(7)=13.25

  Q_length(8)=0.15
  Q_grad(8)=-0.0333541
  Q_bore(8)=0.04
  Q_pos(8)=13.8
/
```

Table 22: Output of the ASTRA postprocessing program at z=19.5 m.

```
    linac
100000 particles from file linac.1950.002
   Particles taken into account      N =     100000
   total charge                      Q =   -4.9996E-03 nC
   horizontal beam position          x =    3.5293E-04 mm
   vertical beam position            y =   -1.3556E-05 mm
   longitudinal beam position        z =      19.50     m
   horizontal beam size          sig x =    3.1711E-02 mm
   vertical beam size            sig y =    6.2031E-02 mm
   longitudinal beam size        sig z =    0.5968     mm
   average kinetic energy            E =     53.41     MeV
   energy spread                    dE =     25.04     keV
   transverse beam emittance     eps x =    0.1107     pi mrad mm
   correlated divergence         cor x =   -3.4883E-03 mrad
   transverse beam emittance     eps y =    6.0661E-02 pi mrad mm
   correlated divergence         cor y =    2.1488E-03 mrad
   longitudinal beam emittance   eps z =     2.358     pi keV mm
   correlated energy spread      cor z =    -24.73     keV
   emittance ratio eps y/eps x         =     1.825
   Reduced emittances:
   hor. emittance minus z correlation:     =     0.1056     pi mrad mm
   hor. emittance minus z & E correlation: =     0.1054     pi mrad mm
   ver. emittance minus z correlation:     =     5.9746E-02 pi mrad mm
   ver. emittance minus z & E correlation: =     5.9741E-02 pi mrad mm
```

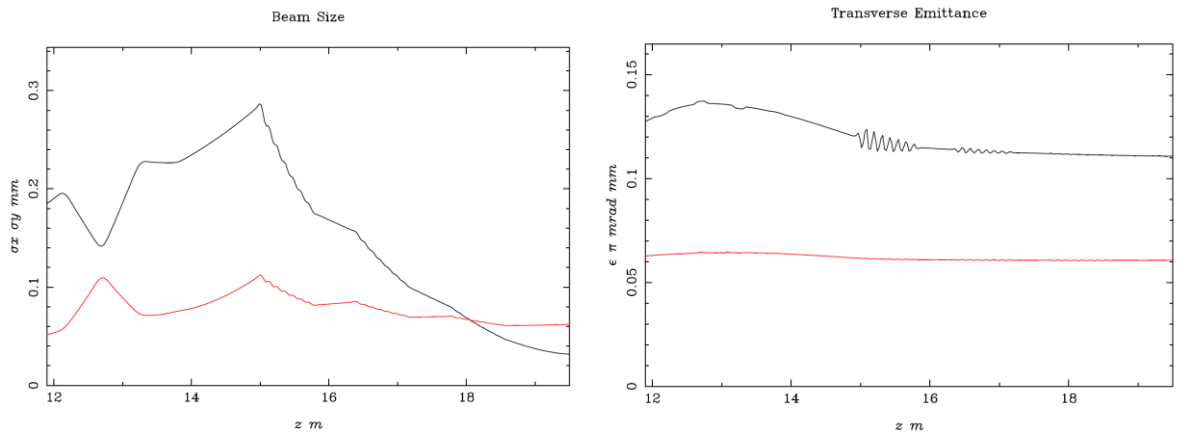

Figure 65. Transverse beam sizes (left) and projected emittances (right) in the linac section. Last step of the "emittance compensation" can be seen.

10 Appendix C: Latice functions in spreaders/recombiners

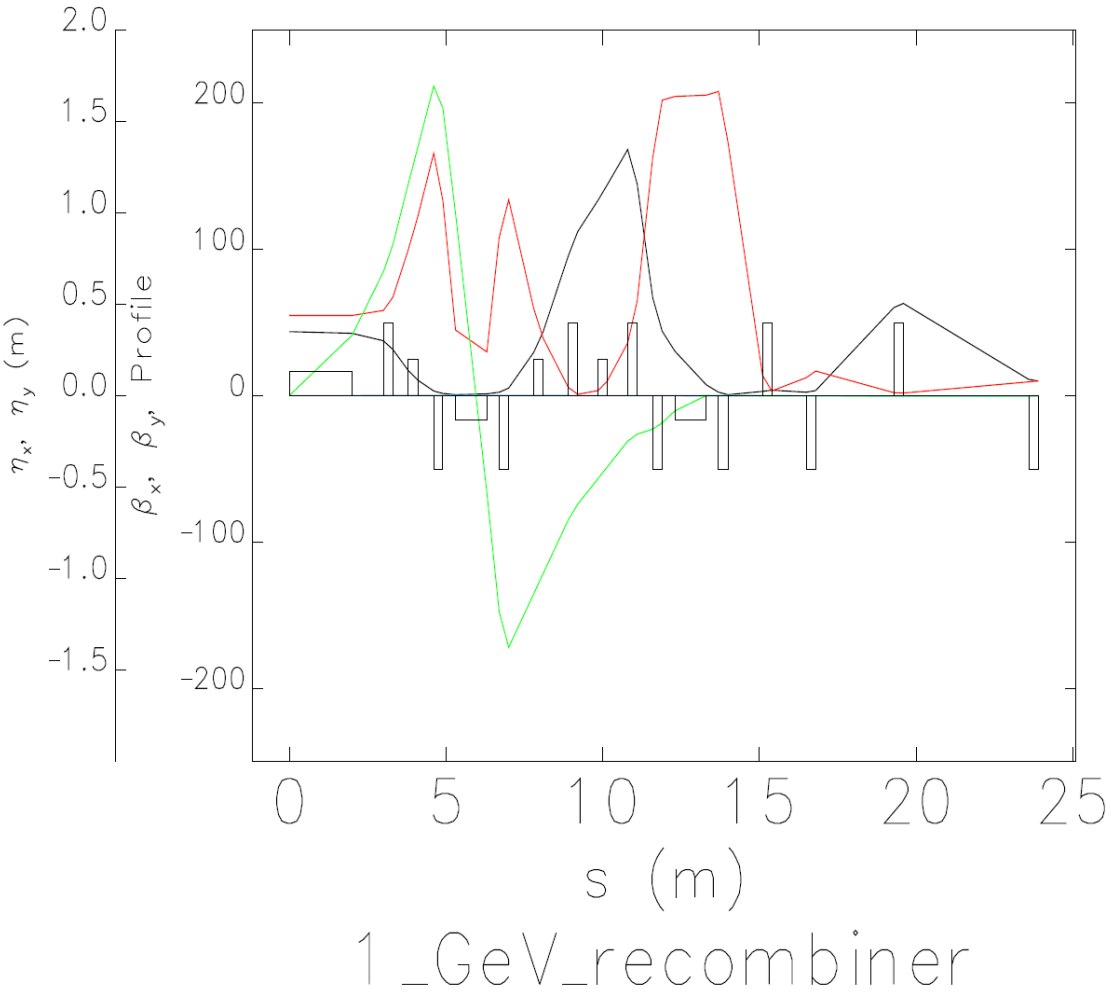

Figure 66. β functions and η function in the 1 GeV recombiner beamline.

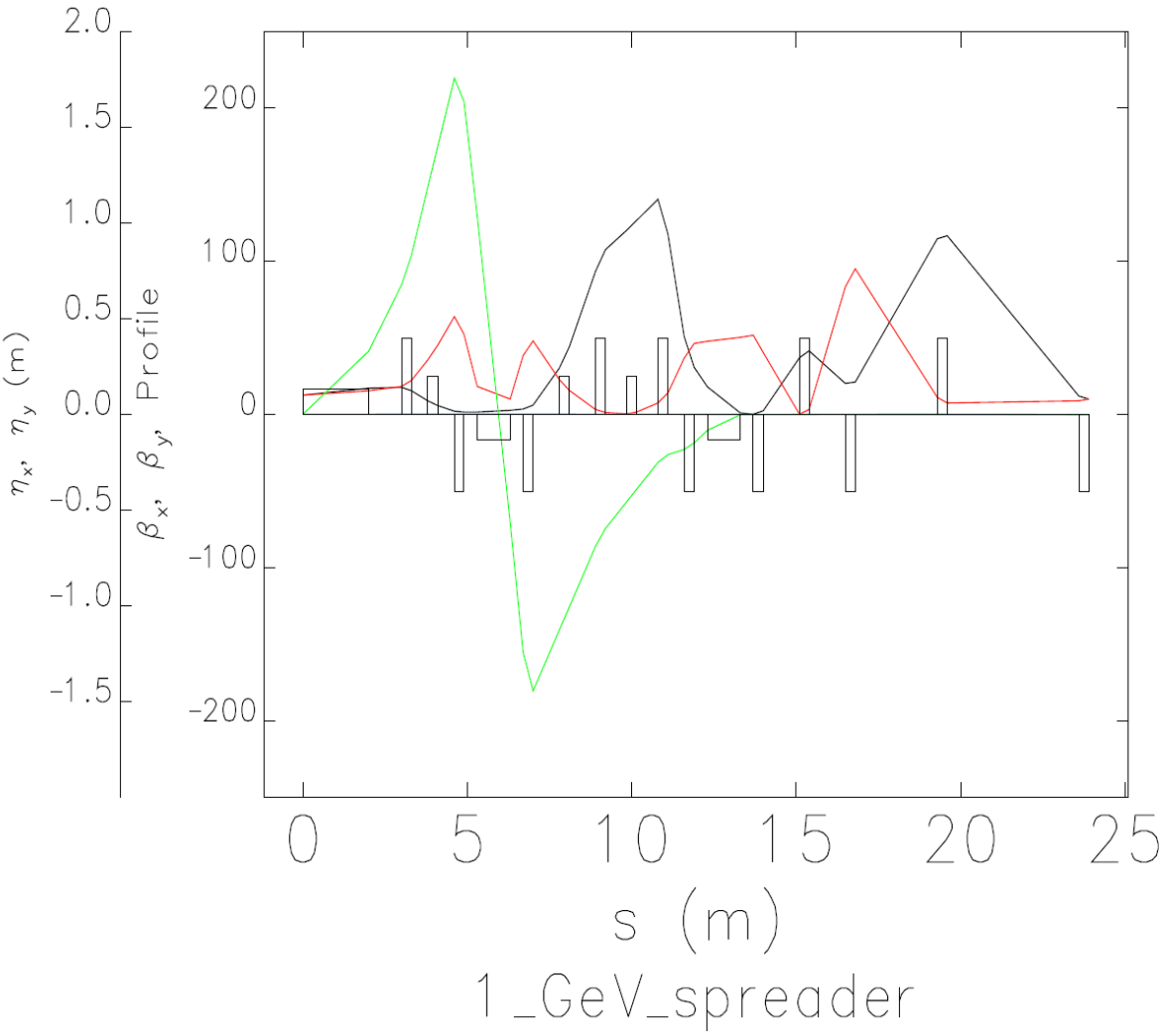

Figure 67. β functions and η function in the 1 GeV spreader beamline.

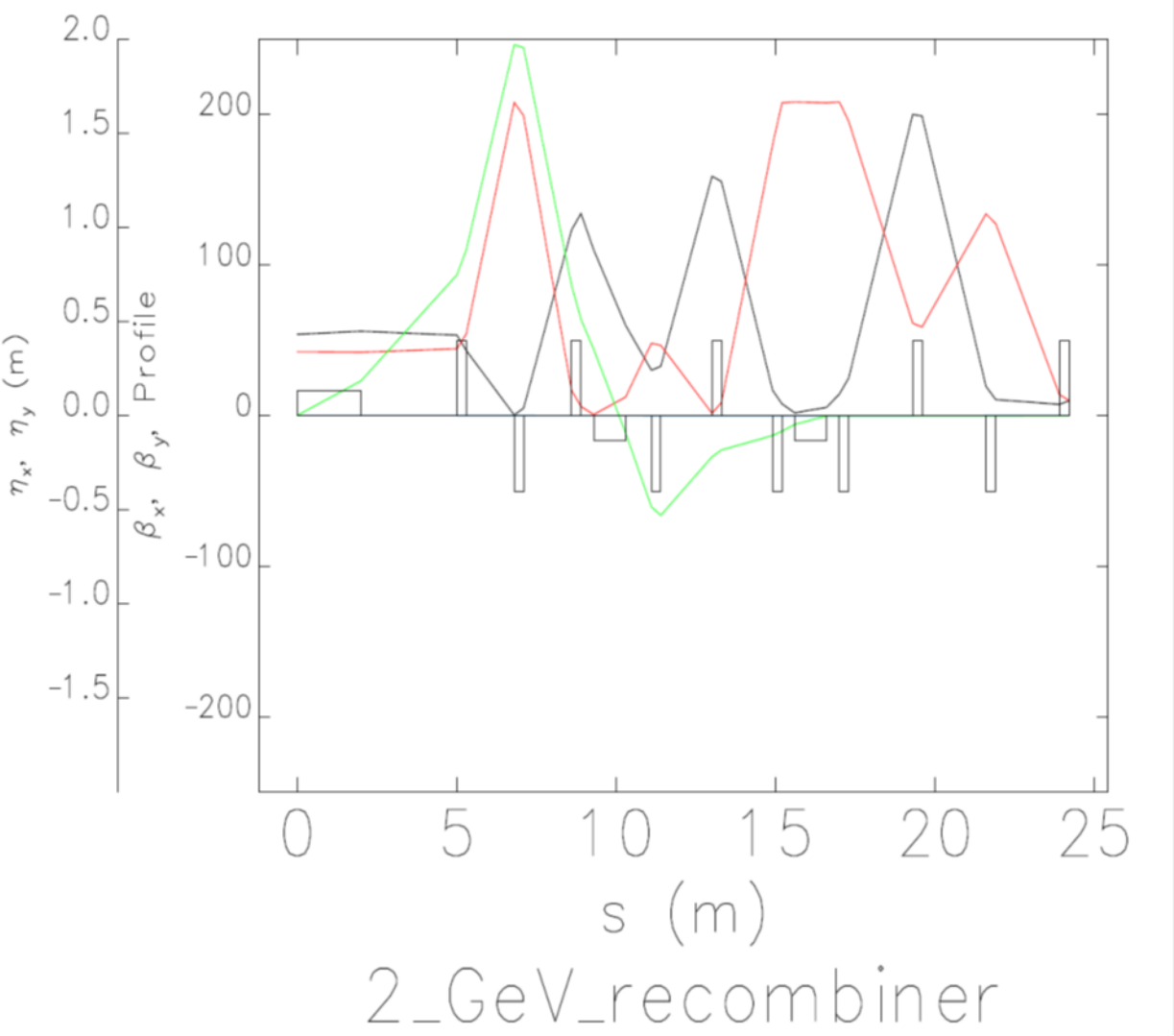

Figure 68. β functions and η function in the 2 GeV recombiner beamline.

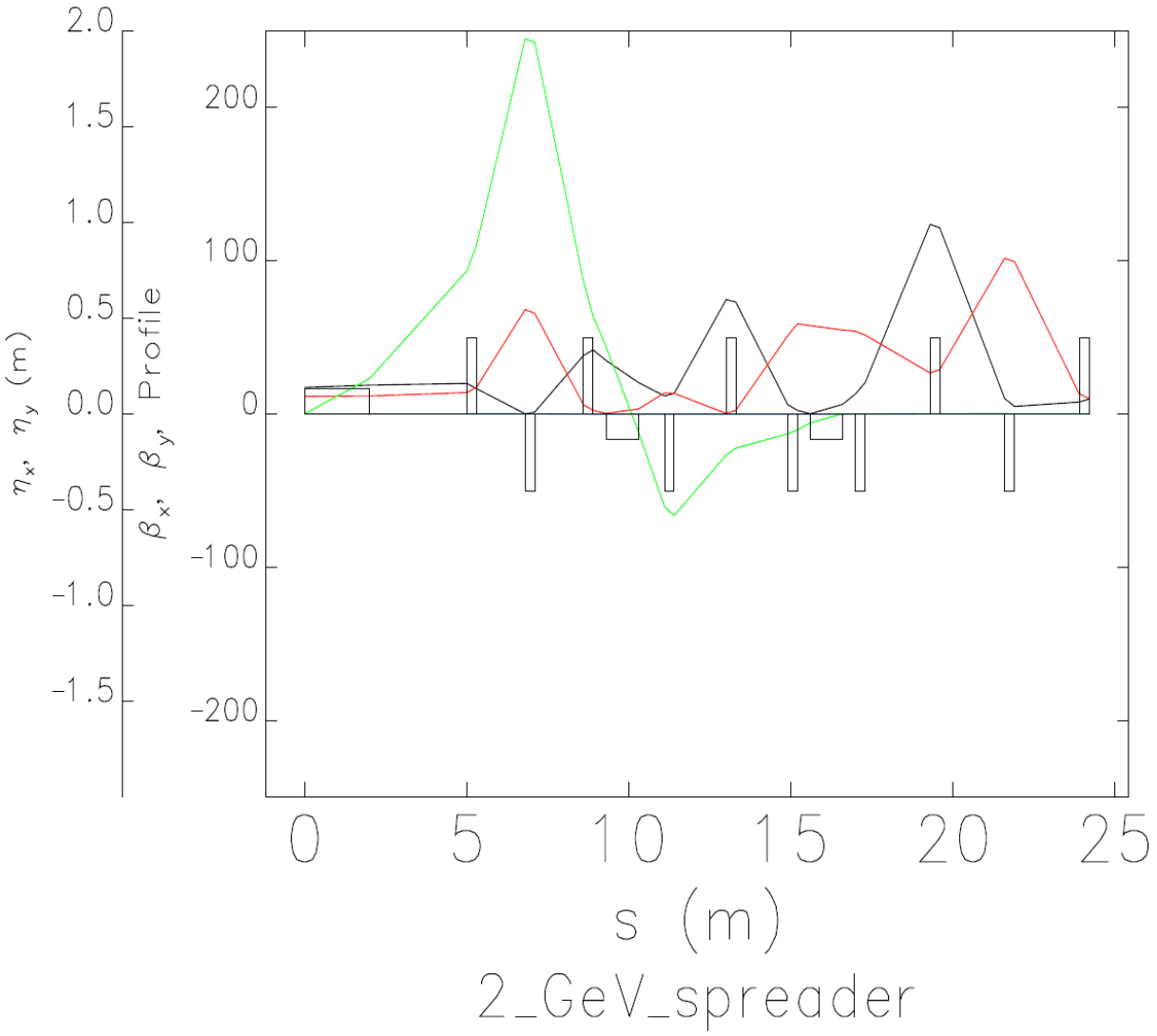

Figure 69. β functions and η function in the 2 GeV spreader beamline.

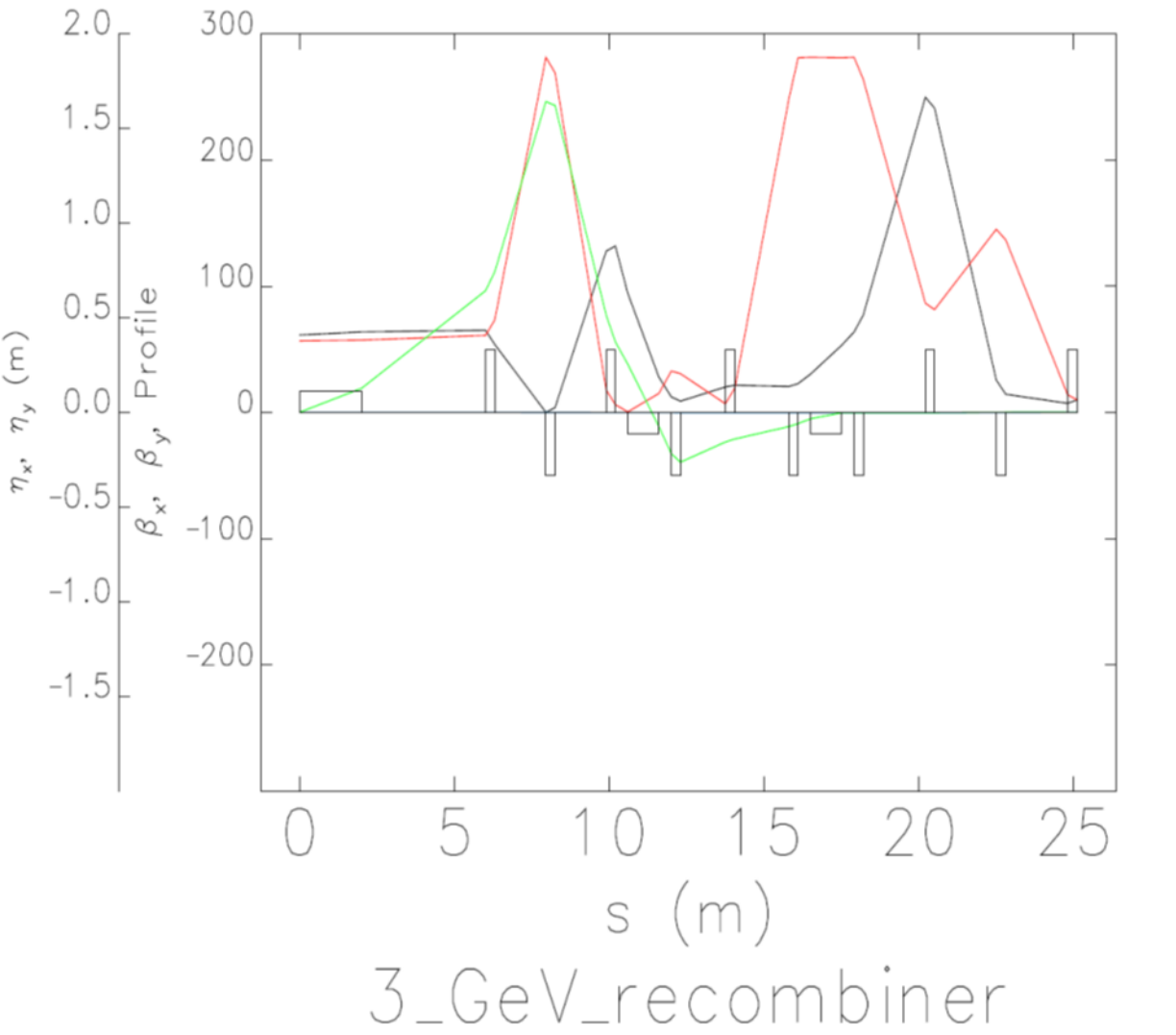

Figure 70. β functions and η function in the 3 GeV recombiner beamline.

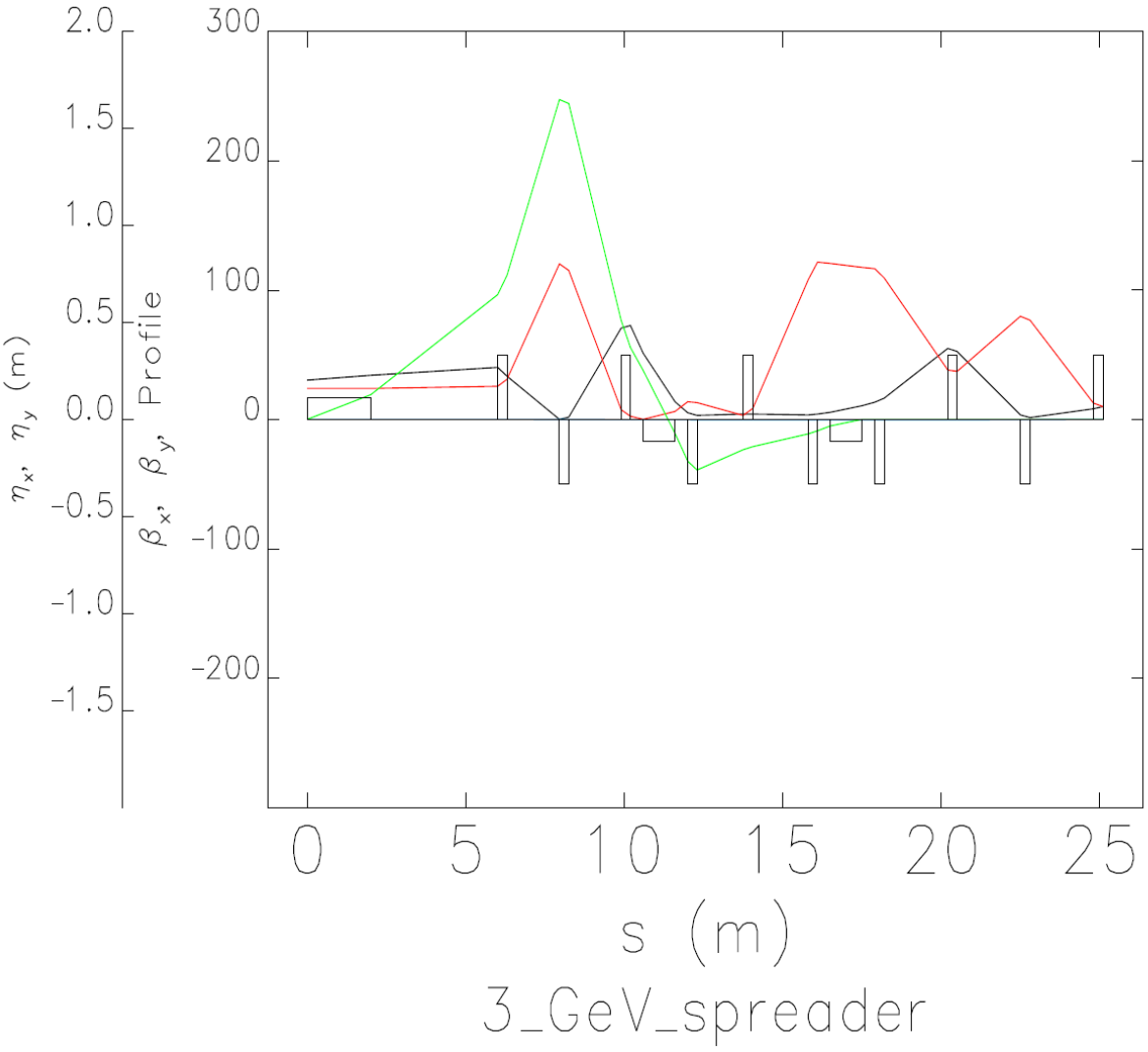

Figure 71. β functions and η function in the 3 GeV spreader beamline.

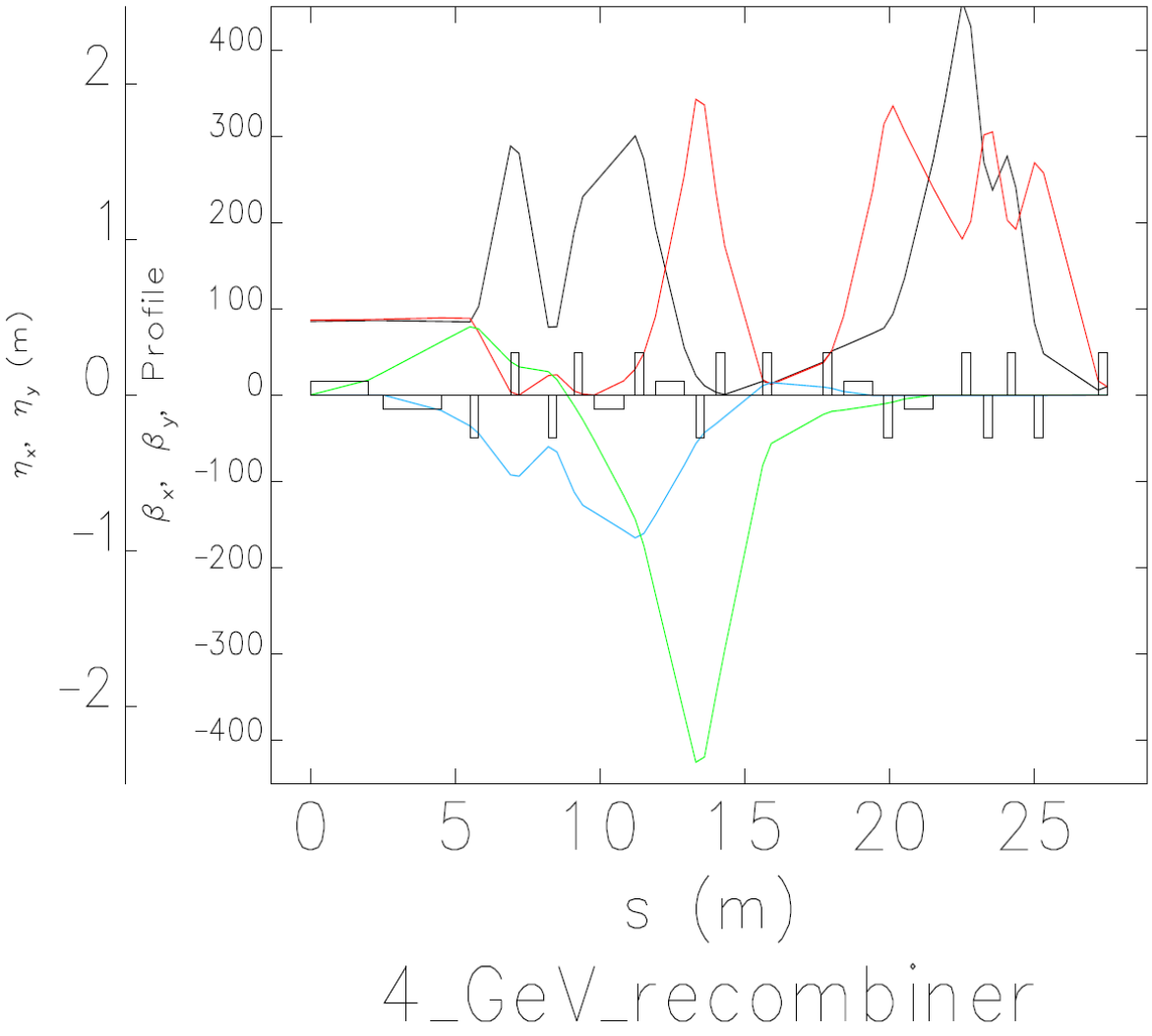

Figure 72. β functions and η function in the 4 GeV recombiner beamline.

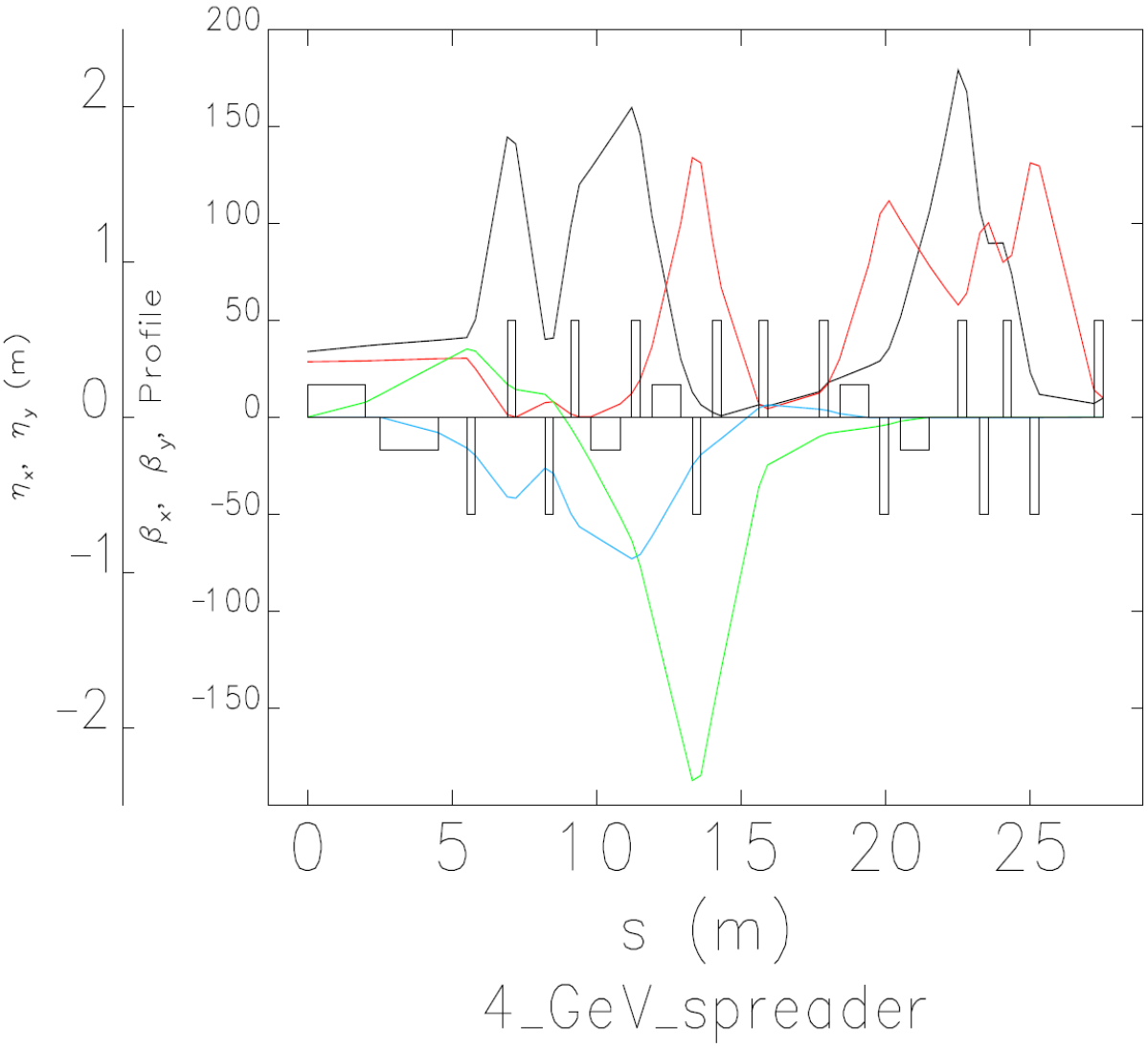

Figure 73. β functions and η function in the 4 GeV spreader beamline.

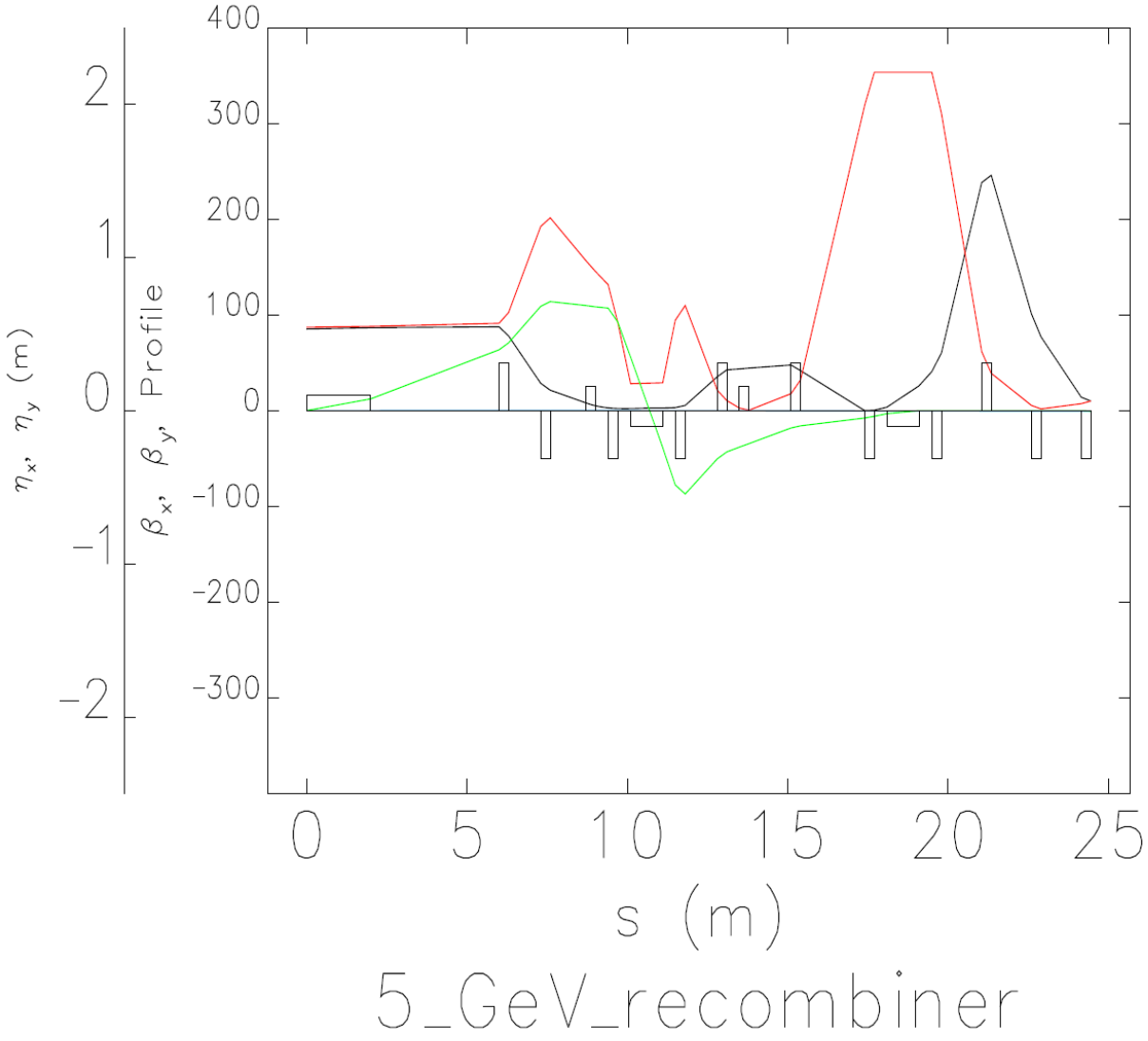

Figure 74. β functions and η function in the 5 GeV recombiner beamline.

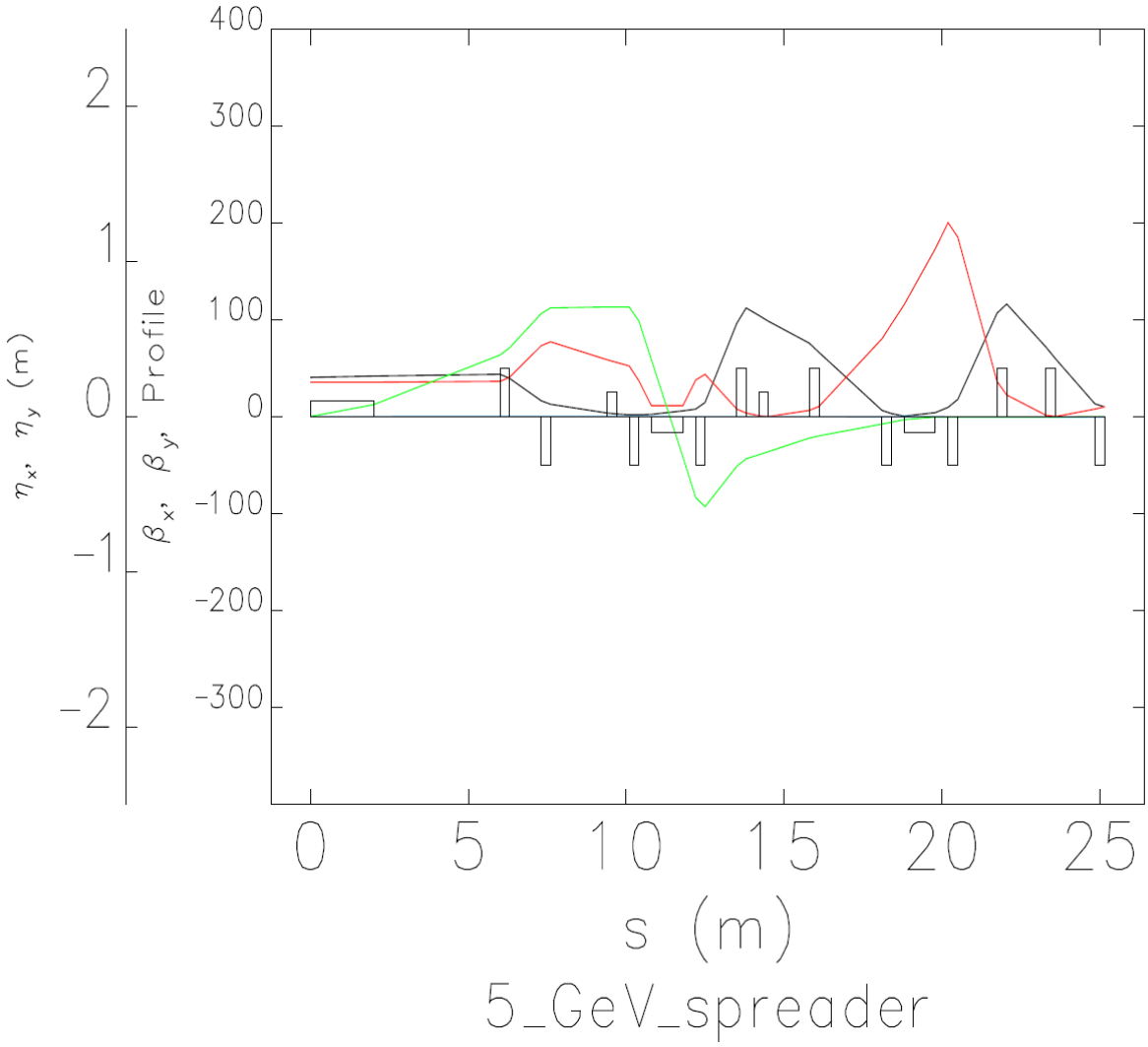

Figure 75. β functions and η function in the 5 GeV spreader beamline.

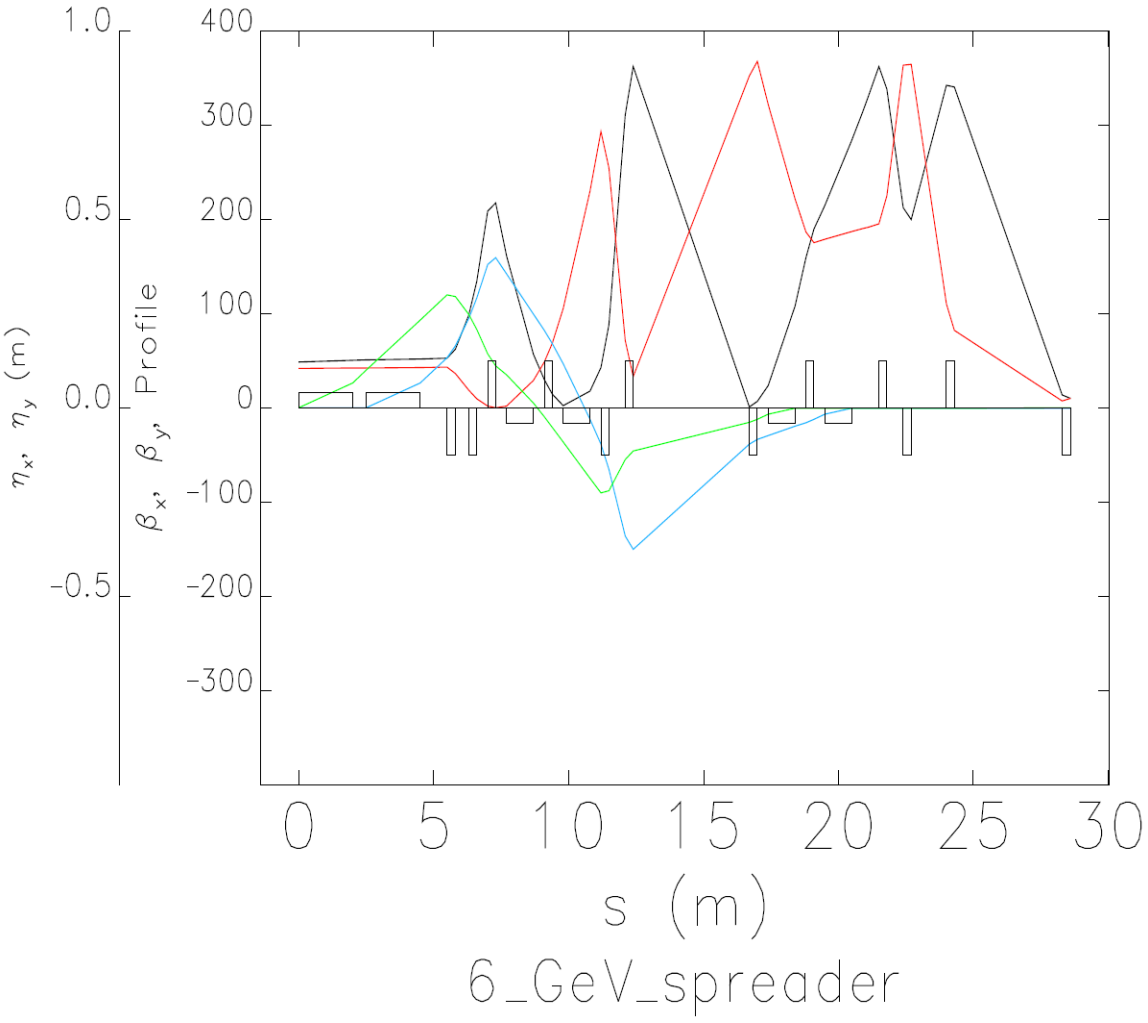

Figure 76. β functions and η function in the 6 GeV spreader beamline.

11 Appendix D: Field error estimates for FSF optics

11.1 Effects and time dependence of the field errors

It is important to take into account different effects of the field errors on the beam dynamics. Field errors can:

- produce unacceptable orbit deviations downstream
- lead to unacceptable growth of the beam size
- dilute emittance

The field errors can be

- time dependent, fast,(AC component in the current)
- time dependent, slow, (induces by temperature drifts, reproducibility due to hysteresis, reproducibility of the power supplies)
- constant in time (e.g. fabrication tolerances, absolute accuracy of the power supplies).

The requirements on the errors are different. We assume we can correct constant in time dipole field errors with steerers (or the dipole power supplies). Therefore, we demand the beam stays roughly inside the vacuum chamber (max. deviation 10 mm). Similarly, we can correct quadrupole errors. The acceptable variation of the beam size is taken to be 5% (10% in the beta-function).

For slow drifts some feedback system can be thought of. Reproducibility of the fields after switching off/on of the magnetic system or a single magnet is taken generally to be factor 10 better, than stated above for the constant in time field errors. It corresponds to beam deviations from the axis of max. 1 mm.

Fast time dependent errors lead to fast beam position oscillations and, therefore, influences the projected emittance. We assume 10% emittance from a single error source to be acceptable. If emittances from different sources are added quadratically, this corresponds to a 0.5% emittance growth from a single error source:

$$\varepsilon = \sqrt{\varepsilon_0^2 + \Delta\varepsilon^2} \approx \varepsilon_0\left(1 + \frac{\Delta\varepsilon^2}{2\varepsilon_0^2}\right) \approx \varepsilon_0 \cdot 1.005$$

11.2 Field quality tables

In the following tables the necessary field accuracy and stability of the magnetic elements in FSF is summarized. Additionally, minimal requirements on the number of steerers are given.

Table 23: Field accuracy and reproducibility of the magnetic elements in FSF.

Element type	Field accuracy	reproducibility
injector dipoles (10 MeV)	$3 \cdot 10^{-3}$	$1 \cdot 10^{-3}$
injector dipoles edge field K	$\Delta K<0.06$	
injector dipole gradient error	0.12 Gs/cm	
second injection stage dipoles (100 MeV)	$3 \cdot 10^{-3}$	$3 \cdot 10^{-4}$
second injection stage dipoles edge field K	$\Delta K<0.05$	
second injection stage dipoles gradient error	0.5 Gs/cm	
recirculator dipoles (1÷6 GeV)	$7 \cdot 10^{-3}$	$7 \cdot 10^{-4}$
recirculator dipoles edge field K	harmless	
recirculator dipole gradient error	12 Gs/cm	
spreader/recombiner dipoles (1÷6 GeV)	$7 \cdot 10^{-4}$	$7 \cdot 10^{-5}$
spreader/recombiner dipoles edge field K	harmless	
spreader/recombiner dipole gradient error	0.5 Gs/cm	
10 MeV quadrupoles	$5 \cdot 10^{-3}$	$5 \cdot 10^{-4}$
100 MeV quadrupoles	$5 \cdot 10^{-3}$	$5 \cdot 10^{-4}$
6 GeV quadrupoles	$5 \cdot 10^{-3}$	$5 \cdot 10^{-4}$
Spreader/recombiner quadrupoles	$6 \cdot 10^{-5}$	$6 \cdot 10^{-6}$
sextupoles		

Table 24: Power supply (AC field) ripples of the magnetic elements in FSF, slow drifts, and reproducibility of the power supply current.

Element type	fast time-dependent field accuracy (power supply ripple)	slow drifts / reproducibility by off/on
injector dipoles		$1 \cdot 10^{-3}$
second injection stage dipoles		$3 \cdot 10^{-4}$
recirculator dipoles		$7 \cdot 10^{-4}$
spreader/recombiner dipoles		$7 \cdot 10^{-5}$
10 MeV quadrupoles	10^{-2}	$5 \cdot 10^{-4}$
100 MeV quadrupoles	10^{-2}	$5 \cdot 10^{-4}$
6 GeV quadrupoles (recirculator)	10^{-2}	$5 \cdot 10^{-4}$
spreader/recombiner quadrupoles	$2 \cdot 10^{-4}$	$6 \cdot 10^{-6}$
sextupoles		
steers (injector)	$7 \cdot 10^{-4}$	
steers (recirculator)	$1.5 \cdot 10^{-3}$	

Table 25: Alignment accuracy of the magnetic elements in FSF.

Element type	alignment accuracy
injector dipole edge angle, rad	0.01
injector dipole yaw angle, rad	$3 \cdot 10^{-3}$
second injection stage dipole edge angle, rad	0.01
second injection stage dipole yaw angle, rad	$3 \cdot 10^{-3}$
recirculator dipole edge angle, rad	harmless
recirculator dipole yaw angle, rad	$7 \cdot 10^{-3}$
spreader/recombiner dipole edge angle, rad	harmless
spreader/recombiner dipole yaw angle, rad	$7 \cdot 10^{-4}$
10 MeV quadrupoles, transversally	0.4 mm
100 MeV quadrupoles, transversally	0.5 mm
6 GeV quadrupoles	0.6 mm
spreader/recombiner quadrupoles (worst case)	0.01 mm
sextupoles, transversally	0.2 mm
steers (injector)	
steers (second stage injection and recirculator)	

Table 26: Mechanical stability to vibrations.

Magnet	Mechanical stability (vibration amplitude)
10 MeV quadrupoles	1.5 µm
100 MeV quadrupoles	0.4 µm
6 GeV quadrupoles	0.5 µm

Maximal distance between steerers (in each plane horizontal and vertical)

- in the injector (at 10 MeV) – 70 cm
- in the second injection stage (at 100 MeV) – 2.5 m
- in the recirculator – 20 m
- in the spreaders/recombiners -20 m

11.3 Dipole errors

The source of the field can be:

- dipole magnet field error (power supply error)
- dipole magnet field error (fabrication tolerances)
- dipole magnet field error (alignment error)
- dipole magnet field error (remnant field)
- quadrupole with an offset of the magnetic center (alignment error)
- sextupole with an offset of the magnetic center (alignment error)
- stray fields in the accelerator hall (earth magnet field, etc.)

Each dipole error of amplitude ΔBon the length L leads to an angle $d\theta = e\frac{\Delta BL}{pc}$. This angle will be transported in the downstream optics by

$$x = m_{12}d\theta = \sqrt{\beta_0\beta_1}\sin(\mu)e\frac{\Delta BL}{pc}$$

where beta-functions are taken at the location of the field error (0) and at the observation point (1), μ is the betatron phase advance.

Next two expressions give the orbit deviation for a field error in a dipole with the total bending angle θ, and for other integrated dipole errors.

$$\frac{\Delta B}{B} = \frac{x}{\theta\sqrt{\beta_0\beta_1}\sin(\mu)} \text{ or } \Delta BL = \frac{pcx}{e\sqrt{\beta_0\beta_1}\sin(\mu)}$$

11.3.1 Dipole magnetic field errors (fabrication tolerances and DC power supply error)

For an estimate we take an average beta-function to be 10 m, $\sin(\mu) = 1$, max. tolerable orbit deviation x=10 mm.

For the DC field tolerance of injector dipoles we get

$$\frac{\Delta B}{B}_{inj} = \frac{10\ mm}{0.314 \cdot 10\ m} \approx 3 \cdot 10^{-3}$$

For the DC field tolerance of dipoles in the second injection stage

$$\frac{\Delta B}{B}_{inj2} = \frac{10\ mm}{1 \cdot 10\ m} \approx 10^{-3}$$

For the DC field tolerance of dipoles in the recirculator

$$\frac{\Delta B}{B}_{recirc} = \frac{10\ mm}{0.131 \cdot 10\ m} \approx 7 \cdot 10^{-3}$$

For the DC field tolerance of dipoles in the spreader/recombiner (should be calculated separately for each dipole, while β-functions vary more than an order of magnitude. The number below is close to the worst case)

$$\frac{\Delta B}{B}_{spreader} = \frac{10\ mm}{0.05 \cdot 300\ m} \approx 7 \cdot 10^{-4}$$

For other integrated errors at 10 MeV

$$\Delta BL = \frac{10 \cdot 10^6 eV \cdot 10\ mm}{e \cdot 300 \cdot 10\ m} \approx 30\ Gs \cdot cm$$

For other integrated errors at 100 MeV, 1 GeV and 6 GeV one get respectively

$$\Delta BL \approx 300\ Gs \cdot cm, 3\ kGs \cdot cm \text{ and } 18 kGs \cdot cm$$

In the spreader/recombiner, where beta-functions are large (up to 800 m), it gives

$$\Delta BL \approx 300\ Gs \cdot cm$$

11.3.2 Dipole alignment errors

11.3.2.1 Dipole rotation (yaw)

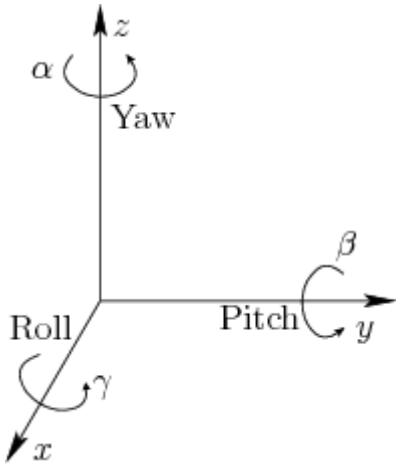

If the dipole is rotated along the z-axis by an angle α, it has a steering effect on the beam in the vertical plane: $d\theta = e\frac{\Delta BL}{pc} = \alpha\theta$. Therefore, the magnet must be aligned to the accuracy better than

in the injector:

$$\alpha = \frac{\Delta B}{B}_{inj} \approx 3 \cdot 10^{-3}$$

dipoles in the second injection stage:

$$\alpha = \frac{\Delta B}{B}_{inj2} \approx 10^{-3}$$

in the recirculator

$$\alpha = \frac{\Delta B}{B}_{recirc} \approx 7 \cdot 10^{-3}$$

in the spreader/recombiner (should be calculated separately for each dipole)

$$\alpha = \frac{\Delta B}{B}_{spreader} \approx 7 \cdot 10^{-4}$$

11.3.3 Quadrupole alignment

In a quadrupole, the field is given by $B_y = Gx$, therefore, alignment tolerance should be better, than

$$\Delta x = \frac{\Delta BL}{GL}$$

In the injector quadrupoles it gives

$$\Delta x = \frac{30\ Gs \cdot cm}{50\frac{Gs}{cm} \cdot 15\ cm} \approx 0.4\ mm$$

In the second injection stage

$$\Delta x = \frac{300\ Gs \cdot cm}{300\frac{Gs}{cm} \cdot 20\ cm} \approx 0.5\ mm$$

In the recirculator (6 GeV, K_{max}=5 m^{-2})

$$\Delta x = \frac{18000\ Gs \cdot cm}{10^4 \frac{Gs}{cm} \cdot 30\ cm} \approx 0.6\ mm$$

in the spreader/recombiner quadrupoles it gives

$$\Delta x = \frac{300\ Gs \cdot cm}{10^4 \frac{Gs}{cm} \cdot 30\ cm} \approx 0.01\ mm$$

11.3.4 Sextupole alignment

In a sextupole, the field is given by $B_y = \frac{1}{2}mx^2$. Misaligned sextupoles produce also a dipole component of the field $B_y = \frac{1}{2}m(x-\Delta x)^2 = \frac{1}{2}mx^2 - mx\Delta x + \frac{1}{2}m\Delta x^2$. Therefore, alignment tolerance should be better, than

$$\Delta x = \sqrt{\frac{2\Delta BL}{mL}}$$

For the second stage injection sextupoles (100 MeV) it gives

$$\Delta x = \sqrt{\frac{2 \cdot 150\ Gs \cdot cm}{80 \frac{Gs}{cm^2} \cdot 10\ cm}} \approx 0.6\ mm$$

Sexupole strength taken here (~500 1/m^3) is our estimation of what would be necessary to set the second order in longitudinal motion (non-linearity compensation in the short pulse mode)

11.3.5 Maximal distance between steerers

One can estimate the orbit deviation in a uniform field (earth field $B \approx 0.5\ Gs$)

$$x = \frac{Ld\theta}{2} = e\frac{\Delta BL^2}{2pc} \rightarrow L = \sqrt{\frac{2pcx}{e\Delta B}}$$

Orbit deviation due to the earth magnetic field is important for the low energy part of the accelerator.

Maximal distance between steerers in the injector for $x = 0.4\ mm$:

$$L = \sqrt{\frac{2 \cdot 10 \cdot 10^6 eV \cdot 0.04\ cm}{e \cdot 300 \cdot 0.5\ Gs}} \approx 70\ cm$$

Maximal distance between steerers in the second injection stage for $x = 0.5\ mm$:

$$L = \sqrt{\frac{2 \cdot 100 \cdot 10^6 eV \cdot 0.05\ cm}{e \cdot 300 \cdot 0.5\ Gs}} \approx 250\ cm$$

Maximal distance between steerers in the recirculator for 6 GeV and $x = 0.6\ mm$:

$$L = \sqrt{\frac{2 \cdot 6 \cdot 10^9 eV \cdot 0.06\ cm}{e \cdot 300 \cdot 0.5\ Gs}} \approx 20\ m$$

At the high energy part of the accelerator, on the other hand, one can set a requirement on the maximal distance between steerers if one allows some maximal beam deviation e.g. in quadrupoles. We could start again with $x = m_{12} d\theta$ for the beam offset and get

$$L = \frac{pcx}{\Delta B e \sqrt{\beta_0 \beta_1} \sin(\mu)}$$

But after substituting numerical values in the recirculator for $x = 0.6\ mm$ one gets

$$L = \frac{18000\ Gs \cdot cm}{0.5\ Gs} \frac{x}{10\ mm} \approx 20\ m$$

which is consistent with the estimation above. It should be mentioned here, that other stray fields in the accelerator hall can be stronger than the earth field, which was takes for this estimation.

11.3.6 Emittance dilution effect

The Figure 77 demonstrates the mechanism of the projected emittance growth due to a fast variable dipole field. The projected emittance growth of a beam at a point of a fast periodical field error is given by

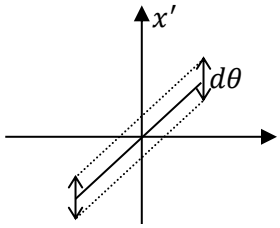

Figure 77. Mechanism of the projected emittance growth in a dipole field.

$$\frac{\Delta\varepsilon}{\varepsilon} = \frac{d\theta \cdot x_0}{2\sqrt{2}\varepsilon} = \frac{e\Delta B L x_0}{2\sqrt{2} pc\varepsilon}$$

(ΔB is the "peak to peak" field oscillation amplitude. $2\sqrt{2}$ is the result of the averaging of $\langle x'^2 \rangle$ over time.) Therefore, the field must be stable to better than $\frac{\Delta B}{B} = \frac{\Delta\varepsilon}{\varepsilon} \frac{\varepsilon R}{x_0 L} 2\sqrt{2} = 2\sqrt{2} \frac{\Delta\varepsilon_n}{\gamma x_0 \theta}$

If we assume 10% projected emittance to be acceptable from a single error source, we estimate:

in the injector dipoles

$$\frac{\Delta B}{B} = \frac{2\sqrt{2} \cdot 0.01 \cdot 10^{-6}\ m}{20 \cdot 0.5\ mm \cdot 0.314} \approx 1 \cdot 10^{-5}$$

in the dipoles of the second injection stage

$$\frac{\Delta B}{B} = \frac{2\sqrt{2} \cdot 0.01 \cdot 10^{-6}\, m}{200 \cdot 0.04\, mm \cdot 1} \approx 3 \cdot 10^{-6}$$

in the recirculator dipoles

$$\frac{\Delta B}{B} = \frac{2\sqrt{2} \cdot 0.01 \cdot 10^{-6}\, m}{12000 \cdot 0.003\, mm \cdot 0.07} \approx 1 \cdot 10^{-5}$$

in spreader/recombiner dipoles

$$\frac{\Delta B}{B} = \frac{2\sqrt{2} \cdot 0.01 \cdot 10^{-6}\, m}{12000 \cdot 0.015\, mm \cdot 0.07} \approx 2 \cdot 10^{-6}$$

These (very tight) tolerances are relieved by the fact that AC component in the current (ripples) penetrate into the magnetic field in the region of the beam only partially (skin currents in the magnet joke and vacuum chamber).

Additionally, if all errors in the merger or the arcs have the same relative amplitude and are in phase (50 Hz AC frequency or the inverter frequency of the power supplies), the emittance growth will cancel out. This is due to the fact, that changing all dipoles and quads fields by $\Delta B/B$ is equivalent to a change of the beam momentum by $\delta = \Delta p/p$. Since the bends are achromatic to the first order, this change of the field will affect the emittance only due to the non-zero 2nd and higher order dispersions.

Emittance growth due to the second order dispersion can be estimated separately for the final beam offset and angle:

$$\Delta\varepsilon \sim \Delta x \cdot x'_0 = T_{166} x'^2_0 \delta^2 \Rightarrow \delta < \sqrt{\frac{\Delta\varepsilon_n}{\gamma T_{166} x'_0}} \approx 10^{-2}$$

$$\Delta\varepsilon \sim \Delta x' \cdot x_0 = T_{266} x'^2_0 \delta^2 \Rightarrow \delta < \sqrt{\frac{\Delta\varepsilon_n}{\gamma T_{266} x_0}} \approx 8 \cdot 10^{-3}$$

(numerical values for the CDR merger design are taken: $T_{166} \approx 0.4\, m$; $T_{266} \approx 0.24$; $x_0 = 0.6\, mm$; $x'_0 = 0.23\, mrad$)

Making the estimation for the projected emittance growth due to a fast variable dipole field in steering coils in the injector one gets:

$$\frac{\Delta B}{B} = \frac{2\sqrt{2} \cdot 0.01 \cdot 10^{-6}\, m}{20 \cdot 1\, mm \cdot 0.002} \approx 7 \cdot 10^{-4}$$

second stage injection:

$$\frac{\Delta B}{B} = \frac{2\sqrt{2} \cdot 0.01 \cdot 10^{-6}\, m}{200 \cdot 0.2\, mm \cdot 0.0005} \approx 1.5 \cdot 10^{-3}$$

in the recirculator:

$$\frac{\Delta B}{B} = \frac{2\sqrt{2} \cdot 0.01 \cdot 10^{-6}\, m}{12000 \cdot 0.003\, mm \cdot 0.0005} \approx 1.5 \cdot 10^{-3}$$

(the steering is taken to be 2 mrad in the injector and 0.5 mrad in the second stage injection and recirculator. Should be corrected, when steering concept is ready. Average beam size is taken for the estimation. Unlike the dipoles with bulk iron joke, steerer can translate current ripple directly into the field ripple.)

11.3.7 Emittance dilution effect due to a fast mechanical movement of a quadrupole

Mechanical movement of a quadrupole Δx leads to an angle deviation of the beam $d\theta = \frac{eL}{pc}\Delta B = \frac{eL}{pc} G\Delta x$. This fast variation of the angle produces emittance growth

$$\frac{\Delta\varepsilon}{\varepsilon} = \langle d\theta^2 \rangle \cdot x_0 = \frac{eG\Delta x L x_0}{2\sqrt{2}pc\varepsilon}$$

Here $2\sqrt{2}$ is again the result of the averaging of $\langle x'^2 \rangle$ over time. Therefore one can estimate

$$\Delta x = \frac{2\sqrt{2}\varepsilon_n}{\gamma x_0} F \frac{\Delta\varepsilon}{\varepsilon}$$

For quadrupoles in injector: $\Delta x = \frac{2\sqrt{2}\cdot 10^{-7}\, m}{20\cdot 0.5\, mm} 0.5\, m \cdot 0.1 \approx 1.5\, \mu m$

For quadrupoles in second stage injection: $\Delta x = \frac{2\sqrt{2}\cdot 10^{-7}\, m}{200\cdot 0.2\, mm} 0.5\, m \cdot 0.1 \approx 0.4\, \mu m$

For quadrupoles in recirculator: $\Delta x = \frac{2\sqrt{2}\cdot 10^{-7}\, m}{12000\cdot 0.003\, mm} 0.6\, m \cdot 0.1 \approx 0.5\, \mu m$

11.4 Quadrupole errors

The source of the field can be:

- quadrupole magnet field error (power supply error)
- quadrupole magnet field error (fabrication tolerances)
- sextupole with an offset of the magnetic center (alignment error)
- stray fields in the accelerator hall
- dipole fringing field errors (edge angle and K-value)
- gradients in the field of dipole magnets

Each quadrupole error of amplitude ΔG on the length L leads to an additional focusing with $F = \frac{pc}{e\Delta GL}$. This additional focusing will change the Twiss parameters in the following beam line. The matrix of this quadrupole is

$$dM = \begin{pmatrix} 1 & 0 \\ -1/F & 1 \end{pmatrix}$$

Assuming the additional focusing to be small, one can find in linear approximation the variations of the beta-function and phase from relations:

$$\begin{pmatrix} m_{11} & m_{12} \\ m_{21} & m_{22} \end{pmatrix} = \begin{pmatrix} \sqrt{\frac{\beta}{\beta_0}}(cos\mu + \alpha_0 sin\mu) & \sqrt{\beta\beta_0}sin\mu \\ \frac{(\alpha_0 - \alpha)cos\mu - (1 + \alpha\alpha_0)sin\mu}{\sqrt{\beta\beta_0}} & \sqrt{\frac{\beta_0}{\beta}}(cos\mu - \alpha sin\mu) \end{pmatrix}$$

$$\begin{pmatrix} m_{11} & m_{12} \\ m_{21} & m_{22} \end{pmatrix}\begin{pmatrix} 1 & 0 \\ -\frac{1}{F} & 1 \end{pmatrix} = \begin{pmatrix} \sqrt{\frac{\beta + \delta\beta}{\beta_0}}\big(cos(\mu + \delta\mu) + \alpha_0 sin(\mu + \delta\mu)\big) & \sqrt{(\beta + \delta\beta)\beta_0}sin(\mu + \delta\mu) \\ \dots & \dots \end{pmatrix}$$

$$\Rightarrow \begin{Bmatrix} \sqrt{\beta}sin\mu = \sqrt{(\beta + \delta\beta)}sin(\mu + \delta\mu) \\ \sqrt{\beta}(cos\mu + \alpha_0 sin\mu) - \frac{\beta_0}{F}\sqrt{\beta}sin\mu = \sqrt{\beta + \delta\beta}\big(cos(\mu + \delta\mu) + \alpha_0 sin(\mu + \delta\mu)\big) \end{Bmatrix}$$

where Twiss parameters with the index 0 are at the point of the field error. Leaving out the algebra, the result is

- $\frac{\delta\beta}{\beta} = -\frac{\beta_0}{F}\sin(2\mu) = -\frac{e\Delta G L\beta_0}{pc}\sin(2\mu)$
- $\delta\mu = \frac{\beta_0}{F}\sin^2\mu = \frac{e\Delta G L\beta_0}{pc}\sin^2\mu$

11.4.1 Quadrupole magnetic field errors (fabrication tolerances and DC power supply error)

We assume 10% variation of the beta-function to be acceptable, take an average beta-function to be 10 m, $\sin(\mu) = 1$.

For the DC field tolerance of quadrupoles we get

in the both stages of the injection and recirculator

$$\frac{\Delta G}{G} = \frac{pc}{eGL\beta_0}\frac{\delta\beta}{\beta_1} = \frac{F_0}{\beta_0}\frac{\delta\beta}{\beta_1} \sim \frac{0.5\ m}{10\ m}0.1 \approx 5 \cdot 10^{-3}$$

in the spreader/recombiner (worst case beta-function is taken)

$$\frac{\Delta G}{G} = \frac{F_0}{\beta_0}\frac{\delta\beta}{\beta_1} = \frac{0.5\ m}{800\ m}0.1 \approx 6 \cdot 10^{-5}$$

For other integrated quadrupole errors in the injector

$$\Delta GL = \frac{pc}{e\beta_0}\frac{\delta\beta}{\beta_1} = \frac{10\cdot 10^6}{300\cdot 1000}0.1 \approx 3\ Gs$$

in the second injection stage, recirculator arcs, and spreader/recombiner

$$\Delta GL \approx 30\ Gs, 1800\ Gs, \text{and } 60\ Gs$$

11.4.2 Dipole fringing field errors

Since we use parallel-faced dipoles, edge focusing is quite strong. Due to the finite extension of the dipole magnet fringe field, additional focusing in the vertical plane appears. The matrix of the edge of a magnet with a gap g, bending radius ρ, edge angle α is given by

$$M = \begin{pmatrix} 1 & 0 & 0 & 0 \\ \frac{tan\alpha}{\rho} & 1 & 0 & 0 \\ 0 & 0 & 1 & 0 \\ 0 & 0 & -\frac{tan(\alpha-\varphi)}{\rho} & 0 \end{pmatrix}, \text{ where } \varphi \approx K\frac{g}{\rho}\frac{1+sin^2\alpha}{cos\alpha}, \text{ and } K = \int_{-\infty}^{\infty}\frac{B(z)(B_0-B(z))}{gB_0^2}dz.$$

First, we estimate the influence of the edge angle accuracy. Additional focusing will be approximately $\Delta\frac{1}{F} \approx \frac{\Delta\alpha}{\rho}$ or, expressed over integral gradient error, $\Delta GL \approx \frac{pc}{e}\frac{\Delta\alpha}{\rho} = B\Delta\alpha$.

This gives the alignment accuracy:

of the injector dipoles: $\Delta\alpha \approx \frac{3\ Gs}{300\ Gs} \approx 0.01 \approx 0.6°$

of the second injection stage dipoles: $\Delta\alpha \approx \frac{30\ Gs}{3000\ Gs} \approx 0.01 \approx 0.6°$

of the recirculator dipoles: $\Delta\alpha \approx \frac{1800\ Gs}{15000\ Gs} \approx 0.12 \approx 7°$(harmless)

Second, we estimate the influence of the fringe field integral K. For real magnets K is in the range 0.3 - 1. Default value for most modeling programs is 0.45. If the fringe field parameter deviates from the assumed value by ΔK, additional focusing will be approximately $\Delta\frac{1}{F} \approx \frac{\Delta Kg}{\rho^2}$ or, expressed over integral gradient error, $\Delta GL \approx \frac{pc}{e}\frac{\Delta Kg}{\rho^2}$.

This gives the integrated quadrupole error due to fringe field errors:

in the injector (1 dipole, 2 edges):

$$\Delta GL \approx 2\frac{10\cdot 10^6}{300}\frac{5.2\ cm}{80^2 cm^2}\cdot\Delta K \approx 45\ Gs\cdot\Delta K$$

in the second injection stage (1 dipole, 2 edges):

$$\Delta GL \approx 2\frac{100 \cdot 10^6}{300}\frac{5.2\ cm}{80^2 cm^2} \cdot \Delta K \approx 600\ Gs \cdot \Delta K$$

in the recirculator, spreader/recombiner (1 dipole, 2 edges)

$$\Delta GL \approx 2\frac{6 \cdot 10^9}{300}\frac{4\ cm}{1300^2 cm^2} \cdot \Delta K \approx 100\ Gs \cdot \Delta K$$

This should be compared to other permissible integrated quadrupole errors, which will give the tolerances for the K-value:

for injector dipoles: $\Delta K < 0.06$

for second injection stage dipoles: $\Delta K < 0.05$

for recirculator dipoles: harmless

for spreader/recombiner dipoles: $\Delta K < 0.6$ (harmless)

11.4.3 Dipole gradient errors

The integrated quadrupole error estimated above gives for the dipoles an estimation of the permissible gradient error.

In the injector dipoles: $\Delta G \approx \frac{3\ Gs}{25\ cm} \approx 0.12\frac{Gs}{cm}$

In the dipoles of the second injection stage: $\Delta G \approx \frac{30\ Gs}{60\ cm} \approx 0.5\frac{Gs}{cm}$

In the recirculator dipoles: $\Delta G \approx \frac{1800\ Gs}{150\ cm} \approx 12\frac{Gs}{cm}$

In the spreader/recombuner dipoles down to: $\Delta G \approx \frac{60\ Gs}{130\ cm} \approx 0.5\frac{Gs}{cm}$

These errors also constrain the “good field region”. Since we define good field as the field without gradient, and $B_y(x) = B_0 + \Delta G x + \cdots$, we get

in the injector dipoles (80 mm vacuum chamber is assumed): $\frac{\Delta B}{B} = \frac{\Delta GL \cdot a}{B_0 L} \approx \frac{3\ Gs \cdot 4\ cm}{400\ Gs \cdot 25\ cm} \approx 1.2 \cdot 10^{-3}$

in the dipoles of the second injection stage (140 mm vacuum chamber is assumed): $\frac{\Delta B}{B} \approx \frac{30\ Gs \cdot 7\ cm}{4400\ Gs \cdot 60\ cm} \approx 8 \cdot 10^{-4}$

in the recirculator dipoles (40 mm vacuum chamber is assumed): $\frac{\Delta B}{B} \approx \frac{1800\ Gs \cdot 2\ cm}{15000\ Gs \cdot 140\ cm} \approx 1.7 \cdot 10^{-3}$

in the spreader/recombiner dipoles (40 mm vacuum chamber is assumed, for the magnets with multiple beams 40 mm is assumed for every single beam): $\frac{\Delta B}{B} \approx \frac{60\ Gs \cdot 2\ cm}{15000\ Gs \cdot 130\ cm} \approx 6 \cdot 10^{-5}$

11.4.4 Sextupole alignment

In a sextupole, the field is given by $B_y = \frac{1}{2}mx^2$, therefore, alignment tolerance should be better, than

$$x = \frac{\Delta GL}{mL}$$

For the sextupoles in the second injection stage it gives

$$\Delta x = \frac{30\ Gs}{160\frac{Gs}{cm^2}\cdot 10\ cm} \approx 0.2\ mm$$

Sexupole strength taken here (~500 1/m^3) is our estimation of what would be necessary to set the second order in longitudinal motion (non-linearity compensation in the short pulse mode). So, the sextupole alignment tolerance is determined by the arising quadrupole field (this tolerance is tighter, than those arising from the dipole field (0.6 mm)).

11.4.5 Emittance dilution effect due to a quadrupole field ripple

As estimation we take for emittance dilution in a quadrupole with a fast varying field (see Figure 2):

$$\Delta\varepsilon = \frac{1}{2\sqrt{2}}\frac{x^2}{F} \Rightarrow \frac{\Delta\varepsilon}{\varepsilon} = \frac{1}{2\sqrt{2}}\frac{\beta}{F}$$

where F is the focal length, corresponding to the AC field amplitude $F = \frac{pc}{e\Delta GL}$. From that we get

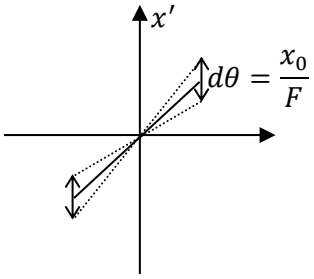

Figure 78. Mechanism of the emittance dilution in a quadrupole field.

$$\frac{\Delta G}{G} = \frac{2\sqrt{2}F_0}{\beta}\frac{\Delta\varepsilon}{\varepsilon}$$

where F_0 is the nominal focal length of the quadrupole. Substituting again 10% emittance growth, we get the field stability

in the quadrupoles (both injection stages and recirculator):

$$\frac{\Delta G}{G} \sim \frac{2\sqrt{2}\cdot 0.5\ m}{10\ m} 0.1 \sim 10^{-2}$$

in the quadrupoles of spreader/recombiner (worst case beta-function):

$$\frac{\Delta G}{G} \sim \frac{2\sqrt{2}\cdot 0.6\ m}{800\ m} 0.1 \sim 2\cdot 10^{-4}$$

12 Appendix E: Analysis of injection schemes

Here we discuss different acceleration schemes for an Energy Recovery Linac based light sources.

The improvement potential one wants to exploit with different distribution of acceleration over injector, pre-injection linac, and single- or multi-turn acceleration is the impact on the beam optics, BBU threshold current, and costs of the linac(s).

We assume for all schemes the same injector and dump parts.

- The first scheme (*direct injection scheme*) consists of one main Linac with direct injection at 7 MeV. The main disadvantage of this scheme is the high ratio between the injection energy E_{in}=7 MeV and the final energy E_{fin}=6 GeV. This disadvantage complicates the focusing in the linac, because the triplets, which focus a beam at the beginning of the linac, will not affect it at the same position on the deceleration. Therefore we exclude this scheme from our analysis. It was analysed in [24].
- The second scheme has a small preinjection linac, what makes lower the high-to-low energy ratio in the main linac and improves transverse optic in the linac, and therefore, the BBU instability. Another advantage of having a preinjection linac is that the preinjection arcs can be used for longitudinal bunch compression (additional compression stage) on acceleration, to reduce the energy spread during deceleration by decompression, and to compensate for the average energy loss of the beam due to radiation.
- The third scheme which is proposed for FSF also has preinjector but it is a multi-turn scheme with 3 passes for acceleration and 3 for deceleration with a split main linac. The split main linac allows having different arcs for each beam energy on acceleration and deceleration.

12.1 Two stage injection scheme

In this part an improved scheme of the ERL based light source is discussed. The layout of this scheme is presented in Figure 79.

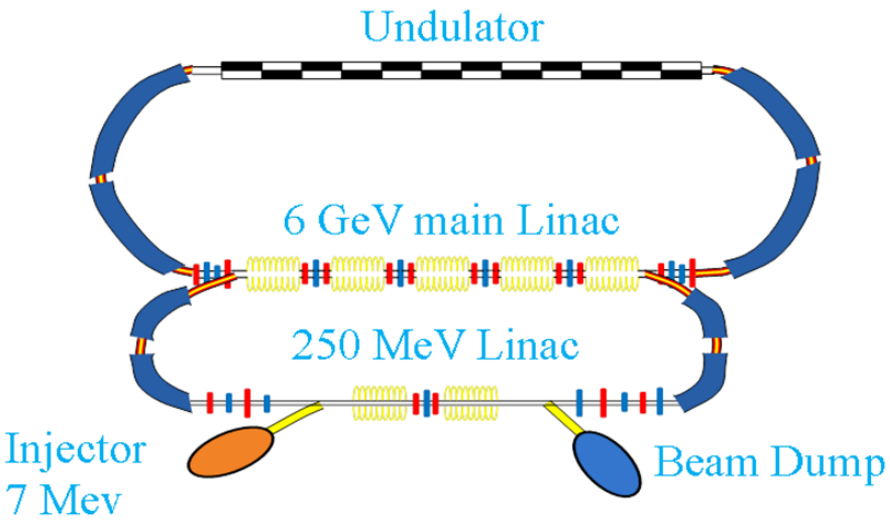

Figure 79. Two stage injection scheme.

The main improvement is that now a beam after an injector goes to a short linac (preinjector), where it is accelerated up to 250 MeV, then it passes the first arc and comes to the main linac where it is accelerated up to 6 GeV. After that it might be used as a light source. After the beam was used it goes back on the deceleration phase. Our goal again will be to find the optimum optic solution for the beam break up stability in the both linacs. But first let us discuss the stability in the preinjection linac.

12.1.1 Preinjector

For the preinjection linac we suggest to use two cryomodules with a triplet of quadrupole magnets in between. The role of this triplet is to change the sign of the Twiss parameter α of the beam. The optimum for BBU instability initial Twiss parameters were found in [24] and given by:

$$\beta_0 = \sqrt{\frac{\gamma_1}{\gamma_0}\frac{m_{12}^3}{t_{12}}},$$

$$\alpha_0 = m_{11}\sqrt{\frac{\gamma_1}{\gamma_0}\frac{m_{12}}{t_{12}}},$$

where m_{ij} and t_{ij} is the transfer matrices of the 1st and 2nd cryomodules, $\gamma_{0,1}$ – the Lorentz factors before and after the first cryomodule. Using Elegant program one can find the matrix elements of the cryomodules: m_{11}= -0.835, m_{12}= 1.62 m. and t_{12}= 7.261 m. And finally the initial Twiss parameters are: α_0= -1.421 and β_0= 2.757 m. It should be noted, that the initial parameters we found are at the entrance to the cavity but not to the cryomodule (where it is about 1 m of a free drift Figure 22), therefore they should be transformed back for this distance. The final optic is presented in Figure 80.

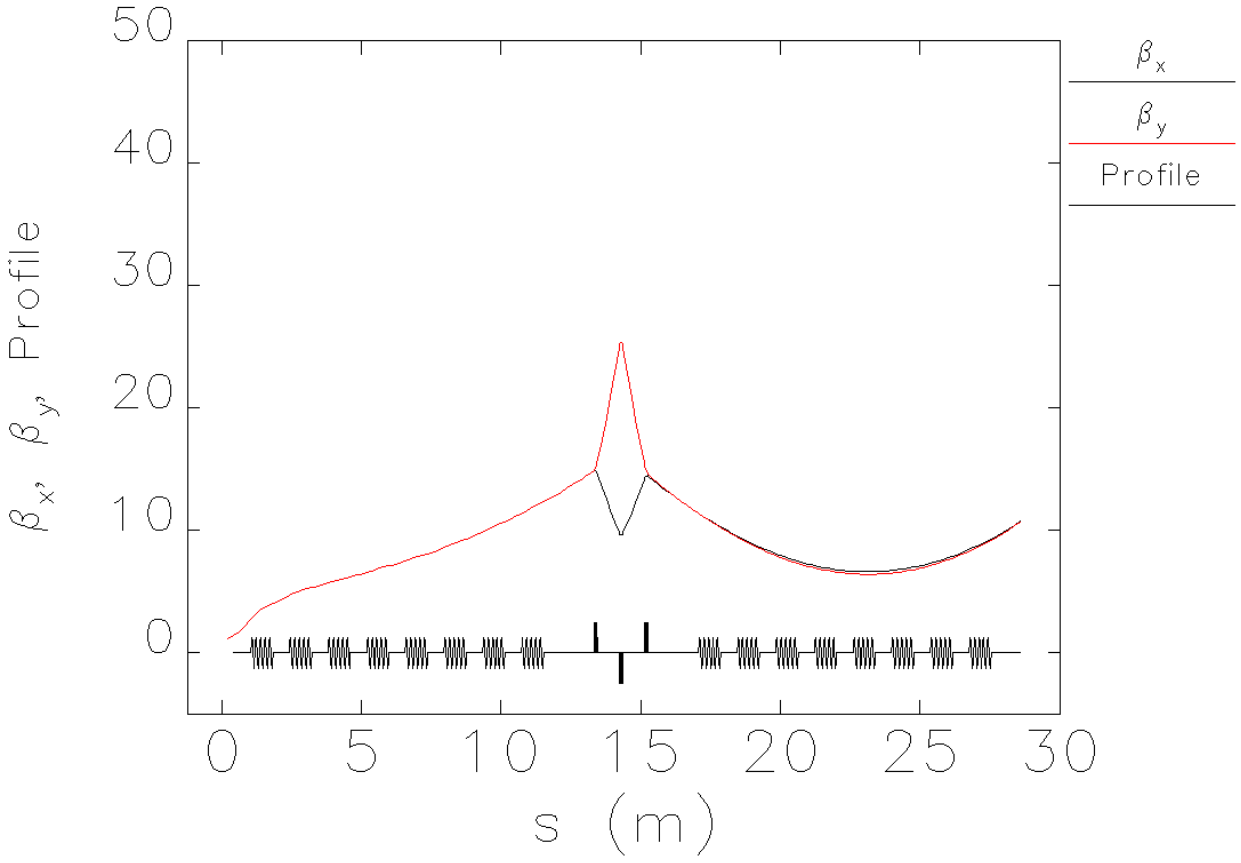

Figure 80. Optic design of the preinjector for two stage injection scheme.

The estimated value of the threshold current for a mode with $(R/Q)_d \cdot Q = 6 \cdot 10^5$ Ω, $\omega = 2\pi \cdot 2 \cdot 10^9$ Hz located in the first and the last cavities is 1.64 A, when the value in the middle of cryomodule is higher – about 2.5 A. In the next part we discuss the optic in the main linac.

12.1.2 Main Linac

The main difference for the optic design between layouts with direct injection and with a preinjector is that in the scheme with two stage injection the initial energy in the main linac is 250 MeV instead of 7 in the scheme with a direct injection. Therefore, it strongly improves the optics. The quadrupole magnets which focus the beam on the low energies (>250 MeV) will also focus the beam on the high energies (<6 GeV). And on such high energies as we already discussed the cavity is like a free drift with acceleration, so RF focusing can be neglected. Therefore, the optic was calculated in the following way: for the first half of the linac the triplets between the cryomodules were adjusted in such a way that the beam will go like in a free drift with initial/final beta-functions about the length of the cryomodule (Figure 81). The role of the triplets is to change the sign of the alpha-function, so it should be calculated for this purpose. The second part assumed to be symmetrical to have the same optics on the deceleration, which is given from right to left in Figure 81. It should be noted, that in order to improve the optic of the second part

of the linac positive and negative triplets were used and sum of the quadrupole powers in the triplet is not equal zero.

In this optic design there are different thresholds for different cavities in the linac. For the first/last cavity estimations give the threshold current about 4 A and 35 A for the cavity in the middle of the linac for the mode with $(R/Q)_d \cdot Q = 6 \cdot 10^5$ Ω, $\omega = 2\pi \cdot 2 \cdot 10^9$ Hz.

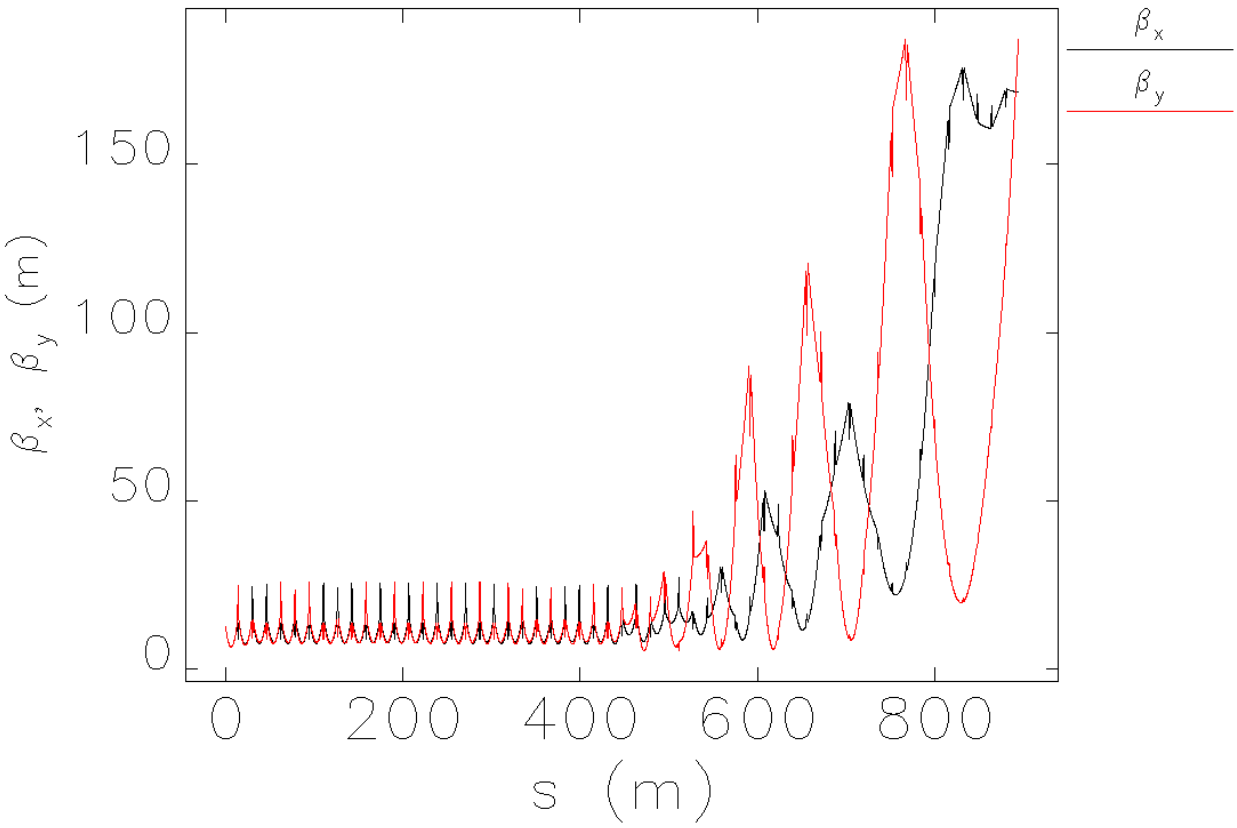

Figure 81. Optic design of the main 6 GeV linac for two stage injection scheme.

12.2 The scheme of FSF with 100 MeV preinjector

The very first proposed scheme of FSF is presented in Figure 82. In this scheme a beam accelerated in the preinjection linac up to 100 MeV and there are 1 GeV energy gains in both main linacs on the each pass.

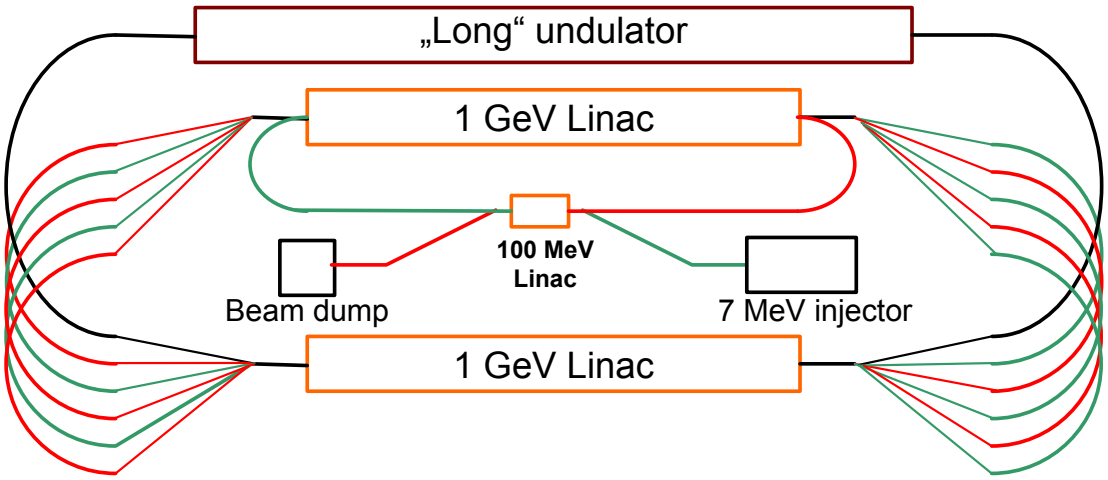

Figure 82. Principal layout of the multi-turn ERL with a cascade injection. The beam acceleration path is shown in green, deceleration path – in red.

The linac is planned to be based on the B*ERL*inPro 7-cell cavities. To reach 1 GeV in the linac we took 72 cavities and distributed them over 9 cryomodules.

Triplets of quadrupoles are planned to be in between the cryomodules in the linac. The full length of the linac is then about 140 m. Optics for all three passes through the first 1 GeV linac is presented in Figure 83. It will be discussed below that BBU instability will develop in the 1st linac. Therefore, the strengths of the quadrupoles were optimized to have the minimum of the beta functions on the 1st pass through the 1st linac.

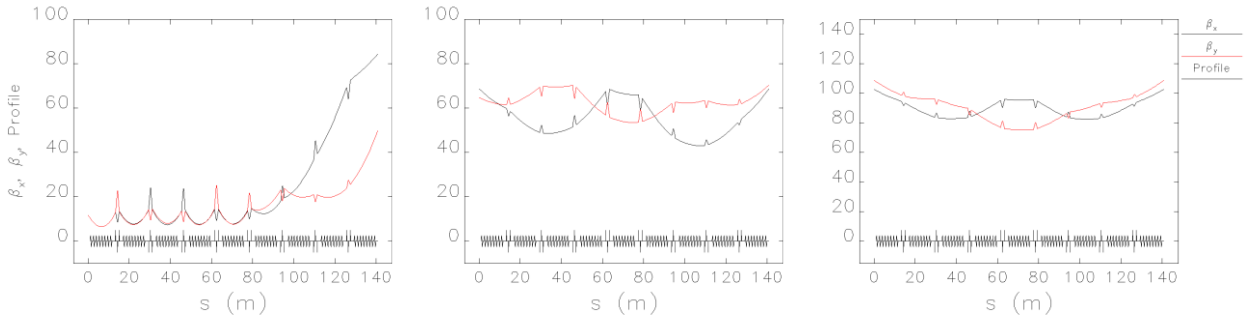

Figure 83. Optic design of the first 1 GeV linac. 3 passes with 1, 3 and 5 GeV beam energy after the pass from left to right correspondingly.

Also the optics was designed for the second 1 GeV Linac and it is presented in

Figure 84.

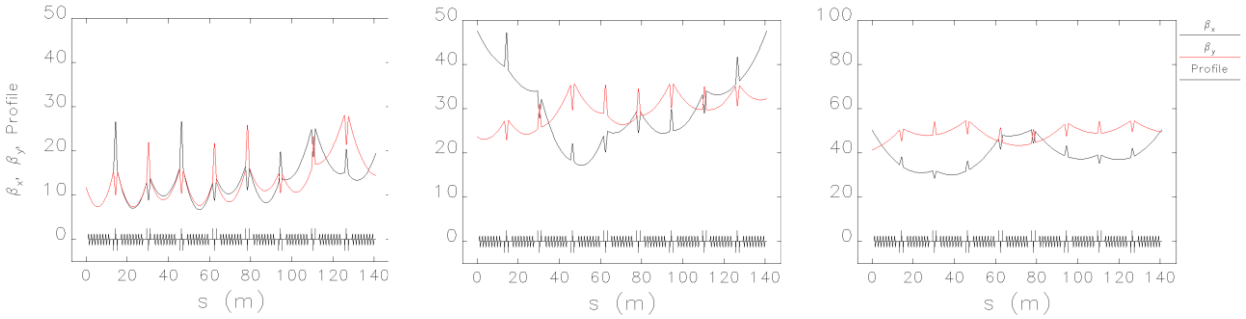

Figure 84. Optic design of the second 1 GeV linac. 3 passes with 2, 4 and 6 GeV beam energy after the pass from left to right correspondingly.

In both linacs the optic is assumed to have mirror symmetry at the middle of the 5th cryomodule. Optic for deceleration is shown from right to left in Figure 83 and

Figure 84.

Optic in the preinjector (Figure 85) can be calculated using the same approach as in Ch.12.1.1. It was presented in [24].

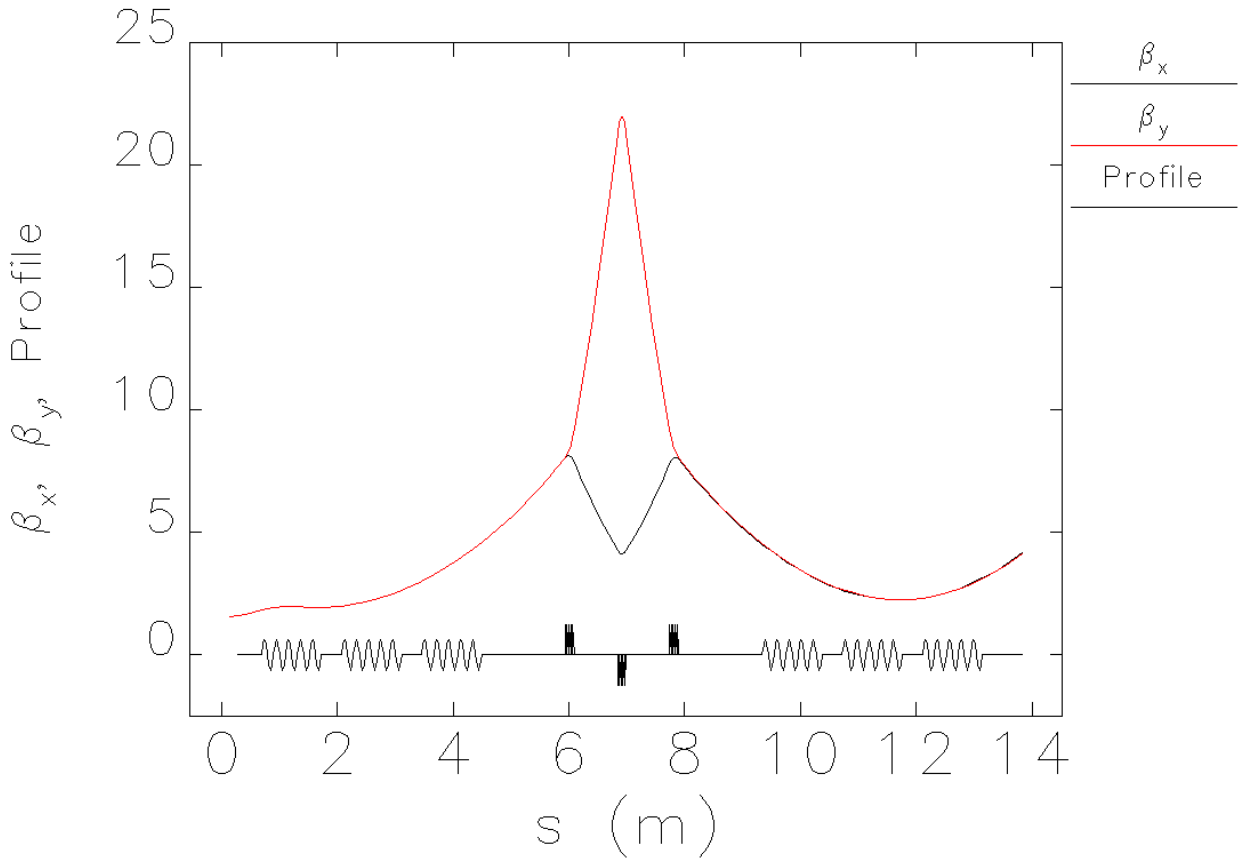

Figure 85. Optic design of 100 MeV preinjector for FSF.

For optic, presented in Figure 83,

Figure 84, the threshold current can be estimated using (86) and the typical parameters of the mode we used before: $(R/Q)_d \cdot Q = 6 \cdot 10^5$ Ω, $\omega = 2\pi \cdot 2 \cdot 10^9$ Hz. The instability will develop in the first/last cavities in the first linac 1 GeV linac with a threshold current of about 0.88 A. The estimated value of the threshold current for the second linac is higher – about 3.73 A. And in the preinjector this value is about 1.26 A. As you can see, the value of the threshold current in the second 1 GeV linac is about 4 times higher. Let's change the energy gains in the main linacs to decrease this difference. This should increase the threshold current of the facility.

12.3 Different acceleration pattern of the FSF scheme

In this paragraph an improvement of the first proposed scheme of FSF is under discussion. The first scheme had 100 MeV preinjection and then two 1 GeV linacs (Figure 82). The new improved scheme is presented in Figure 86.

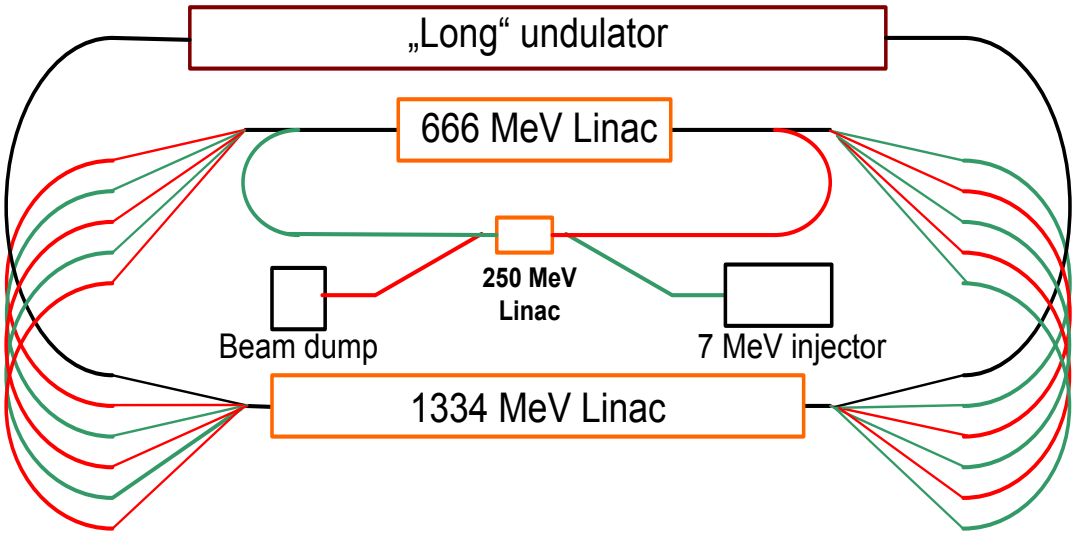

Figure 86. The improved for BBU stability acceleration scheme of FSF.

The main motivation of this improvement is BBU instability. The new scheme gives roughly 1.7 times better threshold current for the 1st cavity in the 1st linac, where the instability develops in the first scheme. The energy gain in the preinjector was also increased up to 250 MeV, so now it is like described in Ch.12.1.1.

The easiest way to see the reason of rebalancing of the energies in the two main linacs is to analyse (74), especially the square root in the denominator. Let's find a balance between the energy gains in two main linacs to have equal threshold currents for them. To do that, a model with linacs, when a focusing from a triplets is neglected for the second and the third passes, will be analysed. In this model with the injection energy of about 250 MeV the transverse focusing inside the cavities can be neglected. So, it is assumed that the beta functions of a beam at the exit and at the entrance to the linac are about the length of the linac for the second and the third passes and for the end of the linacs at the first pass. But it is about the length of the one cryomodule at the entrance to the 1st linac at the first pass.

Let's introduce *G* as a gradient of the cavities in MeV/m, *L= 2000* [MeV] */G* is a length of the cavity structure, required to accelerate to the final energy of 2 GeV, *x* is the length of the first linac and, therefore, *L-x* is the length of the 2-nd. Now one can find energies $\gamma_{1(2),n}$ for each pass and as we assumed before $\beta_{1,1(6)} = \beta_{2,1(6)} \sim 12.57$ m and $\beta_{1,n} = x$ or $\beta_{2,n} = L-x$ for the first and the second linac respectively and for n=2..5.

Let's proceed with the following equation:

$$\sqrt{\sum_{m=1}^{2N-1}\sum_{n=m+1}^{2N}\frac{\beta_{1,n}\beta_{1,m}}{\gamma_{1m}(x)\gamma_{1n}(x)}} = \sqrt{\sum_{m=1}^{2N-1}\sum_{n=m+1}^{2N}\frac{\beta_{2,n}\beta_{2,m}}{\gamma_{2m}(x)\gamma_{2n}(x)}},$$

when the threshold currents have the same values for the 1st and last cavities in both linacs. This equation can be solved numerically and gives the result that $x \sim L/3$ with injection energy – $\gamma_{1,1} = 480$.

With this result one can get the energy gains in the first and second main linacs to be 666 and 1334 MeV correspondingly.

Let's continue with a modeling of the linac optics in Elegant program. Optics for all three passes through the first 666 MeV linac is presented in Figure 87.

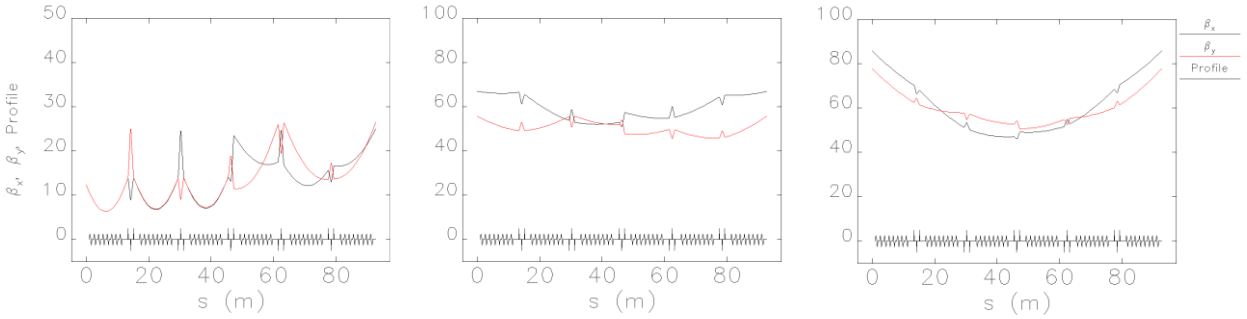

Figure 87. Optics design of the first 666 MeV linac. 3 passes with 250, 2250 and 4250 MeV beam injection energy from left to right respectively.

Also the optics was calculated for the second 1334 MeV linac and it is presented in Figure 88.

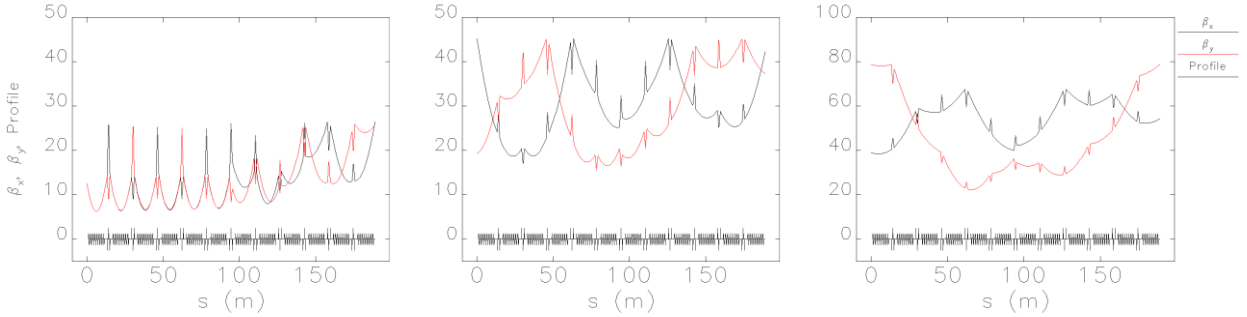

Figure 88. Optics design of the second 1334 MeV linac. 3 passes with 916, 2916 and 4916 MeV beam injection energy from left to right respectively.

To estimate the values of the threshold currents the same approach as usual can be used (Eq. (86) and a mode with $(R/Q)_d \cdot Q = 6 \cdot 10^5$ Ω, $\omega = 2\pi \cdot 2 \cdot 10^9$ Hz). And for the first linac the threshold current is improved and it is about 1.46 A, when for the second it is 3.58 A and slightly decreased. So, the value of threshold current for the 1st main linac was improved. It was also slightly decreased for the 2nd linac and for the preinjection linac its value about 1.64 A. But this scheme has a more complicated spreader, because the energies of the beam in the spreader are: …4250, 4916, 6250, which closer than in the first scheme: 4250 and 5250… Therefore, this scheme seems impractical for us. In the next paragraph let's go back for the scheme with the same energy gains in the main linacs, but with thoughts to connect energies of a beam on different passes to fix the spreader design.

12.4 Conclusion (injection and acceleration schemes)

In this paragraph we summarize the results of the estimations of the threshold currents for different acceleration schemes presented in the previous paragraphs. The results are presented in

Table 27: Threshold currents for different schemes.

Linac scheme	I_{th}, A		
	Preinjector	1st Linac	2nd Linac
Two stage injection (single turn)	1.64	4 (one linac)	
100+2x1000 MeV	1.26	0.88	3.73
250 + 666 + 1334MeV	1.64	1.46	3.58
Scalable scheme 230+2x960 MeV	0.48	0.73	2.34

It should be noted that the values in Table 27 are just the estimations of the threshold currents. These estimations were made assuming that there is only one mode in a linac. In principle this is the comparison of the square roots in the denominator of Eq. (79) for the different cavities and different injection schemes. Such problems as coupling and overlapping of the different modes are not taken into account. These problems will decrease the threshold current and, therefore, should be taken into account later.